Phenomenology

Lectures given at the 2016 HEP Summer School

Simon Badger,
IPPP, Durham University.

1 Introduction

Historically the lecture notes for the phenomenology course have consisted of the slides presented in the lectures. These notes are intended to provide additional information, and more mathematical detail, on the more theoretical aspects of the course which don't change from year to year. The recent experimental results, which as the LHC experiments take more and more data change from day-to-day, will continue to be presented solely on the slides used in the lectures.

These notes have been adapted from notes from Daniel Maïtre and Peter Richardson.

In order to study hadron collisions we need to understand the basics of cross section calculations, Quantum Chromodynamics (QCD) and jets which we will first consider in the simpler environment of e^+e^- and lepton-hadron collisions before we go on to study hadron–hadron collisions.

Unfortunately there is no single good book on modern phenomenology. Two old classics but now a bit dated are:

- *Quarks and Leptons* Halzen and Martin [1];
- *Collider Physics* Barger and Phillips [2].

Two good books, although mainly focused on QCD and probably at a bit too high a level for this course, are:

- *QCD and Collider Physics* Ellis, Stirling and Webber [3];
- *Quantum Chromodynamics* Dissertori, Knowles and Schmelling [4];

and of course the classic on Higgs physics

- *The Higgs Hunter's Guide* Gunion, Haber, Kane and Dawson [5].

In addition the recent reviews:

- *Towards Jetography* [6] which provides a good primer on jet physics;
- *General-purpose event generators for LHC physics* [7] which gives a detailed description of the physics of Monte Carlo event generators;

are good sources of additional information.

2 e^+e^- Annihilation

While electron-positron colliders are less relevat for current phenomenology than they were before, they are a good starting oint to discuss many concepts one also finds at hadron colliders.

If we consider what happens when electrons and positrons collide, then the most likely thing is that some hadrons are produced. However, none of the Lagrangians or Feynman rules you've learnt involve hadrons. This is the key issue in most collider physics, we can calculate things for quarks and gluons but we observe hadrons.

2.1 Leading Order

We will start by studying one of the simplest possible processes, e^+e^- annihilation via the exchange of a photon or Z^0 boson, as shown in Fig. 1. This process can produce either

Figure 1: Feynman diagrams for e^+e^- annihilation into leptons and quarks.

quarks or leptons. Unfortunately due to quark confinement we cannot observe free quarks directly, instead quarks and antiquarks will produce hadrons with unit probability. Much of what we will study in this course will be concerned with the question, given that we observe hadrons how do we infer what was going on in the fundamental process involving quarks?

We will start with the simplest example. Given that quarks and antiquarks produce hadrons with unit probability we can measure the cross section for the process $e^+e^- \to q\bar{q}$, which we can calculate perturbatively, by measuring the cross section for $e^+e^- \to$ hadrons. This is the case because gluons (which also produce hadrons) do not couple directly to the leptons. This is the basis of most collider phenomenology, we want to measure things using hadrons that we can calculate using partons. The total cross section for e^+e^- annihilation into hadrons is the simplest such observable.

Using the techniques you have learnt in the other courses you can now calculate the total cross section for e^+e^- annihilation. In reality it is more common to study the ratio

$$R \equiv \frac{\sigma(e^+e^- \to \text{hadrons})}{\sigma(e^+e^- \to \mu^+\mu^-)}, \tag{1}$$

as this reduces experimental uncertainties. At low energies this process is dominated by photon exchange so we can neglect the Z^0 boson. In this limit

$$\sigma(e^+e^- \to \mu^+\mu^-) = \frac{4\pi\alpha^2}{3s}, \tag{2}$$

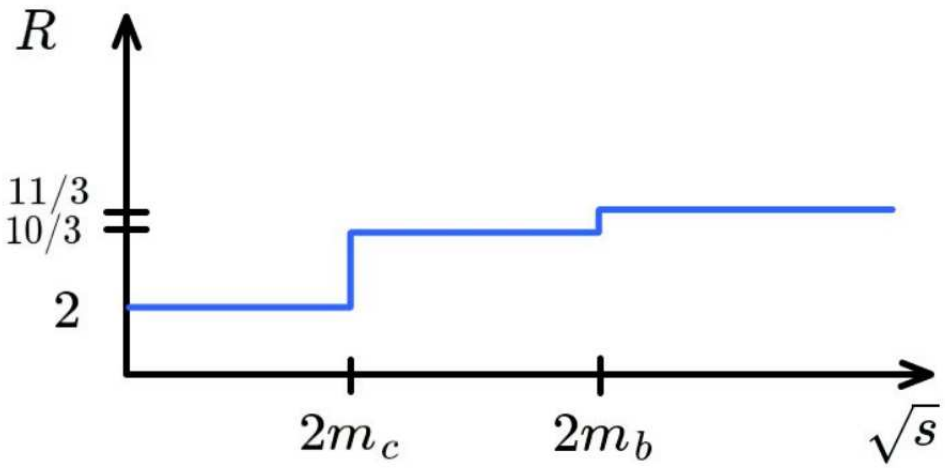

Figure 2: Expected shape for the R ratio.

where s is the centre-of-mass energy of the collision squared. The cross section for the production of quarks is

$$\sigma(e^+e^- \to \text{hadrons}) = \frac{4\pi\alpha^2}{3s} \sum_q e_q^2 N_c, \tag{3}$$

where e_q is the charge of the quark in units of the positron charge and the sum runs over all quarks for which the centre-of-mass energy $\sqrt{s} > 2m_q$, where m_q is the mass of the quark. Remember we must sum over all the quantum numbers of the quarks so the cross section is multiplied by number of colours, N_c. Therefore for centre-of-mass energies much less than the mass of the Z^0 boson, $\sqrt{s} \ll M_z$,

$$R = \sum_q e_q^2 N_c = \underbrace{\underbrace{\underbrace{N_c\left(\frac{4}{9} + \frac{1}{9} + \frac{1}{9}\right.}_{u,d,s} + \frac{4}{9}}_{u,d,s,c} + \left.\frac{1}{9}\right)}_{u,d,s,c,b} . \tag{4}$$

The expected picture is shown in figure 2. The experimental measurement of this ratio is shown in Fig. 3 as a function of energy showing the thresholds for the production of the charm and bottom quarks. Below the charm threshold there are three active quarks down ($e_d = -\frac{1}{3}$), up ($e_u = \frac{2}{3}$) and strange ($e_s = -\frac{1}{3}$) giving $R = 2$. Above the charm ($e_c = \frac{2}{3}$) threshold $R = \frac{10}{3}$ while above the bottom ($e_b = -\frac{1}{3}$) threshold $R = \frac{11}{3}$.

2.1.1 The Z resonance

For energies $\sqrt{s} \sim m_Z$ we will need to include the effects of the second diagram in Fig. 1. The cross-section will then have three different contributions, the photon background, the

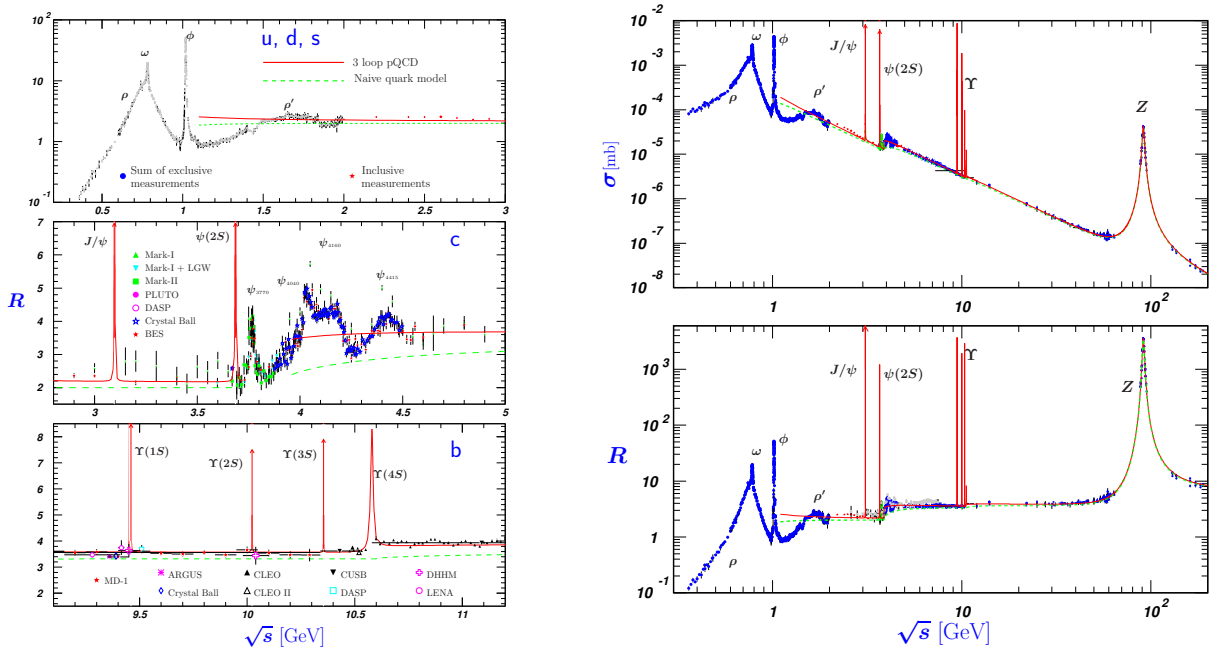

Figure 3: The ratio $R \equiv \frac{\sigma(e^+e^- \to \text{hadrons})}{\sigma(e^+e^- \to \mu^+\mu^-)}$ as a function of energy taken from Ref. [8].

Z-boson resonance and the photon-Z interference. The total cross-section, summed and averaged over spins can be written as (e.g. [3]):

$$\sigma\left(f\bar{f} \to f'\bar{f}'\right) = \alpha^2 \frac{\pi}{2s} \int_{-1}^{1} d(\cos\theta) \Bigg\{ \left(1+\cos^2\theta\right)\left(q_f^2 q_{f'}^2 + \frac{g_Z^2}{4g_e^2} q_f q_{f'} v_f v_{f'} \chi_1 + \frac{g_Z^4}{16 g_e^4}(a_f^2+v_f^2)(a_{f'}^2+v_{f'}^2)\chi_2\right) + \cos\theta\left(\frac{g_Z^2}{2g_e^2} a_f a_{f'} v_f v_{f'} \chi_1 + \frac{g_Z^4}{2g_e^4} a_f a_{f'} v_f v_{f'} \chi_2\right)\Bigg\}$$

where

$$\frac{g_Z}{g_e} = \frac{1}{\cos\theta_w \sin\theta_w} \qquad \chi_1 = \frac{s(s-m_Z^2)}{(s-m_Z^2)^2 + m_Z^2\Gamma_Z^2} \qquad \chi_2 = \frac{s^2}{(s-m_Z^2)^2 + m_Z^2\Gamma_Z^2}$$

The axial ($v_f = T_f^3 - 2q_f \sin^2\theta_w$) and vector ($a_f = T_f^3$) couplings in the Standard Model are given in Table 1. T_f^3 is the 3rd component of the weak isospin as covered in the course on the Standard Model. The terms proportional to χ_2 come from the Z resonance while those propotional to χ_1 come from the photon-Z interference. Γ_Z is the width of the Z boson.

Later we will take a closer look at the EW sector of the Standard Model and use this measurement to find constraints on the number of neutrinos families below the Z mass threshold (see Figure 28).

	q_f	a_f	v_f
u, c, t	$2/3$	$1/2$	$1/2 - 4/3 \sin^2\theta_w$
d, s, b	$-1/3$	$-1/2$	$-1/2 + 2/3 \sin^2\theta_w$
e, μ, τ	-1	$-1/2$	$-1/2 + 2\sin^2\theta_w$
ν_e, μ, τ	0	$1/2$	$1/2$

Table 1: EW couplings in the Standard Model.

2.2 Higher Order Corrections

When we draw Feynman diagrams we are performing a perturbative expansion in the (hopefully) small coupling constant. Unfortunately the strong coupling often isn't very small, at the Z^0 mass, $\alpha_S(M_Z) = 0.118$. We therefore need to consider higher orders in the perturbative expansion. There are always two types of correction:

- real gluon emission;
- virtual gluon loops.

2.2.1 Real Emission

There are two possible diagrams for gluon emission, see Fig. 4. The matrix element, only

Figure 4: Feynman diagrams for $e^+e^- \to q\bar{q}g$.

considering photon exchange for simplicity, is

$$\begin{aligned} \mathcal{M} &= e^2 e_q g_s t^a_{ij} \bar{v}(p_b)\gamma_\mu u(p_a)\frac{-g^{\mu\nu}}{q^2} \\ &\quad \bar{u}_i(p_1)\left[\gamma_\sigma \frac{\not{p}_1+\not{p}_3}{(p_1+p_3)^2}\gamma_\nu - \gamma_\nu \frac{\not{p}_2+\not{p}_3}{(p_2+p_3)^2}\gamma_\sigma\right] v_j(p_2)\epsilon^\sigma_a(p_3), \end{aligned} \tag{5}$$

where $p_{a,b}$ are the 4-momenta of the incoming electron and positron, respectively. The outgoing quark, antiquark and gluon have 4-momenta $p_{1,2,3}$, respectively. The total momentum of the system $q = p_a + p_b = p_1 + p_2 + p_3$. The gluon has colour index $a = 1, \ldots, N_c^2 - 1$ whereas the quark/antiquark have colour indices $i, j = 1, \ldots, N_c$.

Summing/averaging over spins and colours

$$|\overline{\mathcal{M}}|^2 = \frac{4e^2 e_q^2 g_s^2 N_c}{s} C_F \frac{(p_1\cdot p_a)^2 + (p_1\cdot p_b)^2 + (p_2\cdot p_a)^2 + (p_2\cdot p_b)^2}{p_1\cdot p_3\; p_2\cdot p_3}. \tag{6}$$

The colour algebra gives a colour factor

$$\sum_a^{N_c^2-1} t^a_{ij}\left(t^a_{ij}\right)^* = t^a_{ij}t^a_{ji} = \frac{1}{2}\delta^{aa} = \frac{1}{2}(N_c^2 - 1) = N_c C_F, \tag{7}$$

where the colour charges in the fundamental (quarks and antiquarks) and adjoint (gluons) representations are

$$C_F \equiv \frac{1}{2N_c}(N_c^2 - 1) \qquad \text{and} \qquad C_A \equiv N_c, \tag{8}$$

respectively. More about the colour algebra can be found in appendix C

The three-body phase space is

$$\begin{aligned} & \mathrm{d}\Phi_n(p_a + p_b; p_1, p_2, p_3) \\ &= (2\pi)^4 \delta^{(4)}\left(p_a + p_b - p_1 - p_2 - p_3\right) \frac{\mathrm{d}^3\vec{p_1}}{(2\pi)^3 2E_1} \frac{\mathrm{d}^3\vec{p_2}}{(2\pi)^3 2E_2} \frac{\mathrm{d}^3\vec{p_3}}{(2\pi)^3 2E_3} \\ &= \frac{1}{8(2\pi)^5} E_1 \mathrm{d}E_1 \mathrm{d}\cos\theta \mathrm{d}\phi E_2 \mathrm{d}E_2 \mathrm{d}\cos\beta \mathrm{d}\alpha \frac{1}{E_3} \delta(\sqrt{s} - E_1 - E_2 - E_3), \end{aligned}$$

where θ and ϕ are the polar and azimuthal angles, respectively, of the outgoing quark with respect to the beam direction. The polar and azimuthal angles of the antiquark with respect to the quark direction are β and α, respectively. We have integrated over p_3 using the δ-function and assumed that the outgoing particles are massless.

Using momentum conservation

$$E_3 = |\vec{p_3}| = |\vec{p_1} + \vec{p_2}| = \sqrt{E_1^2 + E_2^2 + 2E_1E_2\cos\beta}. \tag{9}$$

Therefore the integral over the remaining δ-function is

$$\int \mathrm{d}\cos\beta \delta(\sqrt{s} - E_1 - E_2 - E_3) = \frac{E_3}{E_1 E_2}, \tag{10}$$

so

$$\begin{aligned} \mathrm{d}\Phi_n(p_a + p_b; p_1, p_2, p_3) &= \frac{1}{8(2\pi)^5} \mathrm{d}E_1 \mathrm{d}\cos\theta \mathrm{d}\phi \mathrm{d}E_2 \mathrm{d}\alpha \\ &= \frac{s}{16(2\pi)^3} \mathrm{d}x_1 \mathrm{d}x_2 \frac{\mathrm{d}\cos\theta \mathrm{d}\phi \mathrm{d}\alpha}{2(2\pi)^2}, \end{aligned} \tag{11}$$

where $x_i \equiv 2E_i/\sqrt{s}$. Momentum and energy conservation requires that $x_1 + x_2 + x_3 = 2$.

The total cross section is

$$\begin{aligned} \sigma &= \frac{1}{2s} \frac{s}{16(2\pi)^3} \int \mathrm{d}x_1 \mathrm{d}x_2 \frac{\mathrm{d}\cos\theta \mathrm{d}\phi \mathrm{d}\alpha}{2(2\pi)^2} |\overline{M}|^2, \\ &= \frac{4\pi\alpha^2 e_q^2 N_c}{3s} C_F \frac{\alpha_S}{2\pi} \int \mathrm{d}x_1 \mathrm{d}x_2 \frac{x_1^2 + x_2^2}{(1 - x_1)(1 - x_2)}. \end{aligned} \tag{12}$$

The contribution from the Z^0 boson is the same except for σ_0. This is divergent at the edge of phase space as $x_{1,2} \to 1$ so that the total cross section is $\sigma = \infty$!

This is a common feature of all perturbative QCD calculations. Configurations which are indistinguishable from the leading-order result are divergent. Physically there are two regions where this happens.

1. *Collinear limit:* If we take $x_1 \to 1$ at fixed x_2 or $x_2 \to 1$ at fixed x_1. We can see what happens physically by considering the dot product of the antiquark and gluon 4-momenta, *i.e.*

$$2p_2 \cdot p_3 = \frac{sx_2x_3}{2}(1-\cos\theta_{23}) = s(1-x_1) \;\Rightarrow\; (1-\cos\theta_{23}) = \frac{2(1-x_1)}{x_2x_3} \to 0. \quad (13)$$

   So the limit $x_1 \to 1$, where the matrix element diverges, corresponds to the angle between the antiquark and gluon $\theta_{23} \to 0$, *i.e.* collinear emission of the gluon from the antiquark. Similarly the limit $x_2 \to 1$ corresponds to collinear emission of the gluon from the quark.

2. *Soft limit:* $x_{1,2} \to 1$ at fixed $\frac{1-x_1}{1-x_2}$. We can consider what happens in this limit by considering the energy of the gluon

$$E_g = \frac{\sqrt{s}}{2}x_3 = \frac{\sqrt{s}}{2}(1-x_1+1-x_2) \to 0, \quad (14)$$

   i.e. the matrix element diverges in the soft limit, when the energy of the gluon is small.

These are both universal features of QCD matrix elements. In general one can see how the divergencies appear by looking at the propagator just before the emission of a gluon.

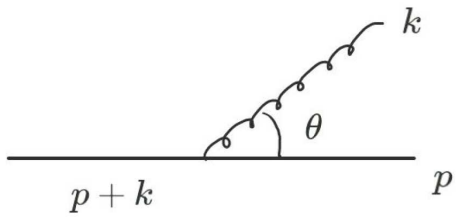

$$P^2 = (k+p)^2 = 2|\vec{k}||\vec{p}|(1-\cos\theta)$$

From this expression one can see that the propagator vanishes (and therefore divergences appear) when the gluon is either soft ($|k| \to 0$) or collinear ($\cos\theta \to 0$)

In these limits QCD matrix elements *factorize*, *i.e.* the matrix element including the emission of a soft or collinear gluon can be written as the convolution of the matrix element before the emission and a universal term describing collinear or soft emission.

Collinear Limit If we first consider collinear emission we take the momentum of the gluon p_3 parallel to p_2 ($\theta_{23} = 0$). We can therefore define

$$p_2 = (1-z)\bar{p}_2, \qquad p_3 = z\bar{p}_2, \qquad \text{with } \bar{p}_2^2 = 0, \quad (15)$$

where $\bar{p}_2$ is the momentum of the antiquark before the gluon radiation and z is the fraction of the original antiquark's momentum carried by the gluon. In this limit the matrix element factorizes

$$|\mathcal{M}_{q\bar{q}g}|^2 = |\mathcal{M}_{q\bar{q}}|^2 \times \frac{g_s^2}{p_2 \cdot p_3} \times C_F \frac{1+(1-z)^2}{z}. \quad (16)$$

As does the phase space

$$\mathrm{d}x_1\mathrm{d}x_2 \longrightarrow \frac{1}{4}z(1-z)\mathrm{d}z\mathrm{d}\theta_{23}^2. \tag{17}$$

Putting this together

$$\sigma = \sigma_0 \int \frac{\mathrm{d}\theta_{23}^2}{\theta_{23}^2} dz C_F \frac{\alpha_S}{2\pi} \frac{1+(1-z)^2}{z} = \sigma_0 \int \frac{\mathrm{d}\theta_{23}^2}{\theta_{23}^2} dz \frac{\alpha_S}{2\pi} \hat{P}_{q\to gq}(z). \tag{18}$$

The Dokshitzer-Gribov-Lipatov-Altarelli-Parisi (DGLAP) splitting function is a universal probability distribution for the radiation of a collinear gluon in any processes producing a quark. The splitting functions are:

$$\begin{aligned} \hat{P}_{g\to gg}(z) &= C_A \left[\frac{1-z}{z} + \frac{z}{1-z} + z(1-z)\right]; & \hat{P}_{q\to qg}(z) &= C_F \frac{1+z^2}{1-z}; \\ p_{g\to q\bar{q}}(z) &= T_R \left[z^2 + (1-z)^2\right]; & \hat{P}_{q\to gq}(z) &= C_F \frac{1+(1-z)^2}{z}; \end{aligned} \tag{19}$$

where z is the fraction of the momenta carried by the first outgoing particle and $T_R = \frac{1}{2}$.

Soft Limit In the limit that $E_g \to 0$ the matrix element for the process factorizes

$$\mathcal{M}_{q\bar{q}g} = \mathcal{M}_{q\bar{q}} g_s t^a_{ij} \left(\frac{p_1}{p_1\cdot p_3} - \frac{p_2}{p_2\cdot p_3}\right)\cdot \epsilon_A(p_3), \tag{20}$$

the *eikonal current*. The matrix element squared therefore factorizes in this case

$$|\mathcal{M}_{q\bar{q}g}|^2 = |\mathcal{M}_{q\bar{q}}|^2 g_s^2 C_F \frac{2p_1\cdot p_2}{p_1\cdot p_3 p_2\cdot p_3}. \tag{21}$$

The phase space is

$$\mathrm{d}x_1\mathrm{d}x_2 \longrightarrow \frac{2}{s} E_g \mathrm{d}E_g \mathrm{d}\cos\theta. \tag{22}$$

So in the soft limit

$$\sigma = \sigma_0 \int C_F \frac{\alpha_S}{2\pi} \frac{\mathrm{d}E_g}{E_g} \mathrm{d}\cos\theta \frac{2(1-\cos\theta_{qq})}{(1-\cos\theta_{qg})(1-\cos\theta_{qg})}, \tag{23}$$

the *dipole radiation pattern* a universal probability distribution for the emission of a soft gluon from any colour-connected pair of partons.[1]

Figure 5 illustrates the dipole radation pattern.

2.2.2 Virtual Corrections

There are three diagrams involving virtual gluon loops, see Fig. 6. This contribution is also divergent, but negative. This will cancel the real divergence to give a finite answer. To show this we need to regularize both the real and virtual cross sections and add them together. The result should be finite when we remove the regularization. The standard

[1] Strictly this is only universal at the amplitude level, not as a probability distribution.

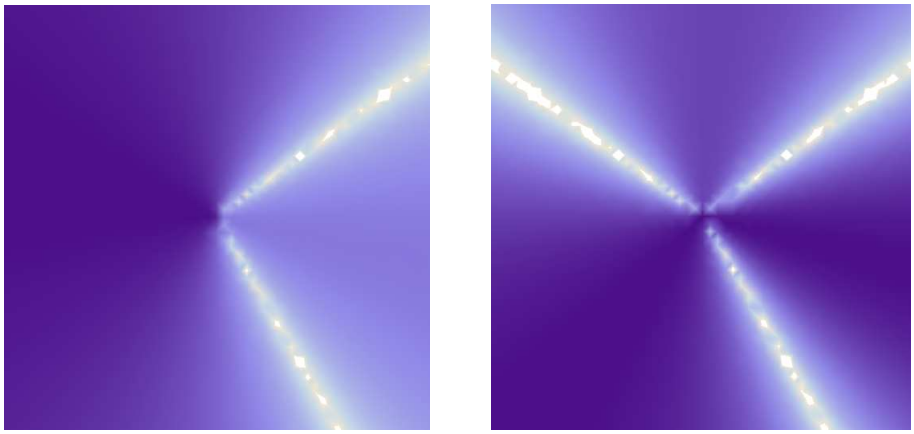

Figure 5: Dipole radiation pattern for $e^+e^- \to q\bar{q}\gamma$ and $e^+e^- \to q\bar{q}g$.

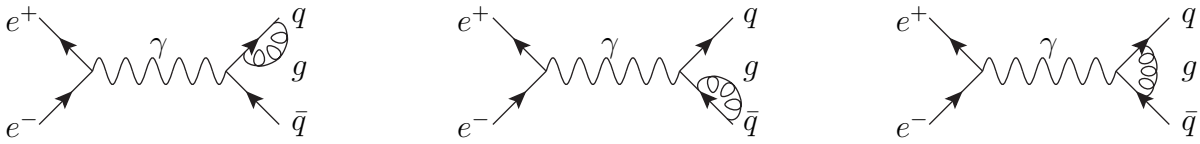

Figure 6: Virtual loop corrections to $e^+e^- \to q\bar{q}$.

way of doing this is to work in $d = 4 - 2\epsilon$ dimensions where to regularize these infrared divergences $\epsilon < 0$. In this case

$$\begin{aligned}
\sigma_{\text{real}} &= \sigma_0 C_F \frac{\alpha_S}{2\pi} H(\epsilon) \left(\frac{4}{\epsilon^2} + \frac{3}{\epsilon} + \frac{19}{2} - \pi^2 + \mathcal{O}(\epsilon) \right), \\
\sigma_{\text{virtual}} &= \sigma_0 C_F \frac{\alpha_S}{2\pi} H(\epsilon) \left(-\frac{4}{\epsilon^2} - \frac{3}{\epsilon} - 8 + \pi^2 + \mathcal{O}(\epsilon) \right),
\end{aligned}$$

where $H(0) = 1$. The sum

$$\sigma_{\text{total}} = \sigma_{\text{real}} + \sigma_{\text{virtual}} = \sigma_0 C_F \frac{3\alpha_S}{4\pi}, \tag{24}$$

is finite as $\epsilon \to 0$. So finally combining this correction with the leading-order result

$$R(e^+e^-) = R_0(e^+e^-) \left(1 + \frac{\alpha_s}{\pi} \right). \tag{25}$$

Measuring $R(e^+e^-)$ is one way of measuring the strong coupling giving[2]

$$\alpha_S(m_Z) = 0.1226 \pm 0.0038. \tag{26}$$

The second and third order corrections, and the results for the next-to-leading-order corrections including quark masses are also known.

This is the simplest example of an observable which we can calculate using perturbation theory involving quarks and gluons, but measure experimentally using hadrons. We now need to go on and consider more complicated observables.

[2]Taken from the Ref. [8].

3 Running Coupling

Figure 7: Example virtual corrections contributing to the evolution of the strong coupling constant.

In addition to the infrared, soft and collinear, divergences we saw in the calculation of $\sigma(e^+e^- \to \text{hadrons})$ it is possible to have ultraviolet divergences. The virtual corrections shown in Fig. 7 are divergent in the ultraviolet. These, and other similar corrections, lead to the strong coupling being *renormalized* to absorb the ultraviolet singularities. The renormalisation procedure introduces an unphysical renormalisation scale μ.

The leads to:

1. diagrams are dependent on μ;
2. α_S is replaced by the running coupling $\alpha_S(\mu)$;
3. although we can't calculate the coupling we can calculate how it changes with scale:

$$\mu^2 \frac{\mathrm{d}\alpha_S}{\mathrm{d}\mu^2} \equiv \beta(\alpha_S) = -\beta_0 \alpha_S^2 + \ldots \qquad \beta_0 = \frac{11N_c - 4T_R n_f}{12\pi}, \tag{27}$$

   where n_f is the number of active quark flavours.

For $\beta_0 > 0$ the coupling displays *asymptotic freedom*, *i.e.* $\alpha_S(\mu) \to 0$ as $\mu \to \infty$ which allows us to perform perturbative calculations at high energies where the coupling is small.

It is standard to quote the value of $\alpha_S(M_Z)$. The value at other scales can by found by solving the evolution equation. Recent experimental measurements of the strong coupling evolved to the Z^0 mass and the running of coupling are shown in Fig. 8.

It is common to define a scale Λ_{QCD} so that

$$\alpha_s(\mu) = \frac{4\pi}{\beta_0 \ln\left(\frac{\mu^2}{\Lambda^2_{\text{QCD}}}\right)} \left[1 + \ldots\right]. \tag{28}$$

In general there is a choice of precisely how we perform the renormalisation, which leads to both *renormalisation scale* and *scheme* dependence. Physical observables don't depend on μ_F or the renormalisation scheme, but fixed order perturbative calculations do.

3.1 Higher order calculations

Since the strong coupling constant is not very small the perturbative series converges slower than it does in QED. To get reliable QCD predictions we need at least NLO precision and NNLO is preferable for important processes, but NNLO calculations are very

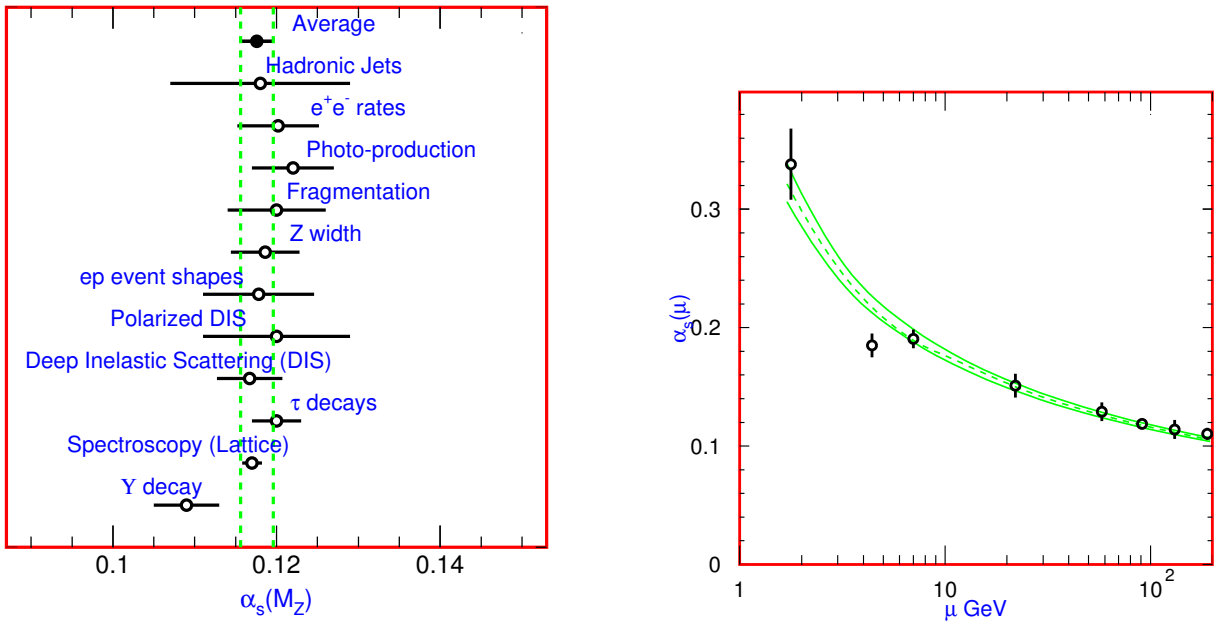

Figure 8: Measurements of the strong coupling at the Z^0 mass and the running of the coupling taken from Ref. [8].

challenging. Perturbative calculations for hadron colliders have two unphysical parameters: the factorisation and renormalisation scales. The former defines the separation between the perturbative and non-perturbative description of hte proton and the latter is needed to remove the ultra-violet divergences and specifies at which scale the coupling constant should be evaluated. This dependence is an artefact of the truncation of the perturbative series, if we were able to compute the entire perturbative series to all orders, the dependence would drop out. Therefore the dependence on the factorisation and renormalisation scales is used as a gauge of the theoretical error due to the missing orders.

3.2 Infrared safety

To enable a meaningful comparison between theory and experiment it is important that the observable is defined in a way that allows the perturbative prediction to be carried out at higher orders. One requirement is that the observable should be infrared safe. By this we mean that the value of the obervable does not change in the case of a collinear splitting or in the case of the emission of a soft particle. Mathematically it means that the observable $\mathcal{O}$ has to fullfil the following properties. For a collinear splitting of the parton with momentum p_i we need

$$\mathcal{O}(p_1, ..., p_i, ..., p_n) = \mathcal{O}(p_1, ..., zp_i, (1-z)p_i, ..., p_n)$$

and in the case of a parton's momentum p_j becoming soft we require

$$\begin{aligned} \mathcal{O}(p_1, ..., p_i, p_j, p_k, ..., p_n) &\rightarrow \mathcal{O}(p_1, ..., p_i, p_k, ..., p_n) \\ \text{for } p_j &\rightarrow 0\ . \end{aligned}$$

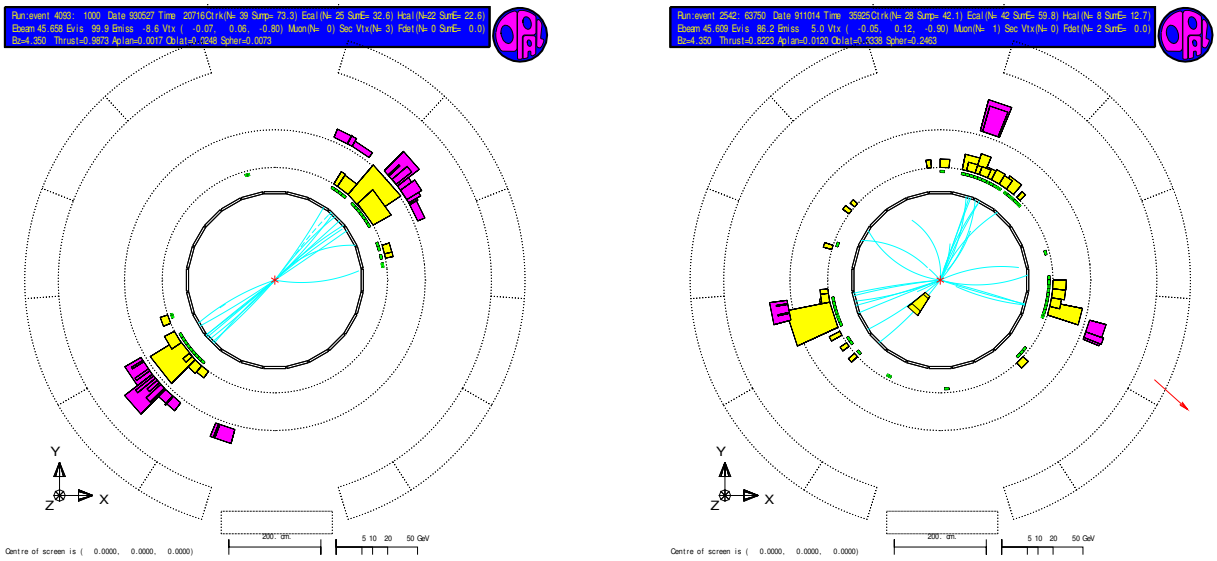

Figure 9: Example two and three jet e^+e^- events.

Examples of infrared unsafe observables or procedures are

- number of partons
- observables using incoming parton momentum fractions
- observables based on older jet algorithms
- using infrared unsafe observables as renormalisation or factorisation scale

It is not always easy to find out whether an observable/procedure is infrared safe, in order to so so correctly we will need to study the details of the jet clustering algorithm and the factorisation of the intial state in hadron collisions. The factorisation of short and long distance effects for hadronic inital states is covered in Section 4 while Section 6 covers details of different jet algorithms.

3.3 Event Shapes

If we consider the e^+e^- annihilation events shown in Fig. 9 we see a collimated bunch of hadrons travelling in roughly the same direction as the original quarks or gluons. Often you can "see" the jets without some fancy mathematical definition. We will come back and consider jets in more detail when we consider hadron–hadron collisions later in the course, in Section 6.

An alternative to defining jets is to define a more global measure of the event which is sensitive to the structure of the event. We need a number of properties to achieve this, the most important of which is *infrared safety*, *i.e.* if there is soft or collinear emission the answer doesn't change. Formally if a parton splits into two collinear partons

$$p \to zp + (1-z)p, \tag{29}$$

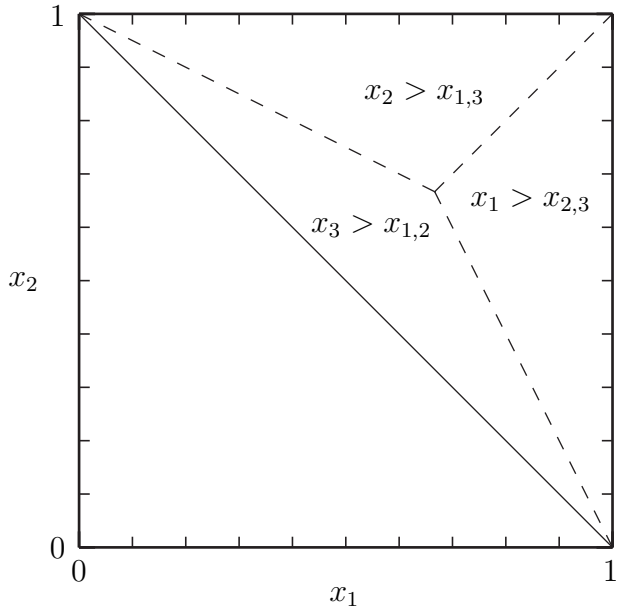

Figure 10: Phase space for $e^+e^- \to q\bar{q}g$. The requirement that $x_3 \leq 1$ ensures that $x_1 + x_2 \geq 1$ by momentum conservation so that physical phase space is the upper half plane.

or if a soft parton is emitted with momentum

$$p \to 0, \tag{30}$$

the result should not change.

After the total cross section, the simplest infrared safe observable is the thrust

$$T = \max_{\vec{n}} \frac{\sum_i |\vec{p}_i \cdot \vec{n}|}{\sum_i |\vec{p}_i|}, \tag{31}$$

where the sum is over all the final-state particles and the direction of the unit vector $\vec{n}$, the thrust axis, is chosen to maximize the projection of the momenta of the final-state particles along that direction.

For a two-jet *pencil-like* event all the particles lie along the thrust axis giving $T = 1$. For a totally *spherical* event the thrust can be calculated by taking a spherical distribution of particles in the limit of an infinite number of particles giving $T = \frac{1}{2}$. For three partons the thrust axis will lie along the direction of the most energetic parton, by momentum conservation there is an equal contribution to the thrust from the other partons giving $T = \max\{x_1, x_2, x_3\}$.

In order to calculate the differential cross section with respect to the thrust for $e^+e^- \to q\bar{q}g$ we can start from the differential cross section in Eqn. 12. In many cases when we wish to introduce a new quantity into a differential cross section it is easier to insert the definition using a δ-function rather than performing a Jacobian transform, in this case we use

$$1 = \int \mathrm{d}T \delta(T - \max\{x_1, x_2, x_3\}), \tag{32}$$

to give

$$\frac{\mathrm{d}\sigma}{\mathrm{d}T} = \sigma_0 C_F \frac{\alpha_S}{2\pi} \int \mathrm{d}x_1 \mathrm{d}x_2 \frac{x_1^2 + x_2^2}{(1-x_1)(1-x_2)} \delta(T - \max\{x_1, x_2, x_3\}), \tag{33}$$

where σ_0 is the leading-order cross section for $e^+e^- \to q\bar{q}$. This expression can be evaluated in each of the three phase-space regions shown in Fig. 10. First in the region where $x_1 > x_{2,3}$

$$\begin{aligned} \left.\frac{\mathrm{d}\sigma}{\mathrm{d}T}\right|_{x_1>x_{2,3}} &= \sigma_0 C_F \frac{\alpha_S}{2\pi} \int_{2(1-T)}^{T} \mathrm{d}x_2 \frac{T^2 + x_2^2}{(1-T)(1-x_2)} \\ &= \sigma_0 C_F \frac{\alpha_S}{2\pi} \frac{1}{1-T} \int_{2(1-T)}^{T} \mathrm{d}x_2 \frac{T^2+1}{(1-x_2)} - (1+x_2), \end{aligned} \tag{34}$$

where we have used the δ-function to integrate over x_1 and the limits on x_2 are given by $x_2 = x_1 = T$ for the upper limit and $T = x_1 = x_3 = 2 - x_1 - x_2 = 2 - T - x_2$ for the lower limit. Performing the integral gives

$$\left.\frac{\mathrm{d}\sigma}{\mathrm{d}T}\right|_{x_1>x_{2,3}} = \sigma_0 C_F \frac{\alpha_S}{2\pi} \frac{1}{1-T} \left[(T^2+1) \ln\left(\frac{2T-1}{1-T}\right) + 4 - 7T + \frac{3}{2}T^2 \right]. \tag{35}$$

The same result is obtained in the region $x_2 > x_{1,3}$ due to the symmetry of the formulae under $x_1 \leftrightarrow x_2$.

In the final region we can take the integrals to be over $x_{2,3}$ and use the δ-function to eliminate the integral over x_3 giving

$$\begin{aligned} \left.\frac{\mathrm{d}\sigma}{\mathrm{d}T}\right|_{x_3>x_{1,2}} &= \sigma_0 C_F \frac{\alpha_S}{2\pi} \int_{2(1-T)}^{T} \mathrm{d}x_2 \frac{(2-T-x_2)^2 + x_2^2}{(T+x_2-1)(1-x_2)}, \\ &= \sigma_0 C_F \frac{\alpha_S}{2\pi} \int_{2(1-T)}^{T} \mathrm{d}x_2 \frac{1}{T} \left[(2-T-x_2)^2 + x_2^2\right] \left[\frac{1}{T+x_2-1} + \frac{1}{1-x_2}\right], \\ &= \sigma_0 C_F \frac{\alpha_S}{2\pi} \frac{2}{T} \left[(2 - 2T + T^2) \ln\left(\frac{2T-1}{1-T}\right) + 2T - 3T^2 \right], \end{aligned} \tag{36}$$

where after the integral over x_3, $x_1 = 2 - x_2 - T$ and the limits are calculated in the same way as before.

Putting the results from the three regions together gives

$$\frac{\mathrm{d}\sigma}{\mathrm{d}T} = \sigma_0 C_F \frac{\alpha_S}{2\pi} \left[\frac{2}{T(1-T)} (3T(T-1)+2) \ln\left(\frac{2T-1}{1-T}\right) + \frac{3(3T-2)(T-2)}{1-T} \right]. \tag{37}$$

This result clearly diverges as $T \to 1$, indeed in this limit

$$\frac{1}{\sigma_0}\frac{\mathrm{d}\sigma}{\mathrm{d}T} \xrightarrow{T\to 1} -C_F \frac{\alpha_S}{2\pi} \left[\frac{4}{(1-T)} \ln(1-T) + \frac{3}{1-T} \right]. \tag{38}$$

We can use this result to define a two- and three-jet rate so that the three jet rate is

$$R_3(\tau) = \int_{\frac{1}{2}}^{1-\tau} \frac{1}{\sigma_0}\frac{\mathrm{d}\sigma}{\mathrm{d}T} \xrightarrow{\tau\to 0} C_F \frac{\alpha_S}{2\pi} 2 \ln^2 \tau, \tag{39}$$

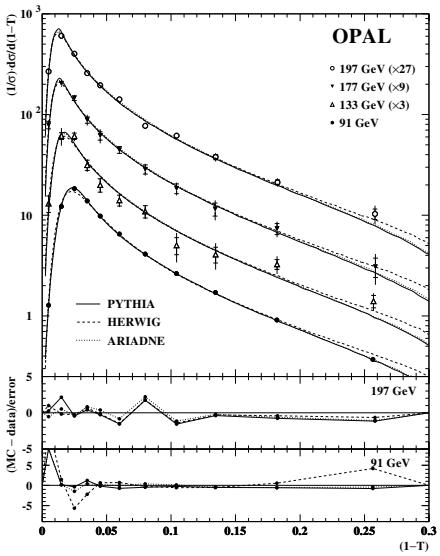

Figure 11: Thrust distribution at various centre-of-mass energies compared with Monte Carlo simulations, taken from Ref. [9].

and the two jet rate

$$R_2(\tau) = 1 - R_3(\tau) \stackrel{\tau\to 0}{\longrightarrow} 1 - C_F \frac{\alpha_S}{2\pi} 2\ln^2\tau. \tag{40}$$

Similar logarithmically enhanced terms appear at all orders in the perturbative expansion giving an extra $\ln^2\tau$ at every order in α_S, *i.e.*

$$R_2(\tau) \equiv \int_{1-\tau}^{1} \mathrm{d}T \frac{1}{\sigma}\frac{\mathrm{d}\sigma}{\mathrm{d}T} \stackrel{\tau\to 0}{\sim} 1 - C_F\frac{\alpha_S}{2\pi}2\ln^2\tau + \left(C_F\frac{\alpha_S}{2\pi}\right)^2 2\ln^4\tau + \ldots \tag{41}$$

Although α_S is small, $\ln^2\tau$ in large so the perturbative expansion breaks down. The solution is to resum the large $\alpha_S^n \ln^{2n}\tau$ terms to all orders giving the *Sudakov Form Factor*

$$R_2(\tau) \stackrel{\tau\to 0}{\sim} \exp\left[-C_F\frac{\alpha_S}{2\pi}2\ln^2\tau\right]. \tag{42}$$

This is finite (zero) at $\tau = 0$, *i.e.* the probability for no gluon radiation is zero. In general the Sudakov form factor gives the probability of no radiation

$$P(\text{no emission}) = \exp\left[-\hat{\mathrm{P}}_{\text{naive}}(\text{emission})\right]. \tag{43}$$

An example of the experimental measurement of the thrust distribution is shown in Fig. 11 compared to various Monte Carlo simulations which include resummation of these large logarithmic contributions..

4 Deep Inelastic Scattering

Historically measurements of deep inelastic scattering were very important for establishing the nature of QCD. Nowadays they are mainly important for the measurement of the parton distribution functions we need to calculate all cross sections for processes with incoming hadrons. As the proton isn't fundamental at sufficiently high energies the scattering is from the constituent quarks and gluons.

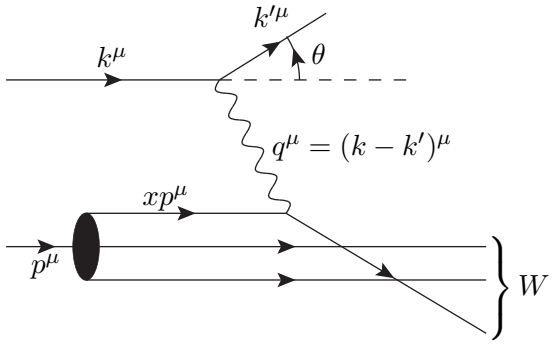

Figure 12: Deep inelastic scattering kinematics.

In deep inelastic scattering processes it is conventional to use the kinematic variables shown in Fig. 12. The struck parton carries a fraction x of the four-momentum of the incoming hadron. The four-momentum of the exchanged boson is q and the virtuality of the boson $Q^2 = -q^2$. Using momentum conservation

$$xp + q = p', \tag{44}$$

where p' is the 4-momentum of the scattered quark. Therefore $(xp + q)^2 = 0$ giving $x = \frac{Q^2}{2p\cdot q}$. Similarly the mass of the hadronic system is $W^2 = (p + q)^2$. By definition $(k + p)^2 = 2k \cdot p = s$ and therefore y$= \frac{p\cdot q}{p\cdot k} = \frac{Q^2}{xs}$.

Deep inelastic scattering has $Q^2 \gg M^2$ (deep) and $W^2 \gg M^2$ (inelastic), where M is the proton mass. Historically the observation and understanding of DIS was one of the key pieces of evidence for quarks. On general grounds the cross section has the form

$$\frac{\mathrm{d}^2\sigma}{\mathrm{d}x\mathrm{d}Q^2} = \frac{4\pi\alpha^2}{xQ^4}\left[y^2 xF_1(x,Q^2) + (1-y)F_2(x,Q^2)\right], \tag{45}$$

which parameterizes the cross section in terms of two unknown structure functions, $F_{1,2}(x, Q^2)$. If we consider that the proton is a bound state of partons we can calculate these structure functions.

Suppose that the probability of a given type of quark carrying a fraction η of the proton's momentum is $f_q(\eta)$ the cross section for hadron scattering can be written in terms of those for partonic scattering

$$\frac{\mathrm{d}^2\sigma(e + \text{proton})}{\mathrm{d}x\mathrm{d}Q^2} = \sum_q \int_0^1 \mathrm{d}\eta f_q(\eta)\frac{\mathrm{d}^2\sigma(e + q(\eta p))}{\mathrm{d}x\mathrm{d}Q^2}. \tag{46}$$

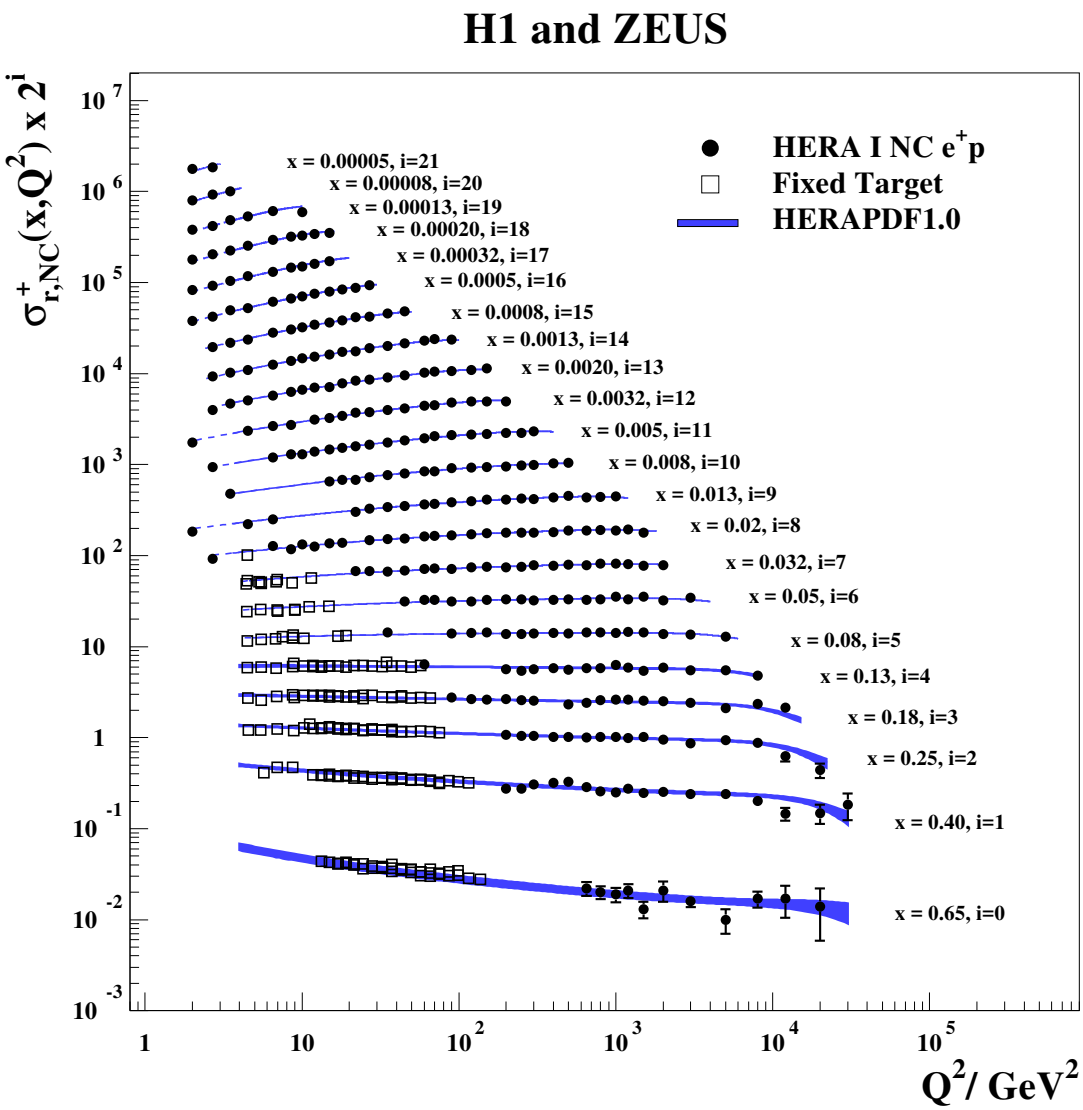

Figure 13: The reduced cross section, which is equivalent to F_2 up to some small corrections, measured by the H1 and ZEUS experiments from Ref. [10].

Taking the outgoing parton to be on-shell:

$$(q + \eta p)^2 = 2\eta p \cdot q - Q^2 = 0 \qquad \Rightarrow \qquad \eta = x.$$

Therefore

$$\frac{\mathrm{d}^2\sigma(e + \text{proton})}{\mathrm{d}x\mathrm{d}Q^2} = \sum_q f_q(x) \frac{\mathrm{d}^2\sigma(e + q(xp))}{\mathrm{d}Q^2}. \tag{47}$$

The differential cross section for $e^\pm(k) + q(p) \to e^\pm(k') + q(p')$ via photon exchange which

dominates at low Q^2 for neutral current scattering is

$$\frac{\mathrm{d}^2\sigma(e+q(xp))}{\mathrm{d}Q^2} = \frac{2\pi\alpha^2 e_q^2}{Q^4}\left[1+(1-y)^2\right], \tag{48}$$

where e_q is the charge of the quark.

So in the naive parton model

$$\begin{aligned} 2xF_1(x) &= F_2(x), \\ F_2(x) &= x\sum_q e_q^2 f_q(x), \end{aligned} \tag{49}$$

are functions of x only, *Bjorken scaling*. Bjorken scaling works reasonably well, see Fig. 13, but the quantum corrections, lead to *scaling violations*.

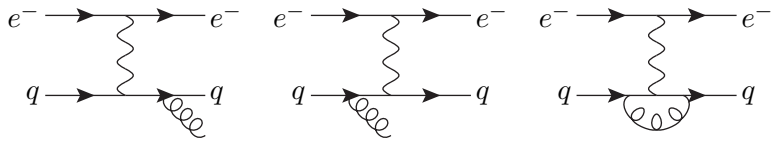

Figure 14: Real and virtual corrections to DIS.

If we consider the $\mathcal{O}(\alpha_S)$ corrections we have the following divergent contributions:

1. soft gluon, $E_g \to 0$;
2. gluon collinear to the final-state quark;
3. gluon collinear to the initial-state quark;
4. the virtual matrix element has a negative divergence;

corresponding to the diagrams shown in Fig. 14.

The contributions from (1), (2) and (4) are indistinguishable from the tree-level configuration and the divergences cancel between the real and virtual corrections. However (3) has momentum fraction $\eta > x$ and (4) $\eta = x$ so the initial-state divergences don't cancel.

Just as with final-state radiation in the collinear limit it can be shown that

$$\mathrm{d}\sigma_{q\to qg} \to \mathrm{d}\sigma_{q\to q} \times \frac{\alpha_S}{2\pi} C_F \frac{1+z^2}{1-z}\frac{\mathrm{d}t}{t}\frac{\mathrm{d}z}{z}. \tag{50}$$

Here we have the unregularized DGLAP splitting function $\hat{P}_{q\to qg}$, it is singular as $z \to 1$. The virtual contribution contains a compensating singularity at exactly $z = 1$. The

regularized splitting function is defined to be the sum of real and virtual contributions[3]

$$\begin{aligned} P_{qq}(z) &= C_F \frac{1+z^2}{1-z} + C_F \delta(1-z) \left\{ \frac{3}{2} - \int_0^1 \mathrm{d}z' \frac{2}{1-z'} \right\}, \\ &\equiv C_F \left(\frac{1+z^2}{(1-z)_+} + \frac{3}{2}\delta(1-z) \right). \end{aligned} \tag{51}$$

The total contribution is

$$\begin{aligned} F_2(x,Q^2) &= x \sum_q e_q^2 \int_x^1 \frac{\mathrm{d}\eta}{\eta} f_q(\eta) \left[\delta\left(1-\frac{x}{\eta}\right) \right. \\ &\quad \left. + \frac{\alpha_S}{2\pi} P_{qq}\left(\frac{x}{\eta}\right) \int_0 \frac{\mathrm{d}t}{t} + \bar{R}_{qq}\left(\frac{x}{\eta}\right) \right], \end{aligned} \tag{52}$$

where $\bar{R}_{qq}\left(\frac{x}{\eta}\right)$ is a calculable finite correction.

The integral over t is infrared divergent, comes from long timescales and should be part of the hadronic wavefunction. We therefore introduce a factorization scale μ_F and absorb contributions with $t < \mu_F$ into the parton distribution function so that $f_q(\eta)$ becomes $f_q(\eta, \mu_F^2)$.

$$\begin{aligned} F_2(x,Q^2) &= x \sum_q e_q^2 \int_x^1 \frac{\mathrm{d}\eta}{\eta} f_q(\eta,\mu_F^2) \left[\delta\left(1-\frac{x}{\eta}\right) \right. \\ &\quad \left. + \frac{\alpha_S}{2\pi} P_{qq}\left(\frac{x}{\eta}\right) \ln\frac{Q^2}{\mu_F^2} + R_{qq}\left(\frac{x}{\eta}\right) \right]. \end{aligned} \tag{53}$$

The finite piece is dependent on exactly how we define the parton distribution function, the factorization scheme dependence. Physical cross sections are independent of μ_F, however at any finite order in perturbation theory they do depend on the factorization scale.

Recall that in perturbation theory we cannot predict $\alpha_S(M_Z)$ but we can predict its evolution, Eqn. 27. Similarly for the PDFs

$$\mu_F^2 \frac{\partial f_q(x, mu_F^2)}{\partial \mu_F^2} = \frac{\alpha_S(\mu_F^2)}{2\pi} \int_x^1 \frac{\mathrm{d}y}{y} f_q(y,\mu_F^2) P_{qq}\left(\frac{x}{y}\right) + \ldots \tag{54}$$

5 Hadron Collisions

In hadron collisions QCD processes dominate due to strength of the strong coupling. The cross sections for electroweak processes, $W^\pm$, Z^0 and Higgs production are much smaller. The values of x and Q^2 probed in hadron collisions and examples of the cross sections for various processes are shown in Fig. 15. In this section we will look at some of the basics

[3]The +-prescription is defined by convolution with a well defined function, $g(z)$, such that

$$\int_0^1 \mathrm{d}z \left[f(z)\right]_+ g(z) = \int_0^1 \mathrm{d}z f(z) \left[(g(z) - g(1))\right].$$

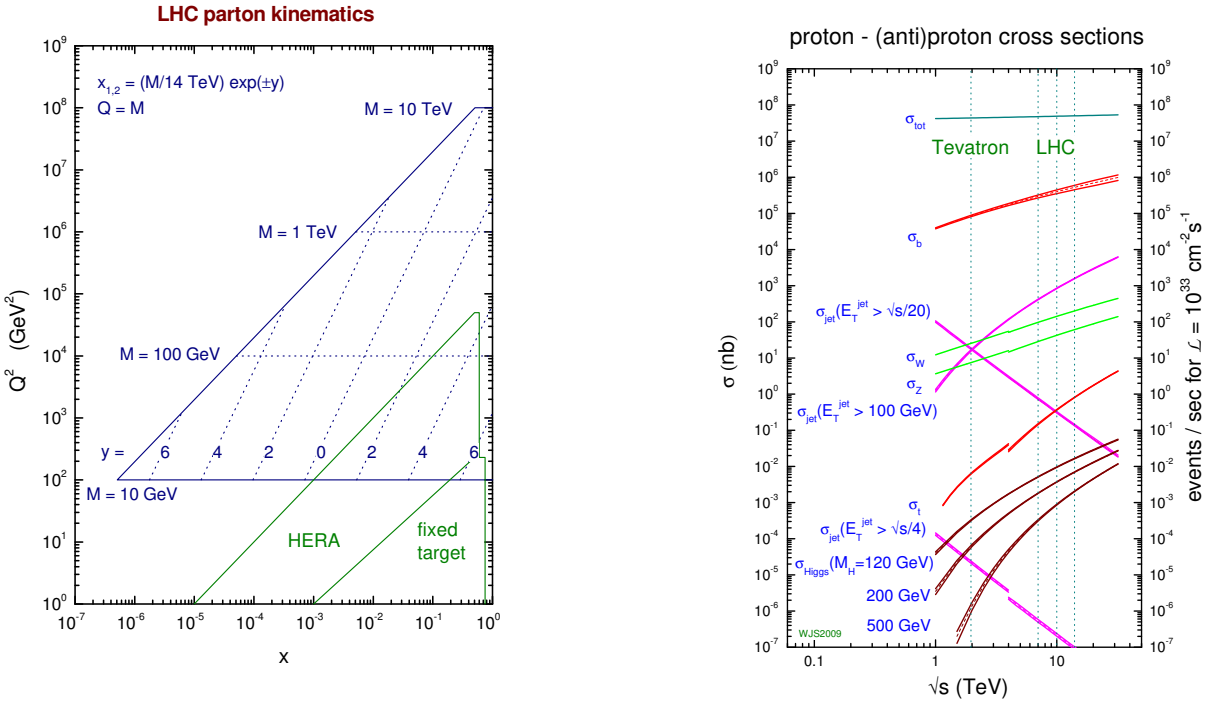

Figure 15: The values of x and Q^2 probed in hadron collisions and examples of the cross sections for various processes taken from Ref. [11].

of the production of the Z^0 boson, as a simple example of a hadron–hadron process, in the next section we will go on and study the physics of jets.

The calculation of the cross section for the production of an s-channel resonance in hadron–hadron collisions is described in more detail in Appendix A.3.1 where the cross section is given in Eqn. 128. The only dependence of the cross section on the rapidity of the Z^0 boson is via the PDFs, *i.e.* the rapidity distribution of Z^0 contains information on the PDFs of the partons a and b. The higher the mass of the produced system the more central it is, see Fig. 15. The Z^0 boson is centrally produced in both $p\bar{p}$ and pp collisions. The experimental results, for example those from the Tevatron shown in Fig. 16, are in good agreement with the theoretical predictions.

At leading order the transverse momentum of the gauge boson is zero. As before we have include real and virtual corrections, as shown in Fig. 17. In the same way as DIS the initial-state singularities must be factorized into the PDFs. At low transverse momentum we need to resum the multiple soft emissions whereas, as with the e^+e^- event shapes, at large $p_\perp$ the fixed-order approach is more reliable. The transverse momentum of the Z^0 boson at the Tevatron is shown in Fig. 18.

In hadron-hadron collisions we would like at least next-to-leading order (NLO) calculations. This is the first order at which we have a reliable calculation of the cross section. If possible we would like next-to-next-to-leading order (NNLO) calculations but

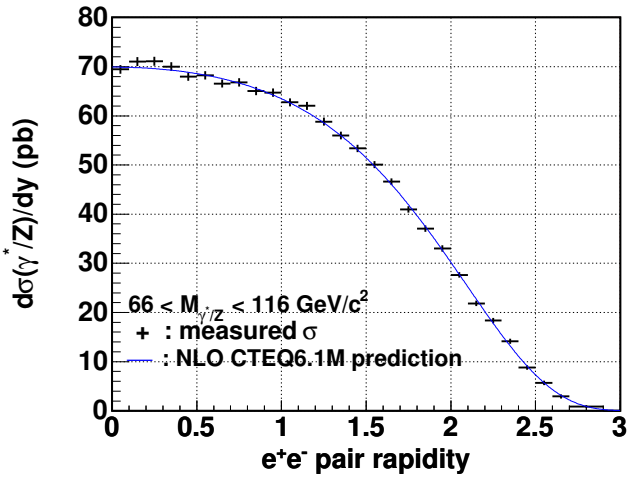

Figure 16: Rapidity of the Z^0 boson measured by the CDF experiment, taken from Ref. [12].

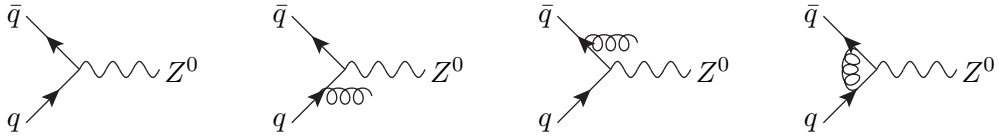

Figure 17: Real and virtual corrections to the production of the Z^0 boson.

that is much harder and takes a long time, *e.g.* $e^+e^- \to 3\,\text{jets}$ was calculated at: LO in 1974 [15]; NLO in 1980 [16]; NNLO in 2007 [17]. Calculating NNLO corrections is still extremely challenging in hadron collisions, only the Drell-Yan process and $gg \to H$ are known. However, we need higher order calculations because while the factorization scale uncertainty is significantly less at NLO when compared to leading order it can still be significant, see for example the scale uncertainty on the rapidity of the Z^0 boson shown in Fig. 19.

6 Jets

While we can often see the jets in an event when we look at an event display we need a precise definition to perform quantitative analyzes.[4] Jets are normally related to the underlying perturbative dynamics, *i.e.* quarks and gluons. The purpose of a *jet algorithm* is to reduce the complexity of the final state, combining a large number of final-state particles to a few jets, *i.e.*

$$\{p_i\} \overset{\text{jet algorithm}}{\longrightarrow} \{j_l\}. \tag{55}$$

We need a number of properties to achieve this (Snowmass accord):

[4] This section is based on the excellent review *Towards Jetography* [6].

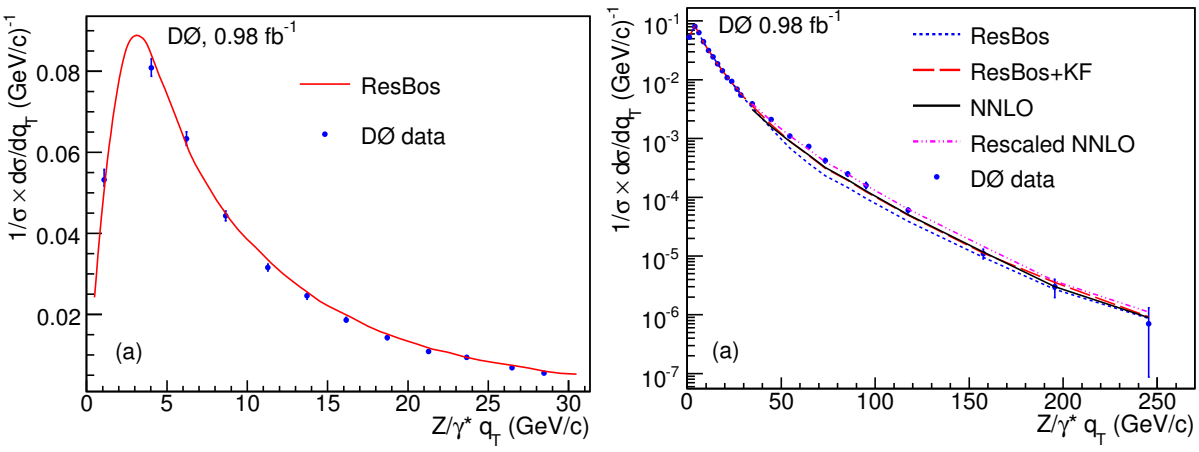

Figure 18: Transverse momentum of the Z^0 boson measured by the D0 experiment at the Tevatron, taken from Ref. [13].

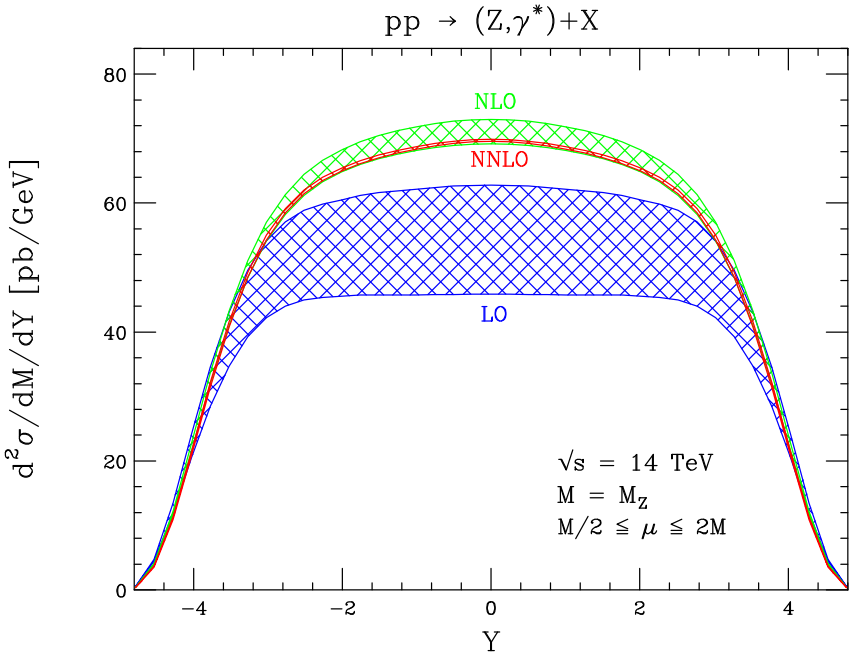

Figure 19: Rapidity distribution of the Z^0 boson for the LHC at $\sqrt{s} = 14\,\text{TeV}$, taken from Ref. [14].

- simple to implement in experimental analyzes and theoretical calculations;
- defined at any order in perturbation theory and gives finite cross sections at any order in perturbation theory (*i.e.* infrared safe);
- insensitive to hadronization effects.

The most important of these properties is *infrared safety*, as with the event shapes we

considered earlier. Provided the jet algorithm is infrared safe there are a range of different approaches.

The two main types of jet algorithm are:

1. cone algorithms;

2. sequential recombination algorithms.

There is a long history to this subject with: theorists and e^+e^- experimentalists generally preferring recombination algorithms for their better theoretical properties; hadron collider experimentalists preferring cone algorithms for their more intuitive picture and because applying many experimental corrections was easier. However, with the start of the LHC we have converged on a specific recombination algorithm.

6.1 Cone Algorithms

The simplest, oldest, and most intuitively appealing idea is a cone algorithm. The most widely used algorithms are *iterative cone* algorithms where the initial direction of the cone is determined by a seed particle, i. The sum of the momentum of all the particles with a cone of radius R, the jet radius, in the azimuthal angle ϕ and rapidity[5] y is then used as a new seed direction and the procedure iterated until the direction of the resulting cone is stable. In this approach the momenta of all the particles j such that

$$\Delta R_{ij}^2 = (y_i - y_j)^2 + (\phi_i - \phi_j)^2 < R^2, \tag{56}$$

are summed. As these algorithms are almost exclusively used in hadron–hadron collisions it is normal to use the kinematically variables defined in Appendix A.1.

While this may seem simple there are a lot of complications in the details of the algorithm in particular: what should be used as the seeds; what happens when the cones obtained from two different seeds share particles, *overlap*. The details of the treatment of these issues can lead to problems with infrared safety, which can often be very subtle.

Consider a simple approach where we take all the particles to be seeds. If we have two partons separated in (y, ϕ) by twice the cone radius then two jets, with the direction

a) Seed particles b) Jet Cones

Figure 20: Example of cone jets.

given by that of the original partons, are formed as shown in Fig. 20. However if there is an additional soft gluon emission between the two jets, as shown in Fig. 21, depending on

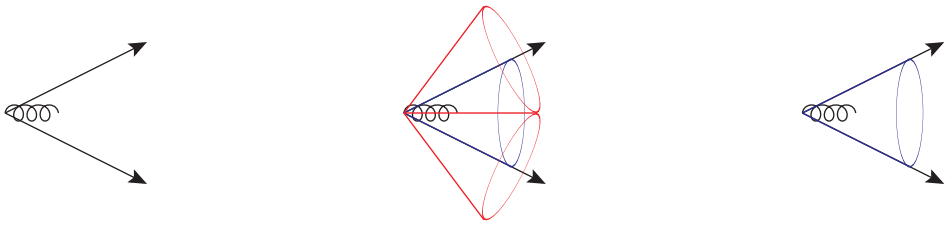

a) Seed particles b) Search cones c) Cone jets

Figure 21: Example of cone jets with additional soft radiation.

the approach we can get only one jet, *i.e.* the algorithm is unsafe. A simple solution was to use the midpoint between all the seeds as a seed, the *midpoint algorithm*. This solves the problem at this level but similar problems appear for higher multiplicities. The final solution, for the only known infrared safe cone algorithm, SISCone, is to avoid the use of seeds and treat overlapping jets carefully.

6.2 Sequential Recombination Algorithms

In this approach jets are constructed by sequential recombination. We define a distance measure between two objects d_{ij}, in hadron collisions we must also define a distance measure d_{iB} with respect to the beam direction. There are two variants of the algorithm the *inclusive* where all jets are retained and *exclusive* where only jets above the cut-off value of the jet measure d_{cut}, the jet resolution scale, are kept. The algorithm proceeds as follows:

1. the distance measure is computed for each pair of particles, and with the beam direction in hadronic collisions, and the minimum found;

2. if the minimum value is for a final-state merging in the exclusive approach the particles i and j are recombined into a pseudoparticle if $d_{ij} \leq d_{\text{cut}}$, while in the inclusive algorithm they are always recombined;

3. otherwise if a beam merging is selected in the in inclusive approach the particle is declared to be a jet, while in the exclusive approach it is discarded if $d_{iB} \leq d_{\text{cut}}$;

4. in the inclusive approach we continue until no particles remain, while in the exclusive approach we stop when the selected merging has $\min\{d_{iB}, d_{ij}\} \geq d_{\text{cut}}$.

In the inclusive approach the jets are all those selected from merging with the beam, whereas in the exclusive approach the jets are all the remaining particles when the iteration is terminated.

The choice of the distance measure, and to a lesser extent the recombination procedure,[6] defines the algorithm.

[5] Or sometimes pseudorapidity η.

[6] In practice the so-called "E-scheme" where the four-momenta of the particles are added to give the pseudoparticle's four-momentum is almost always used.

The earliest JADE algorithm for e^+e^- collisions uses the distance measure

$$d_{ij} = 2E_iE_j\,(1-\cos\theta_{ij})\,, \tag{57}$$

where $E_{i,j}$ are the energies of the particles and θ_{ij} the angle between them. In e^+e^- collisions we have to use the exclusive algorithm and it is conventional to use a dimensionless measure $y_{ij} = d_{ij}/Q^2$, where Q is the total energy in the event. While this choice can easily be proved to be safe in the soft and collinear limits there are problems with the calculation of higher order corrections.

Therefore a class of k_T algorithms was developed in which the distance measure was chosen to be the relative transverse momentum of the two particles in the collinear limit, *i.e.*

$$d_{ij} = \min\{E_i^2, E_j^2\}\theta_{ij}^2 \simeq k_{\perp ij}^2 \quad \text{for } \theta_{ij} \to 0. \tag{58}$$

In e^+e^- collisions the conventional choice is

$$d_{ij} = 2\min\{E_i^2, E_j^2\}\,(1-\cos\theta_{ij})\,. \tag{59}$$

In hadron collisions it is best to use a choice which is invariant under longitudinal boosts along the beam direction. The standard choice is

$$d_{ij} = \min\{p_{i,\perp}^2,\, p_{j,\perp}^2\}\frac{\Delta R_{ij}^2}{R^2}, \tag{60}$$

where R is the "cone-size" and $p_{i,\perp}$ is the transverse momentum of particle i with respect to the beam direction. The standard choice for the beam distance is $d_{iB} = p_{i,\perp}^2$. There are other definitions, particularly of the distance d_{ij}, which are invariant under longitudinal boosts but that in Eqn. 60 is the most common choice.

In general there is a whole class of measures defined by

$$d_{ij} = \min\{p_{i,\perp}^{2p}, p_{j,\perp}^{2p}\}\frac{\Delta R_{ij}^2}{R}, \tag{61}$$

and $d_{iB} = p_{i,\perp}^{2p}$.

The parameter $p = 1$ for the k_T algorithm and 0 for the Cambridge/Aachen algorithm.

Recently a new approach, the anti-k_T algorithm, with $p = -1$, was proposed which favours clustering with hard collinear particles rather than clusterings of soft particles, as in the k_T and Cambridge/Aachen algorithms. The anti-k_T algorithm is still infrared safe and gives "conical" jets due to the angular part of the distance measure and is the algorithm preferred by both general-purpose LHC experiments.

6.3 Jet Cross Sections

All cone jet algorithms, expect from SISCone, are not infrared safe. The best ones typically fail in processes where we consider extra radiation from three-parton configurations while some already fail when we consider radiation from two-parton configurations, see the summary in Table 2.

Process	Last meaningful order		Known at
	JetClu Atlas cone	MidPoint CMS cone	
inclusive jet cross section	LO	NLO	NLO ($\rightarrow$ NNLO)
$W^{\pm}/Z^0 + 1$-jet cross section	LO	NLO	NLO
3-jet cross section	none	LO	NLO
$W^{\pm}/Z^0 + 2$-jet cross section	none	LO	NLO
jet masses in 3-jet and $W^{\pm}/Z^0 + 2$-jet events	none	none	LO

Table 2: Comparisons of various cone algorithms for hadron–hadron processes. Adapted from Ref. [6].

Examples of the jets, and their areas, formed using different algorithms on a sample parton-level event are shown in Fig. 22. As can be seen the k_T and Cambridge/Aachen algorithms tend to cluster many soft particles giving jets with an irregular area whereas the jets produced by the cone and anti-k_T algorithms are more regular making applying corrections for pile-up and underlying event contamination easier.

In order to study jet production in hadron collisions we need to understand both the jet algorithm and the production of the partons which give rise to the jets. The spin/colour summed/average matrix elements are given in Table 3. Many of these matrix elements have t-channel dominance, typically $t \rightarrow 0 \Longleftrightarrow p_\perp^2 \rightarrow 0$. As a consequence the parton–parton scattering cross section grows quickly as $p_\perp \rightarrow 0$ an effect which is further enhanced by the running of α_s when using $\mu_R = p_\perp$ as the renormalisation scale. An example of the $p_\perp$ spectrum of jets for different rapidities measured using the midpoint cone-algorithm is shown in Fig. 23.

$qq' \rightarrow qq'$	$\frac{4}{9}\frac{\hat{s}^2+\hat{u}^2}{\hat{t}^2}$
$q\bar{q} \rightarrow q'\bar{q}'$	$\frac{4}{9}\frac{\hat{t}^2+\hat{u}^2}{\hat{s}^2}$
$q\bar{q} \rightarrow gg$	$\frac{32}{27}\frac{\hat{t}^2+\hat{u}^2}{\hat{t}\hat{u}} - \frac{8}{3}\frac{\hat{t}^2+\hat{u}^2}{\hat{s}^2}$
$qg \rightarrow qg$	$\frac{\hat{s}^2+\hat{u}^2}{\hat{t}^2} - \frac{4}{9}\frac{\hat{s}^2+\hat{u}^2}{\hat{s}\hat{u}}$
$gg \rightarrow q\bar{q}$	$\frac{1}{6}\frac{\hat{t}^2+\hat{u}^2}{\hat{t}\hat{u}} - \frac{3}{8}\frac{\hat{t}^2+\hat{u}^2}{\hat{s}^2}$
$gg \rightarrow gg$	$\frac{9}{2}\left(3 - \frac{\hat{t}\hat{u}}{\hat{s}^2} - \frac{\hat{s}\hat{u}}{\hat{t}^2} - \frac{\hat{s}\hat{t}}{\hat{u}^2}\right)$
$q\bar{q} \rightarrow g\gamma$	$\frac{8}{9}\frac{\hat{t}^2+\hat{u}^2+2\hat{s}(\hat{s}+\hat{t}+\hat{u})}{\hat{t}\hat{u}}$
$qg \rightarrow q\gamma$	$-\frac{1}{3}\frac{\hat{s}^2+\hat{u}^2+2\hat{t}(\hat{s}+\hat{t}+\hat{u})}{\hat{s}\hat{u}}$

Table 3: Spin and colour summed/averaged matrix elements for $2 \rightarrow 2$ parton scattering processes with massless partons taken from Ref. [3]. A common factor of $g^4 = (4\pi\alpha_s)^2$ (QCD), $g^2e^2e_q^2$ (photon production) has been removed.

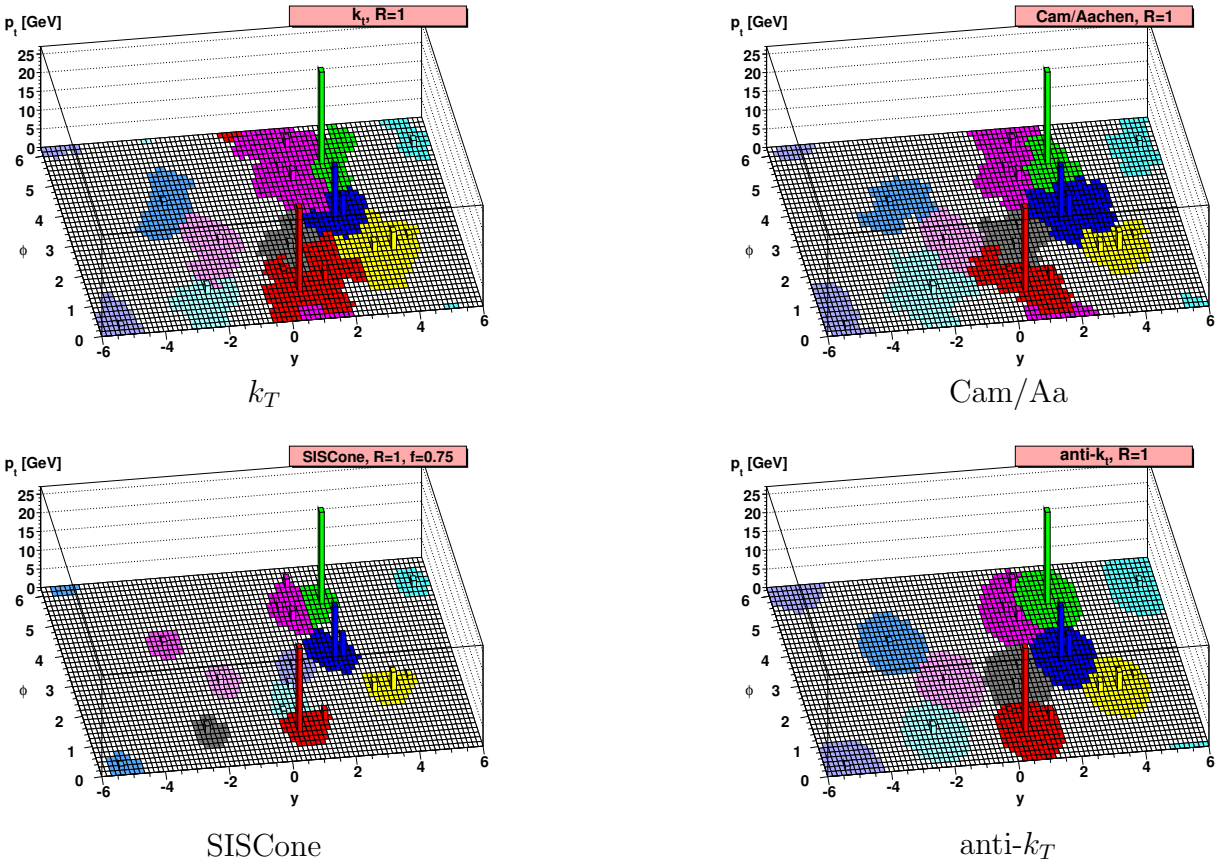

Figure 22: Examples of jets formed by different jet algorithms, taken from Ref. [6].

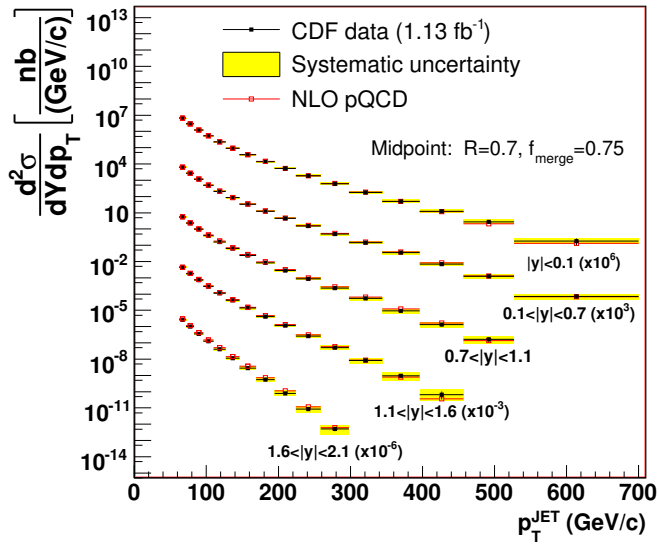

Figure 23: Transverse momentum spectrum of jets measured by the CDF experiment at the Tevatron, taken from Ref. [18].

6.4 Jet Properties

In general the computation of jet properties in hadron–hadron collisions is extremely complicated, however for some quantities we can get estimates of various effects. The simplest of these is to estimate the change in the $p_\perp$ between a parton and the jet it forms.

We can start by considering the change due to perturbative QCD radiation. Suppose we have a quark with transverse momentum $p_\perp$ which radiates a gluon such that the quark carries a fraction z of its original momentum and the gluon a fraction $1-z$, as shown in Fig. 24. In this case after the radiation the centre of the jet will be the parton

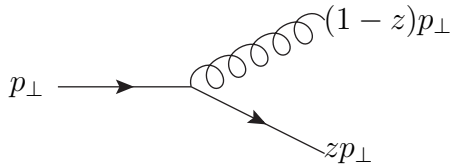

Figure 24: Kinematics of jet branching

with the highest transverse momentum after the branching, *i.e.* the quark if $z > 1-z$ or the gluon if $z < 1-z$. If the other parton is at an angular distance greater $\theta > R$ it will no longer be in the jet and the jet will have a smaller transverse momentum

$$\begin{aligned} \delta p_\perp &= (1-z)p_\perp - p_\perp && = -\,zp_\perp && 1-z > z \\ \delta p_\perp &= zp_\perp - p_\perp && = -\,(1-z)p_\perp && z > 1-z \end{aligned} \tag{62}$$

than the original parton.

We can use the splitting probabilities given in Eqn. 18 to compute the average transverse momentum loss

$$\begin{aligned} \langle p_\perp \rangle_q &= -\frac{C_F \alpha_S}{2\pi} p_\perp \int_{R^2}^1 \frac{\mathrm{d}\theta^2}{\theta^2} \int_0^1 \mathrm{d}z \frac{1+z^2}{1-z} \min\{1-z, z\}, \\ &= -\frac{C_F \alpha_S}{2\pi} p_\perp \ln\left(\frac{1}{R^2}\right) \left[\int_0^{\frac{1}{2}} \frac{1+z^2}{1-z} z + \int_{\frac{1}{2}}^1 \frac{1+z^2}{1-z} 1 - z \right], \\ &= -\frac{C_F \alpha_S}{\pi} p_\perp \ln\left(\frac{1}{R}\right) \left[2\ln 2 - \frac{3}{8} \right]. \end{aligned} \tag{63}$$

The loss of transverse momentum can be calculated for gluon jets in the same way using the gluon splitting functions giving

$$\langle p_\perp \rangle_g = -\frac{\alpha_S}{\pi} p_\perp \ln\left(\frac{1}{R}\right) \left[C_A \left(2\ln 2 - \frac{43}{96} \right) + T_R n_f \frac{7}{48} \right]. \tag{64}$$

These calculations give

$$\frac{\langle p_\perp \rangle_q}{p_\perp} = -0.43 \alpha_S \ln \frac{1}{R}, \qquad \frac{\langle p_\perp \rangle_g}{p_\perp} = -1.02 \alpha_S \ln \frac{1}{R}.$$

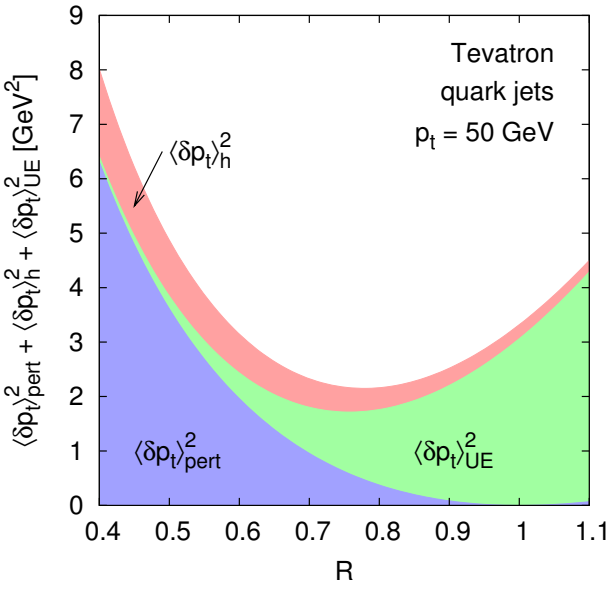

Figure 25: Example of various contributions to the shift of the transverse momentum, taken from Ref. [6].

So for a jet with $R = 0.4$ quark and gluon jets will have 5% and 11% less transverse momentum than the parent parton, respectively. These results are subject to significant finite R and higher order corrections. The result will also depend on the precise details of the recombination scheme, for example SISCONE has a different recombination scheme where the centre of the cone is the direction of the sum of the partons and we require one parton to fall outside the cone.

While this gives the perturbative energy loss by the jet there are other effects which can change the transverse momentum of the jet. In particular the jet can also lose energy in the hadronization process and can gain energy from the underlying event.

While these effects cannot be calculated from first principles we can use some simple models to gauge the size of the effects.

One model for the effect of hadronization on event shapes in e^+e^- collisions, due to Dokshitzer and Webber, is to perform a perturbative calculation and instead of stopping the calculation at some small energy scale μ_I because the strong coupling becomes non-perturbative continue the calculation into the infrared regime with a model of the strong coupling in this regime which does not diverge. They define

$$\mathcal{A}(\mu_I) = \frac{1}{\pi}\int_0^{\mu_I} \mathrm{d}k_\perp \alpha_S(k_\perp). \tag{65}$$

This model can also be used to assess the size of the hadronization corrections for the jet transverse momentum. The hadronization is modelled by soft gluons with $k_\perp \sim \Lambda_{\mathrm{QCD}}$. In this case the transverse momentum loss is

$$\delta p_\perp = z p_\perp - p_\perp = -(1-z)p_\perp. \tag{66}$$

As before the transverse momentum loss is

$$\langle p_\perp \rangle_q = -\frac{C_F}{2\pi} p_\perp \int \frac{\mathrm{d}\theta^2}{\theta^2} \int \mathrm{d}z \alpha_S \frac{1+z^2}{1-z}(1-z). \tag{67}$$

As we are dealing with soft gluons $z \sim 1$ so $1+z^2 \simeq 2$. In this case we will not use a fixed value of α_S but need to evaluate it at the scale of the transverse momentum of the gluon with respect to the quark $k_\perp = p_\perp(1-z)\theta$. We also transform the integration variables to use $k_\perp$ and θ giving

$$\langle p_\perp \rangle_q = -\frac{2C_F}{\pi} \int_R^1 \frac{\mathrm{d}\theta}{\theta^2} \int_0^{\mu_I} \mathrm{d}k_\perp \alpha_S(k_\perp) = -\frac{2C_F \mathcal{A}}{R}. \tag{68}$$

Using the coefficients from fits to the e^+e^- thrust distribution

$$\langle \delta p_\perp \rangle_q \sim -\frac{0.5\,\mathrm{GeV}}{R}, \qquad \langle \delta p_\perp \rangle_g \sim -\frac{1\,\mathrm{GeV}}{R}. \tag{69}$$

The hadronization correction has a $\frac{1}{R}$ dependence on the size of the jet, unlike the $\ln \frac{1}{R}$ dependence of the perturbative radiation.

We can estimate the underlying event contribution by assuming there is Λ_{UE} energy per unit rapidity due to soft particles from the underlying event giving a correction to the transverse momentum of

$$\langle \delta p_\perp \rangle = \Lambda_{\mathrm{UE}} \int_{\eta^2+\phi^2<R^2} \mathrm{d}\eta \frac{\mathrm{d}\phi}{2\pi} = \Lambda_{\mathrm{UE}} \frac{R^2}{2}. \tag{70}$$

This is a useful estimate although strictly the area of the jet is only πR^2 for the anti-k_T algorithm.

An example of the various contributions to the shift between the partonic and jet transverse momentum is shown in Fig. 25.

7 Electroweak Physics

The Standard Model has 18 parameters (assuming massless neutrinos):

- 6 quark and 3 charged lepton masses;
- 3 quark mixing angles and 1 phase;
- 1 strong coupling;
- 1 electromagnetic coupling and 3 boson masses, m_W, m_Z, m_h.

All observables are a function of these 18 parameters. In principle we could choose 18 well-measured observables and define them to be the fundamental parameters of the theory, *e.g.*

$$\alpha, \qquad G_F, \qquad \alpha_S, \qquad M_Z, \qquad M_h, \qquad m_f,$$

and calculate everything else in terms of them.

For the electroweak part of the theory we need m_t, m_h and three other parameters to specify everything, neglecting the masses of the other Standard Model fermions. Everything else can then be calculated from these parameters, *e.g.*

$$\cos\theta_W = \frac{m_W}{m_Z}, \qquad\qquad e = g\sin\theta_W.$$

The current values of the electroweak parameters are

$$m_W = 80.41\,\text{GeV}, \qquad m_Z = 91.188\,\text{GeV}, \quad \sin^2\theta_W = 0.231,$$
$$\alpha(m_Z) = \frac{1}{128.89}, \qquad G_F = 1.16639\times10^{-5}\,\text{GeV}^{-2}.$$

It is common to include the Fermi constant, $G_F = \frac{\sqrt{2}g^2}{8m_W^2}$, from the effective theory of weak interactions at low energies as a parameter.

Different choices for the input parameters give different values for the calculated parameters.

1. input: $\alpha(m_Z)$, G_F, $\sin^2\theta_W$, extracted:

$$g = \frac{4\pi\alpha(m_Z)}{\sin^2\theta_W} = 0.6497,$$

$$m_W = \frac{g}{\sqrt{4\sqrt{2}G_F}} = 79.98\,\text{GeV}, \qquad m_Z = \frac{m_W}{\cos\theta_W} = 91.20\,\text{GeV};$$

2. input: m_W, G_F, $\sin^2\theta_W$ extracted:

$$m_Z = \frac{m_W}{\cos\theta_W} = 91.695\,\text{GeV},$$

$$g = \sqrt{4\sqrt{2}G_F}m_W = 0.653, \qquad \alpha(m_Z) = \frac{g^2\sin^2\theta_W}{4\pi} = 1/127.51;$$

3. input: m_Z, $\alpha(m_Z)$, $\sin^2\theta_W$ extracted:

$$m_W = \frac{m_Z}{\cos\theta_W} = 79.97\,\text{GeV}, \qquad g = \frac{4\pi\alpha(m_Z)}{\sin\theta_W} = 0.6497;$$

4. input: m_Z, m_W, G_F extracted:

$$\sin^2\theta_W = 1 - \left(\frac{m_W}{m_Z}\right)^2 = 0.2224,$$

$$g = \sqrt{4\sqrt{2}G_F}m_W = 0.653, \qquad \alpha(m_Z) = \frac{g^2\sin^2\theta_W}{4\pi} = 1/132.42.$$

This is due to the quantum corrections.

It was the great triumph of the LEP/SLD and Tevatron physics programmes that the quantum corrections to the theory were probed. The normal choice of input parameters is:

1. $\alpha = 1/137.035999679(94)$ the fine-structure constant at $q^2 = 0$ is accurately measured, however the error on its evolution to $q^2 = m_Z^2$ has greater uncertainty due to hadronic corrections;

2. $G_F = 1.166367(5) \times 10^5\,\mathrm{GeV}^{-2}$ is very accurately measured in muon decay $\mu^- \to e^- \nu_\mu \bar{\nu}_e$;

3. $m_Z = 91.1876 \pm 0.0021\,\mathrm{GeV}$ from the LEP1 lineshape scan;

as these are the most accurately measured.

7.1 Quantum Corrections to Masses

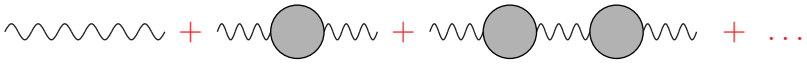

Figure 26: Example quantum corrections to the gauge boson propagator.

We have already considered the running of the coupling and corrections to cross sections and other observables. However masses are also renormalized in the Standard Model. If we consider the propagator for a massive gauge boson we get corrections of the form shown in Fig. 26. If we omit the Lorentz structures this gives a propagator

$$\begin{aligned} D(q^2) &= \frac{i}{q^2 - m^2} + \frac{i}{q^2 - m^2} i\Pi(q^2) \frac{i}{q^2 - m^2} \\ &\quad + \frac{i}{q^2 - m^2} i\Pi(q^2) \frac{i}{q^2 - m^2} i\Pi(q^2) \frac{i}{q^2 - m^2} + \ \ldots, \end{aligned}$$

where $\Pi(q^2)$ is the gauge boson self energy. This is a geometric progression, summing the series gives

$$D(q^2) = \frac{i}{q^2 - m^2} \frac{1}{1 - \frac{\Pi(q^2)}{q^2 - m^2}} = \frac{i}{q^2 - m^2 - \Pi(q^2)}. \tag{71}$$

If the particle can decay to the particles in the loop there is an imaginary part of the self energy $\Pi(q^2)$ which is related to the width of the particle

$$\mathrm{Im}\,\Pi(q^2) = -iq\Gamma(q). \tag{72}$$

The real part of the self energy correction renormalizes the particle's mass giving

$$D(q^2) = \frac{i}{q^2 - m_R^2(q) + iq\Gamma(q)}. \tag{73}$$

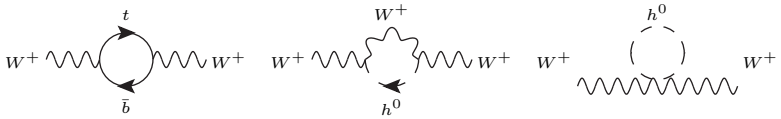

Figure 27: Quantum corrections to the $W^{\pm}$ boson mass.

As we have defined to the mass of the Z^0 boson to be a fundamental parameter $\delta m_Z^2 = 0$, by definition.

The dominant corrections to the W mass come from top-bottom and Higgs loop corrections, as shown in Fig. 27.

The correction to the $W^{\pm}$ boson mass is

$$\begin{aligned}\delta m_W^2 \;\sim\; & \frac{4s_W^2}{1-2s_W^2}\frac{G_F}{8\pi^2\sqrt{2}}m_W^2 \times \frac{c_W^2}{s_W^2}N_c\left(m_t^2 - m_b^2\right) \\ & -\frac{4s_W^2}{1-2s_W^2}\frac{G_F}{8\pi^2\sqrt{2}}m_W^2 \times m_W^2\frac{11}{3}\left(\ln\frac{M_h^2}{m_W^2} - \frac{5}{6}\right).\end{aligned}$$

7.2 Electroweak Observables

A number of observables are used in the electroweak fit performed by the LEP Electroweak Working Group (LEPEWWG):

1. the Z^0 mass and width m_Z, Γ_Z;

2. the hadronic cross section at the Z^0 pole $\sigma(\text{had}) \equiv \frac{12\pi\Gamma(e^+e^-)\Gamma(\text{had})}{m_Z^2\Gamma_Z^2}$;

3. the ratio of the hadronic to leptonic partial widths of the Z^0, $R_\ell \equiv \frac{\Gamma(\text{had})}{\ell^+\ell^-}$, and the ratio of the bottom, $R_b \equiv \Gamma(b\bar{b})/\Gamma(\text{had})$, and charm, $R_c \equiv \Gamma(c\bar{c})/\Gamma(\text{had})$, quark partial widths to the hadronic partial width of the Z^0;

4. the forward-backward asymmetry for $e^+e^- \to \bar{f}f$

$$A_{fb}^{0,f} = \frac{\sigma_F - \sigma_B}{\sigma_F + \sigma_B}, \tag{74}$$

   for charged leptons, $A_{fb}^{0,\ell}$, bottom $A_{fb}^{0,b}$, and charm $A_{fb}^{0,c}$ quarks;

5. the couplings of the fermions to the Z^0 can be extracted from the forward-backward asymmetry in polarized scattering at SLD

$$A_{LR}^{FB}(f) = \frac{\sigma_{LF}^f - \sigma_{LB}^f - \sigma_{RF}^f + \sigma_{RB}^f}{\sigma_{LF}^f + \sigma_{LB}^f + \sigma_{RF}^f + \sigma_{RB}^f} = \frac{3}{4}A_f. \tag{75}$$

   The couplings for the bottom, A_b, and charm, A_c, quarks can be extracted from these measurements. There are a number of possible ways of extracting A_ℓ;

6. $\sin^2\theta_{\text{eff}}^{\text{lept}}(Q_{fb})$ is extracted from the hadronic charge asymmetry;

7. the W mass, m_W, and width, Γ_W are measured in a range of ways;

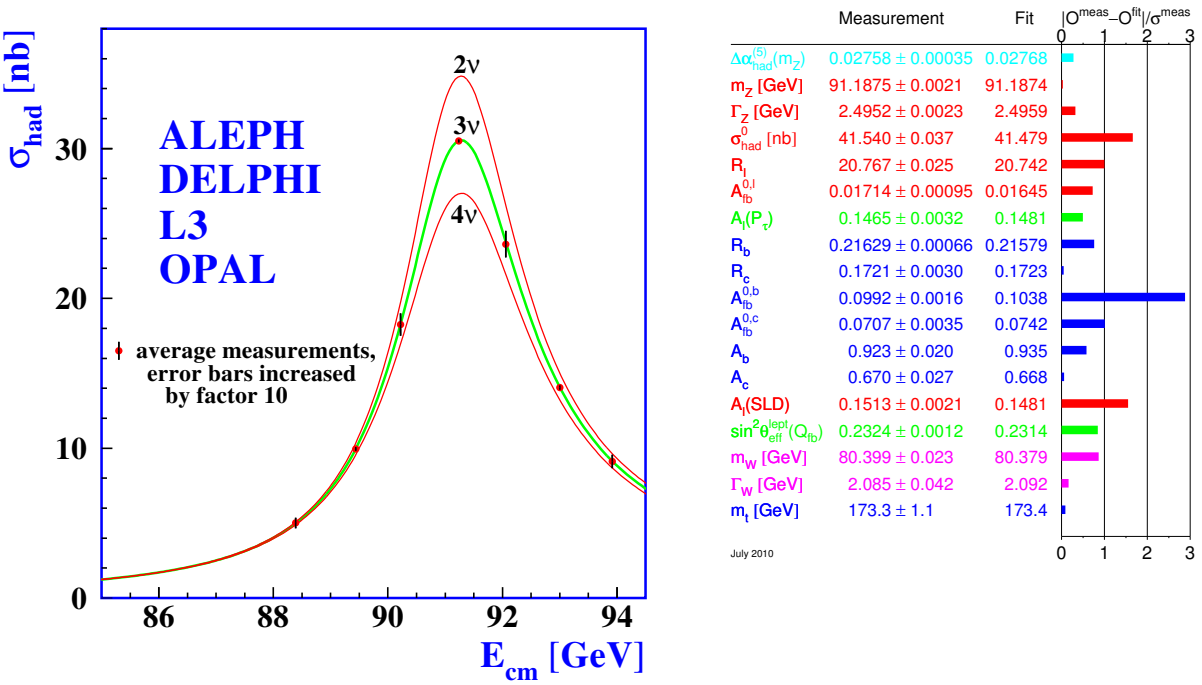

Figure 28: The lineshape of the Z boson and results of the precision electroweak fit taken from the LEPEWWG.

8. the top quark mass, m_t, is measured at the Tevatron.

The results of the precision electroweak fit are in good agreement with the experimental results, as shown in Fig. 28, and for example shows that there are 3 massless neutrinos which couple to the Z boson.

7.2.1 W mass measurements

One of the most important quantities in electroweak sector in the mass of the $W^{\pm}$ boson. The first measurements of the W mass were in hadronic collisions. The QCD backgrounds and resolution means that the hadronic $W^{\pm}$ decay mode cannot be used. The mass cannot be directly reconstructed using the leptonic mode due to the unobserved neutrino. Instead the transverse mass

$$M_{\perp}^{\ell\nu 2} = 2p_{\perp}^{\ell} \not{E}_{\perp} (1 - \cos\phi_{\ell,\mathrm{miss}}), \tag{76}$$

where $p_{\perp}^{\ell}$ is the transverse momentum of the observed lepton, $\not{E}_{\perp}$ is the missing transverse energy and $\phi_{\ell,\mathrm{miss}}$ is the azimuthal angle between the lepton and the direction of the missing transverse energy, is used.

The maximum value of the transverse mass is $M_{\perp}^{\ell\nu 2} \leq m_W^2$ and can be used to extract the $W^{\pm}$ mass. This approach was used by the UA1 and UA2 experiments for the original W mass measurements and the recent results at the Tevatron, for example Fig. 29. The endpoint is smeared by the non-zero $p_{\perp}$ and width of the W boson.

A major result of the LEP2 programme was the study of the production of pairs of electroweak gauge bosons, W^+W^- and Z^0Z^0. The mass of the W can be extracted in two ways:

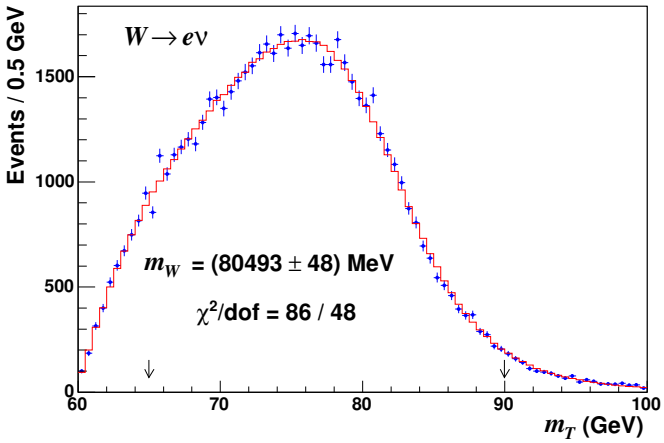

Figure 29: The transverse mass of the W at the Tevatron taken from Ref. [19].

1. measuring the cross section near the threshold

$$\sigma \sim \frac{G_F^2 m_W^2}{2\pi}\sqrt{1-\frac{4m_W^2}{s}}, \tag{77}$$

   which is clean theoretical but limited by statistics, see Fig. 30;

2. reconstructing the mass from the W decay products above threshold.

7.2.2 ρ parameter

In principle we should compare the full predictions of the Standard Model, or any model of new physics, with all the electroweak observables. However it is often useful, particularly in new physics models as corrections from new particles can lead to large corrections, to consider the ρ parameter. Naively

$$\rho = \frac{m_W^2}{m_Z^2 \cos^2\theta_W} = 1, \tag{78}$$

connects the Z^0 and $W^\pm$ masses with the weak mixing angle. The dominant loop corrections to it from self energies give

$$\Delta\rho = \frac{3G_F m_W^2}{8\sqrt{2}\pi^2}\left[\frac{m_t^2}{m_W^2} - \frac{\sin^2\theta_W}{\cos^2\theta_W}\left(\ln\frac{m_H^2}{m_W^2} - \frac{5}{6}\right) + \dots\right].$$

This relates m_W, m_t, and m_H. For a long time, m_t was most significant uncertainty in this relation; by now, m_W has more than caught up.

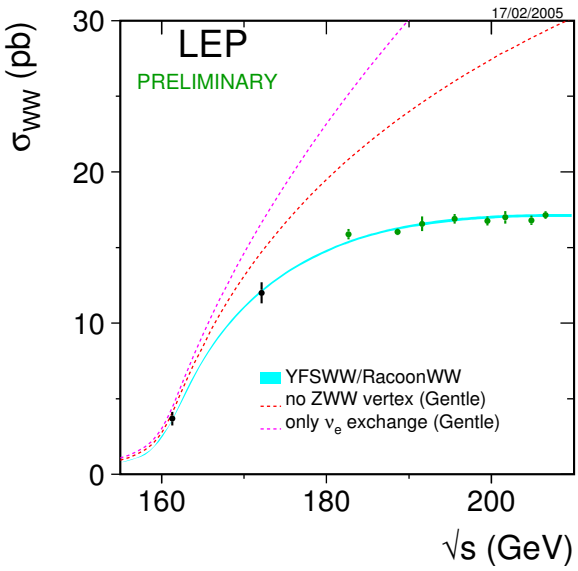

Figure 30: Cross section for the pair production of W^+W^- close to threshold from the LEPEWWG.

8 Higgs Boson

The details of the Higgs mechanism with the SM are covered in the Standard model course. In this section we summarise the properties of the Standard Model Higgs Boson that are important for hadron collider measurements.

The SM contains spin-1 gauge bosons and spin-$\frac{1}{2}$ fermions. Massless fields ensure gauge invariance under $SU(2)_L \times U(1)_Y$ and renormalizability. While we could introduce mass terms "by hand", *i.e.*

$$\mathcal{L} \propto m_A^2 A^\mu A_\mu + m_f(\bar{\Psi}_R \Psi_L + \bar{\Psi}_L \Psi_R), \tag{79}$$

this violates gauge invariance. Under the gauge transformation, $A^\mu \rightarrow A^\mu + \frac{1}{g}\partial^\mu\theta$, the mass term $A^\mu A_\mu$ gives terms proportional to the gauge transformation parameter θ, *i.e.* the gauge boson mass term is not gauge invariant. As the fields Ψ_L and Ψ_R transform differently under $SU(2)_L$ under the gauge transformation of the left-handed fermion field the fermion mass term is not gauge invariant.

Adding these mass terms by hand is obviously a bad idea. Instead we add a complex scalar doublet under the $SU(2)_L$ gauge group which introduces an additional four degrees of freedom. This scalar field can be coupled gauge invariantly to the gauge bosons, *i.e.*

$$\mathcal{L}_{\Phi A} = (D^\mu \Phi)(D_\mu \Phi). \tag{80}$$

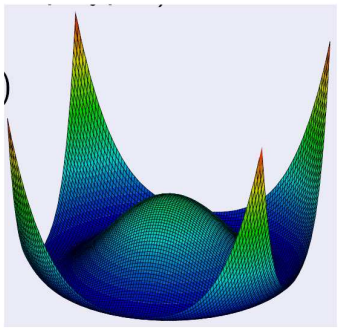

Figure 31: The Higgs boson potential.

A gauge-invariant interaction term with fermions can also be included[7]

$$\mathcal{L}_{\Phi\Psi} = g_f \bar{\Psi}_L \Phi \Psi_R + \text{h.c.}. \tag{81}$$

In addition we need the Higgs potential

$$\mathcal{V}(\Phi) = \lambda \left(\Phi^\dagger \Phi\right)^2 + \mu^2 \Phi^\dagger \Phi. \tag{82}$$

For $\mu^2 < 0$ this potential has an infinite number of equivalent minima,

$$|\Phi| = \sqrt{\frac{-\mu^2}{2\lambda}} \equiv \frac{v}{\sqrt{2}}, \tag{83}$$

as shown in Fig. 31. We expand around one of these minima giving one radial and three circular modes. The circular modes are "gauged away" $\longrightarrow$ "eaten" by gauge bosons to give them mass via the vacuum expectation value (vev) the minimum of the potential.

From the structure above:

$$\begin{array}{lcll} (D_\mu \Phi)^2 & \longrightarrow & \frac{g^2 v^2}{4} W_\mu W^\mu & \longrightarrow \quad M_W^2 = \frac{g^2 v^2}{4}; \\ g_f \bar{\Psi}_L \Phi \Psi_R & \longrightarrow & g_f \frac{v}{\sqrt{2}} \bar{\Psi}_L \Phi \Psi_R & \longrightarrow \quad m_f = \frac{g_f v}{\sqrt{2}}; \\ \lambda(|\Phi|^2 - v^2/2)^2 & \longrightarrow & \lambda v^2 H^2 & \longrightarrow \quad M_H^2 = 2\lambda v^2. \end{array}$$

This gives a fixed relation between the mass of the particles and their coupling to (surviving) scalar Higgs boson.

8.1 Unitarity

While in the Standard Model introducing the Higgs boson is the only way to give mass to the particles in a gauge invariant manner there are other arguments for the existence of the Higgs boson and it is interesting to ask what would happen if the Higgs boson did not exist.

[7] While we can use Φ to couple to the down-type fermions we need to use $i\sigma_2 \Phi^*$ to couple to the up-type fermions in a gauge invariant manner.

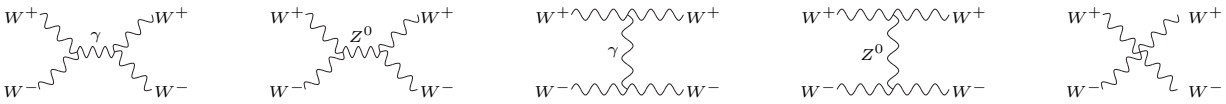

Figure 32: Feynman diagrams for WW scattering via gauge boson exchange.

If we consider $W^+W^- \to W^+W^-$ scattering, via the Feynman diagrams shown in Fig. 32, in the high energy limit the matrix element is

$$\mathcal{M} = g^2 \frac{s}{8M_W^2} \left(1 - \frac{4M_W^2}{s}\right)(1 + \cos\theta). \tag{84}$$

So without the Higgs boson the cross section

$$\sigma \sim \frac{s}{M_W^4}, \tag{85}$$

for $s \gg M_W$.

Figure 33: Higgs boson contributions to WW scattering.

This violates unitarity, so we need something to cancel the bad high energy behaviour of the cross section. We can arbitrarily invert a particle to cure this. This particle must be a scalar, suppose it has coupling, λ, to W^+W^-. This gives a contribution, via the Feynman diagrams in Fig. 33,

$$\mathcal{M} = \lambda^2 \left[-\frac{s}{8M_W^4}(1 + \cos\theta) - \frac{M_H^2}{4M_W^4} \left\{ \frac{s}{s - M_H^2} + \frac{t}{t - M_H^2} \right\} \right]. \tag{86}$$

This cancels the bad high energy behaviour if $\lambda = gM_W$, *i.e.* the Higgs coupling to the $W^\pm$ boson. If we repeat the same procedure for $WW \to ZZ$ we need a coupling $g_{ZZH} \propto gm_Z$ and for $WW \to f\bar{f}$ we need a coupling $g_{f\bar{f}H} \propto gm_f$, *i.e.* the Higgs boson couplings to the Z^0 boson and Standard Model fermions.

So even if there was no Higgs boson we are forced to introduce a scalar interaction that couples to all particles proportional to their mass.

8.2 Higgs Measurements

To study the properties of the recently discovered Higgs boson we should focus our attention on,

- channels with a high signal rate;
- and a low background rate.

Decay mode	Partial Width, Γ
$H \to f\bar{f}$	$\frac{G_F M_H}{8\pi\sqrt{2}} \cdot 2m_f^2 N_c \left(1 - \frac{4m_f^2}{m_H^2}\right)^{\frac{3}{2}}$
$H \to W^+W^-$	$\frac{G_F M_H}{8\pi\sqrt{2}} \cdot m_H^2 \left(1 - \frac{4m_W^2}{m_H^2} + \frac{12m_W^4}{m_H^4}\right)\left(1 - \frac{4m_W^2}{m_H^2}\right)^{\frac{1}{2}}$
$H \to ZZ$	$\frac{G_F M_H}{8\pi\sqrt{2}} \cdot m_H^2 \frac{m_W^2}{2m_Z^2} \left(1 - \frac{4m_Z^2}{m_H^2} + \frac{12m_Z^4}{m_H^4}\right)\left(1 - \frac{4m_Z^2}{m_H^2}\right)^{\frac{1}{2}}$
$H \to \gamma\gamma$	$\frac{G_F M_H}{8\pi\sqrt{2}} \cdot m_H^2 \left(\frac{\alpha}{4\pi}\right)^2 \cdot \left(\frac{4}{3} N_c Q_t^2\right)^2 \qquad (2m_t > m_H)$
$H \to gg$	$\frac{G_F M_H}{8\pi\sqrt{2}} \cdot m_H^2 \left(\frac{\alpha_s}{4\pi}\right)^2 \cdot \left(\frac{2}{3}\right)^2 \qquad (2m_t > m_H)$
$H \to VV^*$	more complicated, but important for $m_H \lesssim 2m_V$

Table 4: Partial widths for various Higgs decay modes.

Unfortunately the channels with the highest signal rate often have the largest backgrounds. We need to be able to trigger on a given signal. Good mass resolution for the mass of the Higgs boson and its decay products can help to suppress backgrounds. We should also try and measure things that are well understood theoretically.

In order to consider the signals we need to understand how the Higgs boson is produced and then decays in hadron–hadron collisions.

The analytic results for the partial widths for various Higgs boson decay modes are given in Table 4 and the branching ratios are plotted as a function of the mass of the Higgs boson in Fig. 34. For $m_H < 2m_W$ the Higgs boson is quite narrow, $\Gamma_H = \mathcal{O}(\text{MeV})$, while for $m_H > 2m_W$ the Higgs boson becomes obese, $\Gamma_H(m_H = 1\text{TeV}) \approx 0.5$ TeV. At large m_H the decay into vector boson pairs, W^+W^- and Z^0Z^0, is dominant with $\Gamma_{H\to WW} : \Gamma_{H\to ZZ} \approx 2 : 1$, while for small m_H the decay into bottom quark pairs is dominant,

As the Higgs boson likes to couple to heavy objects (top, W, Z) there are a range of important Higgs production processes where the Higgs boson couples to heavy particles. The Feynman diagrams for the important processes are shown in Fig. 35 while the cross sections for the important processes are shown in Fig. 36 as a function of the Higgs boson mass.

The relative importantance of different channels depend on the collider energy and the initial state (e.g. pp or $p\bar{p}$). At the Tevatron typical channels used for searches were:

- $gg \to H \to W^+W^- \to \ell\ell' + \not{E}_\perp$ this was the "golden plated" channel because although there is no mass peak the background can be reduced by using quantities, such as the angle between the leptons, which differ in the signal and background due to the different W boson production mechanisms;

- $q\bar{q} \to ZH \to \ell\ell b\bar{b}$ the key ingredient for this process is the b-tagging efficiency and mass resolution for jets in order to suppress the QCD backgrounds;

- $q\bar{q}' \to WH \to \ell\nu b\bar{b}$ has similar features to $q\bar{q} \to ZH \to \ell\ell b\bar{b}$;

- $q\bar{q}' \to ZH \to \not{E}_\perp + b\bar{b}$ the key feature is again the b-tagging efficiency and mass resolution for jets in order to suppress the QCD backgrounds;

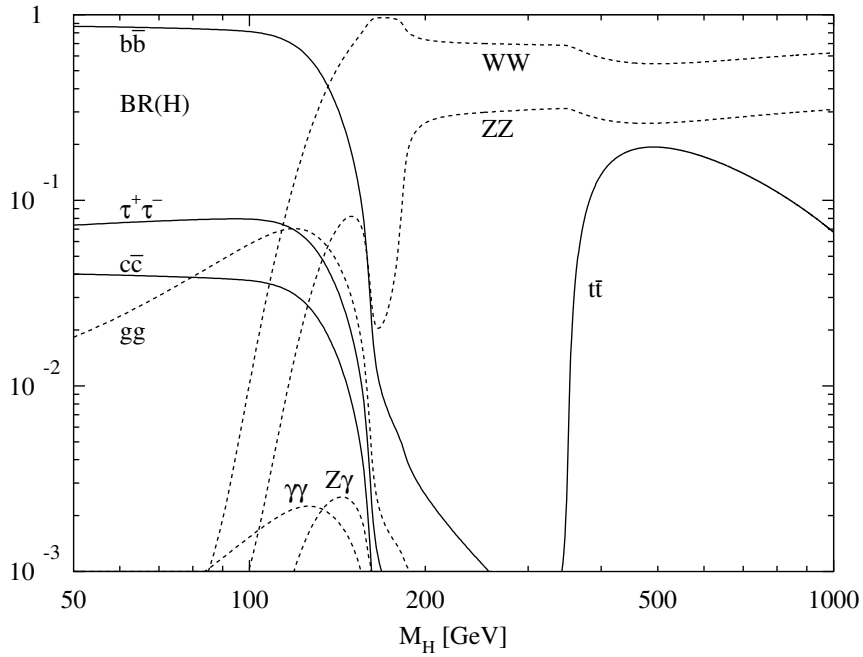

Figure 34: Branching ratios for the Higgs boson as a function of the Higgs boson mass, taken from Ref. [20], calculation by M. Spira.

- $q\bar{q}' \to W^{\pm}H \to W^{\pm}W^{+}W^{-}$ in this case there is the possibility of same sign lepton production which has a low background together with the decay of remaining W to hadrons in order to increase the cross section.

Typical channels at the LHC include:

- $gg \to H \to ZZ \to 4\mu, 2e2\mu$ which is the "Golden plated" channel for $m_H > 140$ GeV, the key ingredient is the excellent resolution of the Z mass peak from the leptonic decay;

- $gg \to H \to W^{+}W^{-} \to \ell\ell' + \not{E}_{\perp}$ is similar to the Tevatron analysis but with better statistics due to the larger production cross section;

- $gg \to H \to \gamma\gamma$ since Nature determined that the Higgs boson should have a mass around 120 GeV this is the easiest way to detect a Higgs boson in a collider exper iemnt. Although the branching ratio is small, the key ingredient is the mass resolution for photon pairs and a veto on photons from π^0 decays;

- VBF$\to H \to \tau\tau$ an important mode for determining couplings to the EW sector of the SM. The key ingredient is that QCD backgrounds are reduced by requiring a rapidity gap between the two tagging jets;

- VBF$\to H \to WW$ as for VBF$\to H \to \tau\tau$;

- VBF$\to H \to b\bar{b}$ is in principle similar to the other VBF modes but it is hard to trigger on pure QCD-like objects (jets).

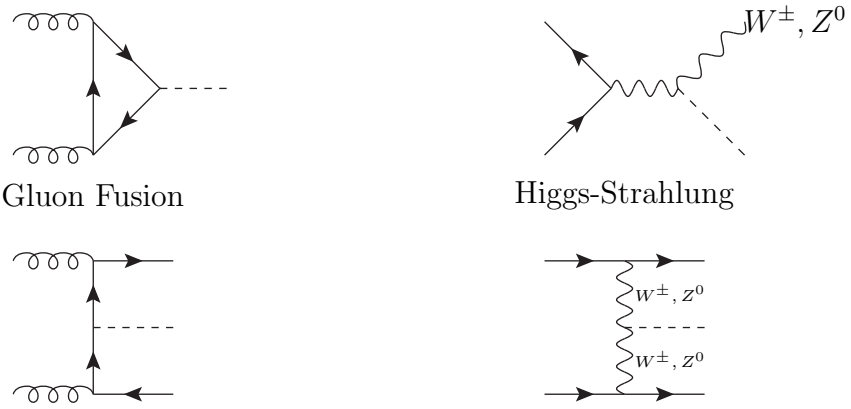

Figure 35: Feynman diagrams for important Higgs boson production processes.

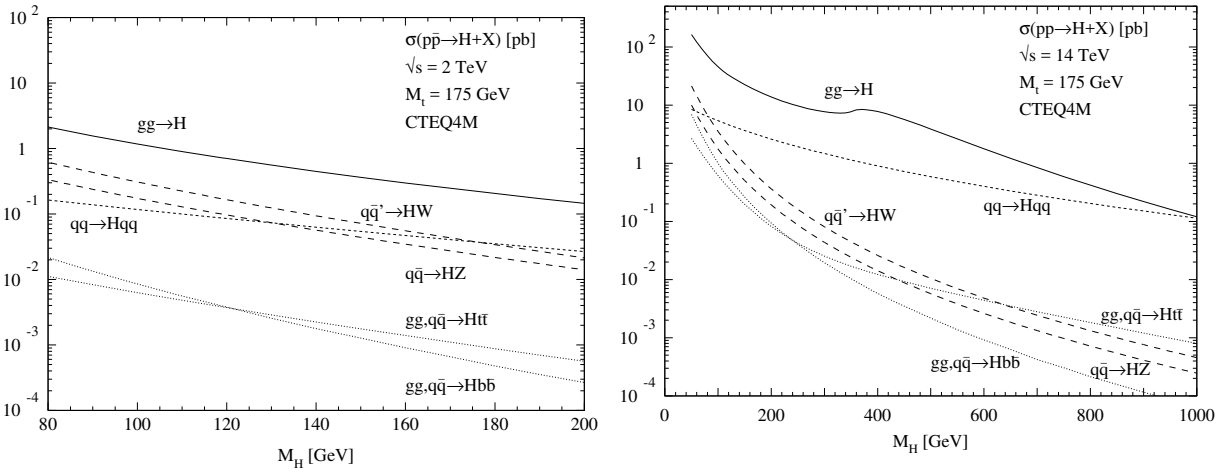

Figure 36: Higgs production cross sections at hadron colliders taken from Ref. [20], calculation by M. Spira.

8.3 The effective Higgs coupling to gluons

The loop induced coupling of gluons to the Higgs boson via a massive quark loop is one of the most important ingredients for Higgs studies at a proton-proton collider. Quantum corrections to this process can be extremely large but computations with the full dependence on the quark mass are extremely difficult.

For low transverse momenta, and inclusive quantities like the total cross section, it is popular to compute the quantum corrections in an effective field theory in the limit that the top quark mass is infinitely heavy, $m_t \to \infty$. The Lagrangian of the heavy quark Higgs effective theory (HEFT) proceeds through a dimension-five operator with the Higgs coupling directly to gluons and is derived via expansion in m_H/m_t,

$$\mathcal{L}_{\text{HEFT}} = c_{\text{HEFT}} \frac{1}{4} H G^{a,\mu\nu} G^a_{\mu\nu} \tag{87}$$

where $c_{\text{HEFT}} = \frac{\alpha_s}{3\pi v} + \mathcal{O}(\alpha_s^2)$ for a Higgs vacuum expectation value v. It is possible to

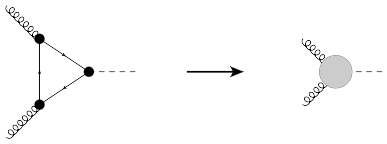

Figure 37: The triangle Feynamn diagram for $gg \to H$ via a haevy quark loop can be used to extract the Wilson coefficient in the heavy quark effective Higgs Lagrangian.

extract the value of c_{HEFT} by considering to large mass limit of the triangle diagram in Figure 37. While the ratio of m_H/m_t is not particularly small the approximation often does a good job at matching data when the complete results for leading order are used as a normalisation. As the transverse momentum of the produced Higgs boson increases the approximation will break down.

Computations within this effective theory are now available for the total cross section $gg \to H$ through to N^{3}LO [21, 22]. Figure 38 shows the convergence of the total cross-section by studying the dependence on the renormalisation and factorisation scale $\mu = \mu_R = \mu_F$. Futher details on the approximation and other topics can be found in references [5, 23].

8.4 Extended Higgs Sectors

While current measurements show no significant deviations from a minimal SM Higgs sector adding a single Higgs doublet is the simplest choice for the Higgs sector. Many theoretically attractive models like SUSY naturally have a larger Higgs sector. However, we need to be careful to respect constraints from flavour changing neutral currents (FCNC) and the electroweak precision data.

8.4.1 The Two Higgs Doublet Model

The simplest extension to the Standard Model is the *Two Higgs Doublet Model* (THDM). In this model there are two Higgs doublets. There are a number of variants on the model depending on whether or not CP is conserved and how the Higgs bosons couple

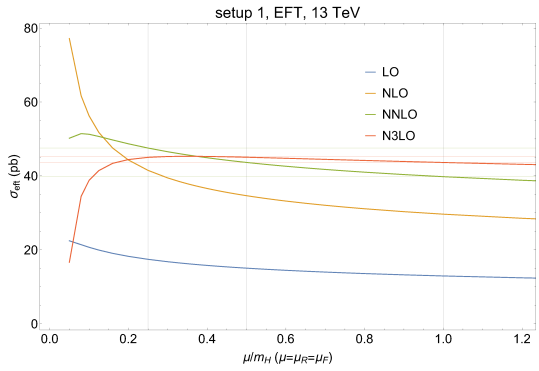

Figure 38: The scale dependence of the total cross section for Higgs production through gluon fusion up to N^{3}LO in QCD. Figure taken from Ref. [22].

to the fermions. The most interesting variant (called Type-II) is that which occurs (in a constrained variant) in SUSY models. In the general version of the Type-II model there are ~ 10 new parameters, whereas in the constrained SUSY version there are only two m_{A^0} and $\tan\beta$. There are indirect constraints from rare processes, *e.g.* kaon and bottom mixing and decays, precision EW data and cosmology.

As there are two doublets there as two vevs: $v_{1,2}$. They are constrained by the requirement

$$v_1^2 + v_2^2 = v^2 \approx (246\text{GeV})^2, \tag{88}$$

in order to give the correct gauge boson masses as in the Standard Model. There is an additional parameter $\tan\beta = v_2/v_1$. In the Type-II mode the H_1 doublet gives mass to up-type fermions while the H_2 doublet gives mass to down-type fermions. Both doublets couple and give mass to the gauge bosons. After electroweak symmetry breaking there are five scalar boson mass eigenstates, two neutral scalars h^0, H^0, one neutral pseudoscalar A^0, and two charged scalars $H^\pm$. The coupling of all the Higgs bosons to the vector bosons are reduced. The couplings to the fermions are enhanced (up-type) and suppressed (down-type) as $\tan\beta$ increases. At tree level the masses are related by

$$m_{H^\pm}^2 = m_{A^0}^2 + m_W^2, \qquad\qquad m_{H^0}^2 + m_{h^0}^2 = m_{A_0}^2 + m_Z^2. \tag{89}$$

At tree level in SUSY $m_{h^0} \leq M_Z$ however there are large quantum corrections ($m_{h^0} \lesssim 140\,\text{GeV}$).

9 Beyond the Standard Model Physics

As discussed in Section 7 the Standard Model has 18 free parameters, although in principle we should also include the Θ parameter of QCD. We now need more parameters to incorporate neutrino masses. Despite the excellent description of all current experimental data there are still a number of important questions the Standard Model does not answer.

- What are the values of these parameters?
- Why is the top quark so much heavier that the electron?
- Why is the Θ parameter so small?
- Is there enough CP-violation to explain why we are here, *i.e.* the matter-antimatter asymmetry of the universe?
- What about gravity?

While these are all important questions there is no definite answer to any of them.

There are however a large number of models of Beyond the Standard Model (BSM) physics which motivated by trying to address problems in the Standard Model. Given the lack of any experimental evidence of BSM physics the field is driven by theoretical and ascetic arguments, and unfortunately fashion.

All models of BSM physics predict either new particles or differences from the Standard Model, otherwise they cannot be distinguished experimentally from the Standard Model. There are a number of ways of looking for BSM effects:

Collider Experiments if the theory contains new particles these should be produced in collider experiments and decay to give Standard Model particles, currently the searches at the energy frontier are at the LHC general-purpose detectors ATLAS and CMS;

Precision Experiments measure something predicted by the Standard Model to very high accuracy and compare the results with the theoretical prediction, examples include the LEP/SLD precision measurements at the Z^0 pole and the anomalous magnetic moment, $g-2$, of the muon;

Rare Decays or Processes measure the cross section or decay rate for some process which the Standard Model predicts to be small (or zero). Examples include: neutron electric dipole moment experiments, proton decay experiments, neutrino mixing experiments, rare B and kaon decay and CP-violation experiments (BELLE, BaBar, NA48/62, LHCB).

In many ways these approaches are complimentary. Some effects, *e.g* CP-violation, are best studied by dedicated experiments but if the result of these experiments differs from the SM there should be new particles which are observable at collider experiments.

We will consider the collider signals of BSM physics in detail but only look at the constraints from low-energy physics as we look at various models. The most important low energy constraints are flavour changing neutral currents and proton decay. Often other constraints, *e.g.* from astrophysics and cosmology are also considered.

9.1 Models

We will briefly review some of the more promising models and then look at the implications of these models for collider physics taking a pragmatic view looking at the different possible signatures rather than the details of specific models.

There are a wide range of models: grand unified theories; Technicolor; supersymmetry; large extra dimensions; small extra dimensions; little Higgs models; unparticles .... Depending on which model builder you talk to they may be almost fanatical in their belief that one of these models is realized in nature.

9.1.1 Grand Unified Theories

The first attempts to answer the problems in the Standard Model were *Grand Unified Theories* (GUTs.) The basic idea is that the Standard Model gauge group $SU(3)_c \times SU(2)_L \times U(1)_Y$ is the subgroup of some larger gauge symmetry. The simplest group is SU(5), which we will consider here, other examples include SO(10). SU(5) has $5^2-1=24$ generators which means there are 24 gauge bosons. In the Standard Model there are 8 gluons and 4 electroweak gauge bosons ($W^\pm,\ W^0,\ B^0 \Rightarrow W^\pm,\ \gamma,\ Z^0$). Therefore there are 12 new gauge bosons $X^{\pm\frac{4}{3}}$ and $Y^{\pm\frac{1}{3}}$. The right-handed down type quarks and left

handed leptons form a $\bar{5}$ representation of $SU(5)$. The rest of the particles form a 10 representation of the gauge group

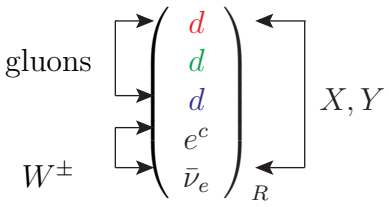

$$\begin{pmatrix} 0 & u^c & -u^c & -u & -d \\ u^c & 0 & u^c & -u & -d \\ u^c & -u^c & 0 & -u & -d \\ u & u & u & 0 & -e^c \\ d & d & d & e^c & 0 \end{pmatrix}_L . \quad (90)$$

In this model there are two stages of symmetry breaking. At the GUT scale the $SU(5)$ symmetry is broken and the X and Y bosons get masses. At the electroweak scale the $SU(2) \times U(1)$ symmetry is broken as before. There are three problems with this theory: the couplings do not unify at the GUT scale; why is the GUT scale higher than the electroweak scale; and proton Decay. We will come back to the first two of these questions.

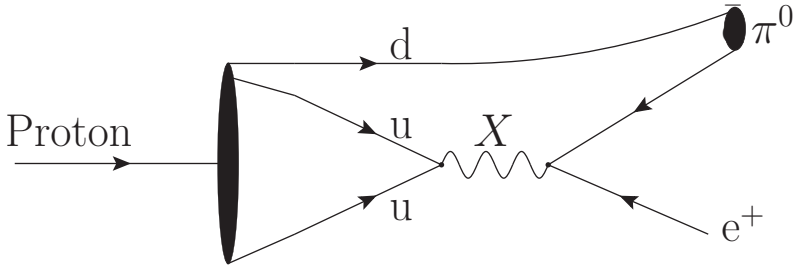

Figure 39: Proton Decay in a Grand Unified theory.

Proton Decay Grand unified theories predict the decay of the proton via the exchange of the X and Y bosons, as shown in Fig. 39. We would expect this decay rate to go like

$$\Gamma(p \to \pi^0 e^+) \sim \frac{M_p^5}{M_X^4}, \quad (91)$$

where M_X is the mass of the X boson and M_p the mass of the proton, on dimensional grounds.

There are limits on the proton lifetime from water Čerenkov experiments. The decay of the proton will produce an electron which is travelling faster than the speed of light in water. This will give Čerenkov radiation, just as the electron produced in the weak interaction of a neutrino does. This is used to search for proton decay. As there is no evidence of proton decay there is limit of

$$\tau_P \geq 1.6 \times 10^{32} \text{ years} \quad (92)$$

on the proton lifetime. This means $M_X > 10^{16-17}$GeV which is larger than preferred by coupling unification. Proton decay gives important limits on other models.

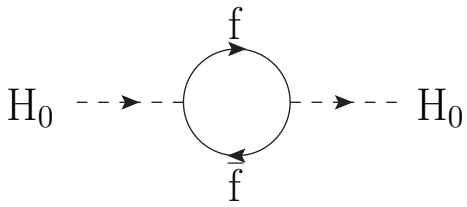

Figure 40: Quantum correction to the Higgs mass from a fermion loop.

9.1.2 Hierarchy Problem

The vast majority of new physics models are motivated by considering the hierarchy problem, *i.e.* why is the electroweak scale is so much less than the GUT or Planck (where gravity becomes strong) scales? It is more common to discuss the technical hierarchy problem which is related to the Higgs boson mass. If we look at the Higgs mass there are quantum corrections from fermion loops such as that shown in Fig. 40. This gives a correction to the Higgs mass,

$$\delta M_{Hf}^2 = i\frac{|g_f|^2}{4}\int \frac{d^4k}{(2\pi)^4}\frac{\text{tr}\left[(\not{k}+\not{p}+m_f)(\not{k}+m_f)\right]}{\left[(k+p)^2-m_f^2\right]\left[k^2-m_f^2\right]}, \tag{93}$$

where p is the four-momentum of the Higgs boson, k the four-momentum flowing in the loop, g_f the coupling of the Higgs boson to the fermion and m_f the fermion mass. We need to introduce an ultra-violet cut-off, Λ, to regularize the integral giving

$$\delta M_{Hf}^2 = \frac{|g_f|^2}{16\pi^2}\left[-2\Lambda^2+6m_f^2\ln\left(\Lambda/m_f\right)\right]. \tag{94}$$

So either the Higgs mass is the GUT/Planck scale or there is a cancellation

$$M_H^2 = M_{H\,\text{bare}}^2 + \delta M_H^2, \tag{95}$$

of over 30 orders of magnitude to have a light Higgs boson.

This worries a lot of BSM theorists, however there are values of the Higgs boson mass for which the Standard Model could be correct up to the Planck scale. The Higgs boson mass is $m_H^2 = \lambda v^2$. There are two constraints on the mass: the coupling should be perturbative, $\lambda \lesssim 1$; the vacuum must be non-trivial, $\lambda \to 0$ is forbidden. As can be seen in Fig. 41 there is an island of stability in the middle where the Standard Model can be valid to the Planck scale.

Many solutions to the hierarchy problem have been proposed. They come in and out of fashion and occasionally new ones are proposed. Examples include: Technicolor; supersymmetry; extra dimensions; and little Higgs models.

9.1.3 Technicolor

Technicolor is one of the oldest solutions to the hierarchy problem. The main idea is that as the problems in the theory come from having a fundamental scalar particle they can be solved by not having one. The model postulates a new set of gauge interactions *Technicolor*, which acts on new technifermions. We think of this interaction like QCD,

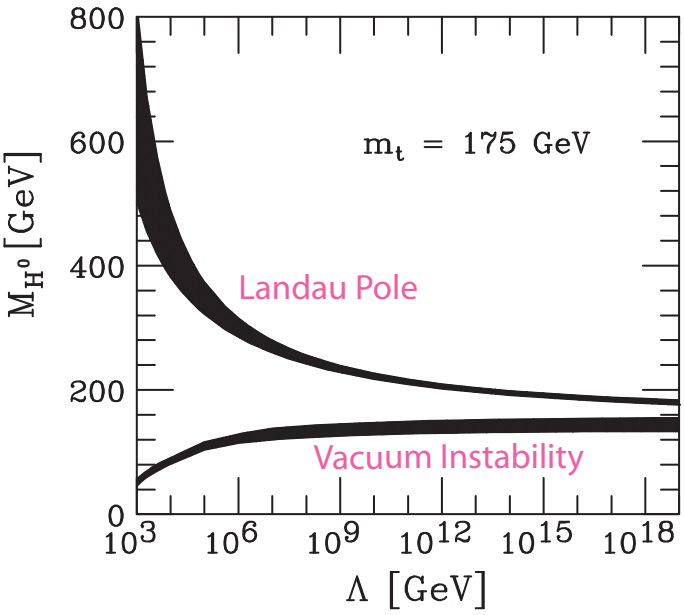

Figure 41: Region of stability for the Standard Model Higgs boson.

although different gauge groups have been considered. The technifermions form bound states, the lightest being technipions. Using the Higgs mechanism these technipions give the longitudinal components of the $W^{\pm}$ and Z bosons, and hence generate the gauge boson masses. There must also be a way to generate the fermions masses, *Extended Technicolor*. It has proved hard to construct realistic models which are not already ruled out. For many years Technicolor fell out of fashion, however following the introduction of little Higgs models there has been a resurgence of interest and the new walking Technicolor models look more promising.

9.1.4 Supersymmetry

If there is a scalar loop in the Higgs propagator, as shown in Fig. 42. We get a new

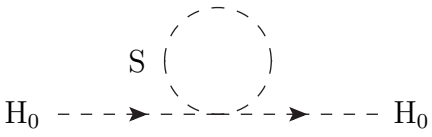

Figure 42: New scalar boson loop in the Higgs boson propagator.

contribution to the Higgs mass,

$$\delta M_{HS}^2 = \frac{\lambda_s}{16\pi^2}\left(\Lambda^2 - 2M_S^2 \ln\left(\Lambda/M_S\right)\right), \tag{96}$$

where M_S is the mass of the new scalar particle. If there are two scalars for every fermion, with the same mass and $\lambda_s = |g_f|^2$ the quadratic dependence cancels. Theorists like to

SM particle	Spin	SUSY particle	Spin
Electron	1/2	Selectron	0
Neutrino	1/2	Sneutrino	0
Up	1/2	Sup	0
Down	1/2	Sdown	0
Gluon	1	Gluino	1/2
Photon	1	Photino	1/2
Z	1	Zino	1/2 Neutralinos
Higgs	0	Higgsino	1/2
W^+	1	Wino	1/2 Charginos
H^+	0	Higgsino	1/2

Table 5: Particle content of the Minimal Supersymmetric Standard Model.

have symmetries to explain cancellations like this, *Supersymmetry* (SUSY). For every fermionic degree of freedom there is a corresponding bosonic degree of freedom: all the SM fermions have two spin-0 partners; all the SM gauge bosons have a spin-$\frac{1}{2}$ partner. The full particle content of the theory is given in Table 5. In SUSY models we need to have two Higgs doublets to give mass to both the up- and down-type quarks in a way which is invariant under the supersymmetric transformations.

There are major two reasons, in addition to the solution of the hierarchy problem, to favour SUSY as an extension of the SM.

Coleman-Mandula theorem If we consider any extension to the Poincaré group any new generators which transform as bosons lead to a trivial S-matrix, *i.e.* scattering only through discrete angles. Later Haag, Lopuszanski and Sohnius showed that SUSY is the only possible extension of the Poincaré group which doesn't give a trivial S-matrix.

SUSY coupling unification In SUSY GUTS the additional SUSY particles change the running of the couplings and allow the couplings to truly unify at the GUT scale, as shown in Fig. 43. However, with increasingly accurate experimental measurements of the strong coupling this is no longer quite true.

In the modern view of particle physics we construct a theory by specifying the particle content and symmetries. All the terms allowed by the symmetries are then included in the Lagrangian. If we do this in supersymmetric models we naturally get terms which do not conserve lepton and baryon number. This leads to proton decay as shown in Fig. 44. Proton decay requires that both lepton and baryon number conservation are violated. The limits on the proton lifetime lead to very stringent limits on the product of the couplings leading to proton decay.

$$\lambda'_{11k} \cdot \lambda''_{11k} \lesssim 2 \cdot 10^{-27}. \tag{97}$$

Only natural way for this to happen is if some symmetry requires that one or both couplings are zero. Normally a multiplicatively conserved symmetry *R-parity*

$$R_p = (-1)^{3B+L+2S}, \tag{98}$$

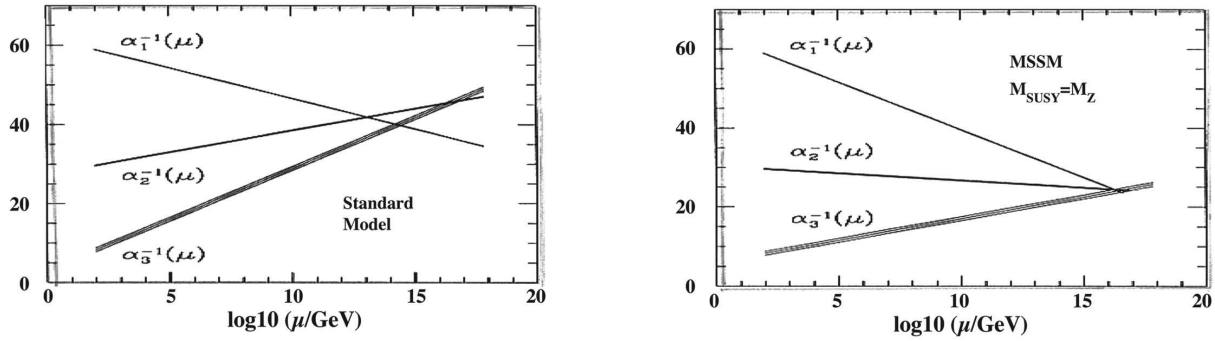

Figure 43: Coupling constant unification in the Standard and Minimal Supersymmetric Standard Models.

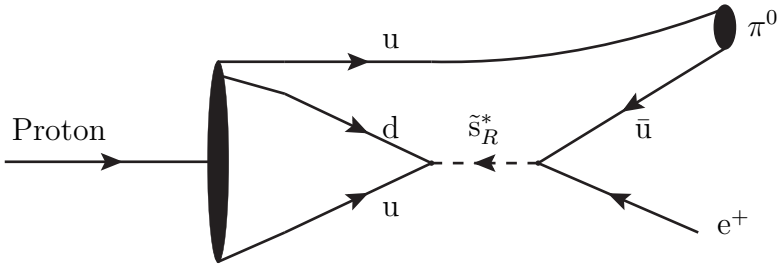

Figure 44: Proton decay in supersymmetric models.

such that Standard Model Particles have $R_p = +1$ and SUSY particles have $R_p = -1$, is introduced which forbids both terms.

Alternatively symmetries can be imposed which only forbid the lepton or baryon number violating terms. The simplest SUSY extension of the Standard Model has R_p conservation and is called the Minimal Supersymmetric Standard Model (MSSM). The multiplicative conservation of R-parity has two important consequences: SUSY particles are only pair produced; the lightest SUSY particle is stable, and therefore must be neutral on cosmological grounds. It is therefore a good dark matter candidate.

So far we haven't dealt with the biggest problem in SUSY. Supersymmetry requires that the SUSY particles have the same mass as their Standard Model partner and the SUSY partners have not been observed. SUSY must therefore be a broken symmetry in such a way that the Higgs mass does not depend quadratically on the ultraviolet cut-off, called *soft SUSY breaking*. This introduces over 120 parameters into the model. Many of these parameters involve either flavour changing or CP-violating couplings and are constrained by limits on flavour changing neutral currents.

Flavour Changing Neutral Currents In the Standard Model the only interactions which change change the quark flavour are those with the $W^{\pm}$ boson. So any processes which change the flavour of the quarks, but not the charge, *Flavour Changing Neutral Currents* (FCNCs), must be loop mediated.

There are two important types: those which change the quark flavour with the emission of a photon, *i.e.* $b \to s\gamma$; those which give meson-antimeson mixing, *e.g.* $B - \bar{B}$ mixing.

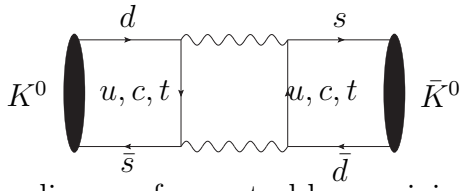

Figure 45: Feynman diagram for neutral kaon mixing in the Standard Model.

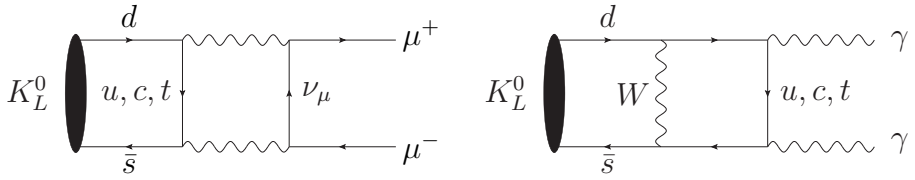

Figure 46: Feynman diagrams for the decay of the neutral kaon to $\mu^+\mu^-$ and $\gamma\gamma$ in the Standard Model.

Both are important in the Standard Model and in constraining possible new physics models.

In the Standard Model flavour changing neutral currents are suppressed by the Glashow-Iliopoulos-Maiani (GIM) mechanism. If we consider neutral Kaon mixing, as shown in Fig. 45, and the rare Kaon decays $K_L^0 \to \mu^+\mu^-$ and $K_L^0 \to \gamma\gamma$, as shown in Fig. 46.

Considering only two generations for simplicity all these diagrams go like

$$\frac{1}{M_W^2}\frac{m_u^2 - m_c^2}{M^2}, \tag{99}$$

times a factor due to the Cabibbo mixing angle where M is the largest mass left after the removal of one W propagator, *i.e.* M_W for $K^0 - \bar{K}^0$ mixing and $K_L^0 \to \mu^+\mu^-$, and m_c for $K_L^0 \to \gamma\gamma$. This suppression is called the GIM mechanism and explains why $\Gamma(K_L^0 \to \mu^+\mu^-) \sim 2 \times 10^{-5}\Gamma(K_L^0 \to \gamma\gamma)$. The current experimental results are in good agreement with the SM. This often proves a problem in BSM physics as there are often new sources of FCNCs.

In SUSY theories the SUSY partners also give contributions to FCNCs, as shown in Fig. 47. In this case the diagrams proportional to the mass difference of the squarks.

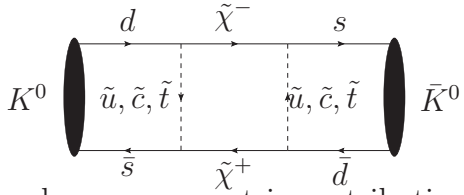

Figure 47: An example supersymmetric contribution to neutral kaon mixing.

Provide the SUSY breaking masses are flavour independent this is not a problem, as the mass differences are the same as the SM. It is also not a problem if there is no flavour mixing in the model. In general both these things are possible and must be considered.

SUSY Breaking What are the 120 SUSY breaking parameters? In general there are: SUSY breaking masses for the scalars; SUSY breaking masses for the gauginos; A terms which mix three scalars; mixing angles and CP-violating phases. We need a model of

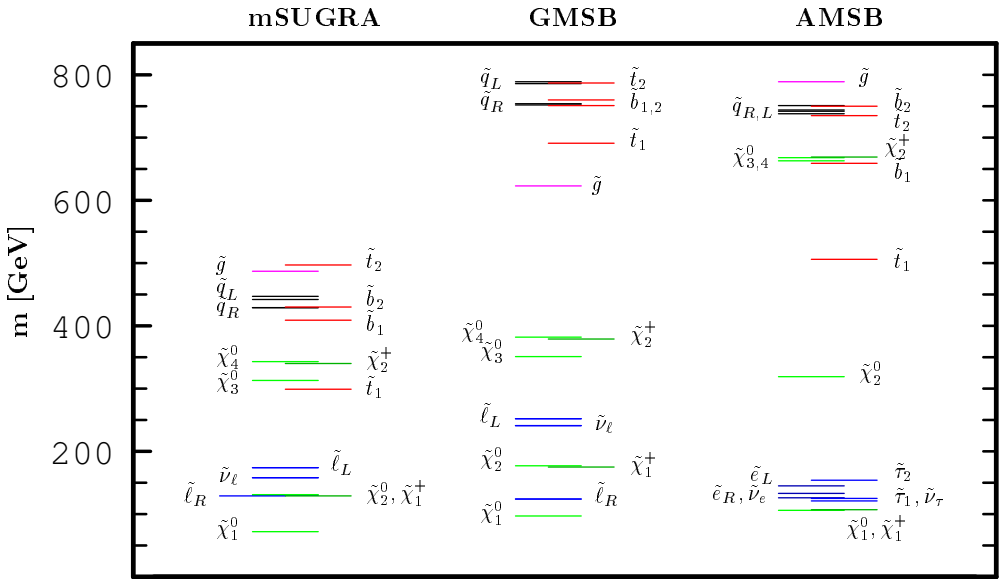

Figure 48: Examples of the mass spectra in different SUSY breaking models.

where these parameters come from in order to do any phenomenological or experimental studies. We therefore use models which predict these parameters from physics at higher energy scales, *i.e.* the GUT or Planck scale. In all these models SUSY is broken in a hidden sector. The models differ in how this SUSY breaking is transmitted to the visible sector, *i.e.* the MSSM particles.

SUGRA SUSY breaking is transmitted via gravity. All the scalar (M_0) and gaugino ($M_{1/2}$) masses are unified at the GUT scale. The A and B terms are also universal. The known value of M_Z is used to constrain the μ and B parameters leaving $\tan\beta = v_1/v_2$ as a free parameter. There are five parameters which give the mass spectrum: M_0, $M_{1/2}$, $\tan\beta$, $\mathrm{sgn}\,\mu$, A. The gluino mass is correlated with $M_{1/2}$ and slepton mass with M_0.

GMSB In gauge mediated SUSY breaking (GMSB) the flavour-changing neutral current problem is solved by using gauge fields instead to gravity to transmit the SUSY breaking. The messenger particles, X, transmit the SUSY breaking. The simplest choice is a complete $SU(5)$ **5** or **10** of particles transmitting the SUSY breaking to preserve the GUT symmetry. The fundamental SUSY breaking scale $\lesssim 10^{10}\,\mathrm{GeV}$ is lower than in gravity mediated models. The gaugino masses occur at one-loop, $M_{\tilde{g}} \sim \alpha_s N_X \Lambda$ while the scalar masses occur at two-loop, $M_{\tilde{q}} \sim \alpha_s^2 \sqrt{N_X}\Lambda$, where Λ is the breaking scale and N_X the number of messenger fields. The true LSP is the almost massless gravitino. The lightest superpartner is unstable and decays to gravitino and can be neutral, *e.g.* $\tilde{\chi}_1^0$, or charged, *e.g.* $\tilde{\tau}_1$.

AMSB The superconformal anomaly is always present and can give anomaly mediated SUSY breaking (AMSB). This predicts the sparticle masses in terms of the gravitino mass, $M_{3/2}$. The simplest version of the model predicts tachyonic particles so another SUSY breaking mechanism is required to get a realistic spectrum, *e.g.* adding universal scalar masses (M_0). The model has four parameters M_0, $M_{3/2}$, $\tan\beta$ and $\mathrm{sgn}\,\mu$. In this model the lightest chargino is almost degenerate with the lightest neutralino.

The mass spectrum in the models is different, as shown in Fig. 48. The main differences are: the mass splitting between gluino and electroweak gauginos; the mass splitting of the squarks and sleptons; and the nature of the LSP.

Muon g-2 Another important low energy constraint on BSM physics is the anomalous magnetic moment of the muon. The magnetic moment of any fundamental fermion is

$$\mu = g\left(\frac{e}{2m}\right)\mathbf{S}, \tag{100}$$

where g is the g-factor, m the mass and $\mathbf{S}$ the spin of the particle. The Dirac equation predicts $g = 2$. However there are quantum corrections, as shown in Fig. 49, which lead to an anomalous magnetic moment, $g - 2$.

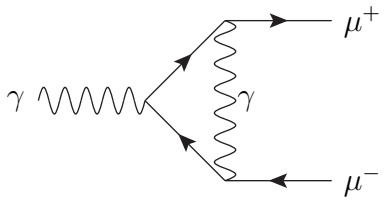

Figure 49: Vertex correction contributing to the anomalous muon magnetic moment in the Standard Model.

There are also quark loops in the photon propagator, as shown in Fig. 50. This is a low energy process so we can not use perturbative QCD. Instead we must use the measured e^+e^- total cross section and the optical theorem to obtain the corrections which leads to an experimental error on the theoretical prediction. In many BSM theories, for example

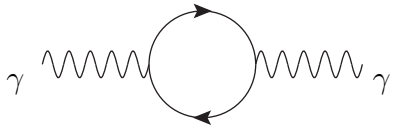

Figure 50: Quark loop in the photon propagator which contributes to the anomalous muon magnetic moment in the Standard Model.

in SUSY, there are additional corrections from diagrams, such as that shown in Fig. 51.

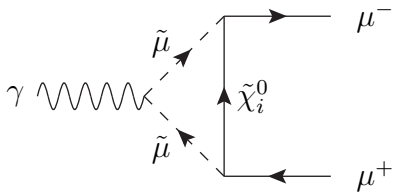

Figure 51: Example of a SUSY correction to the muon magnetic moment.

The original experimental result disagreed with the SM at 2.6σ, but there was an error in the sign in one of the terms in the theoretical calculation reducing the significance to about 1.4σ. However if you measure enough quantities some of them should disagree with the prediction by more the 1 sigma (about 1/3), and some by 2 sigma (4.6%) or 3 sigma (0.3%). This is why we define a discovery to be 5 sigma (6×10^{-5}%), so this is nothing to worry about.

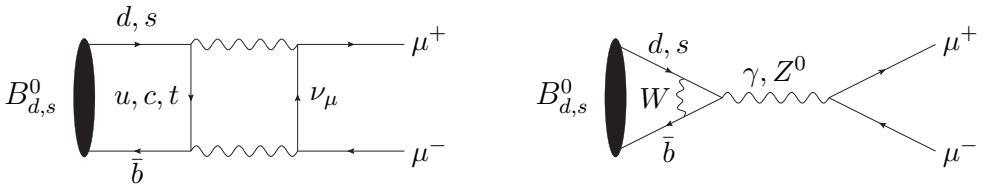

Figure 52: Standard Model Feynman diagrams for $B_s \to \mu^+\mu^-$.

Rare B decays There is an amazing consistency of the current flavour physics measurements. However, many new physics models can have a similar pattern in their flavour sector, the new physics model must have this otherwise it is experimentally excluded. However, there can still be new physics in rare processes (like $B^+ \to \tau^+\nu_\tau$) and CP-asymmetries. One promising examples is the decay $B_s \to \mu^+\mu^-$. There are two Standard Model contributions from box and penguin diagrams as shown in Fig. 52. Both of these are suppressed by $V_{tb}V_{ts}^*$ giving a Standard Model branching ratio

$$\mathrm{BR}^{(\mathrm{SM})}_{B_{s,d}\to\mu\mu} \approx 10^{-9}. \tag{101}$$

This gives a simple leptonic final state with minor theoretical uncertainties but a huge background so the mass resolution is paramount, the expected mass resolution for the LHC experiments is given in Table 6.

Exp.	ATLAS	CMS	LHCb
σ_m (MeV)	77	36	18

Table 6: Expected mass resolution for $B_s \to \mu^+\mu^-$.

In the MSSM, however, the amplitude involves three powers of $\tan^2\beta$, so that

$$\mathrm{BR}^{(\mathrm{MSSM})}_{B_s\to\mu\mu} \propto \tan^6\beta, \tag{102}$$

which leads to an enhancement over the SM value by up to three orders of magnitude.

9.1.5 Extra Dimensions

Many theorists believe there are more than 4 dimensions, for example string theories can only exist in 10/11 dimensions. The hierarchy problem can be solved (redefined?) in these models in one of two ways.

1. There is a large extra dimension with size $\sim$ 1mm. In this case

$$M^2_{\mathrm{Planck}} \sim M^{n+2}R^n, \tag{103}$$

where M_{Planck} is the observed Planck mass, M is the extra-dimensional Planck mass and R the radius of the additional n dimensions. In this case the Planck mass is of order 1 TeV so there is no hierarchy problem. However the hierarchy in the sizes of the dimensions must be explained.

2. Small extra dimensions in which case the extra dimension is warped. The model has two branes, we live on one and the other is at the Plank scale. The Higgs VEV is suppressed by a warp factor, $\exp(-kr_c\pi)$, where r_c is the compactification radius of the extra dimension, and k a scale of the order of the Planck scale.

We can consider what happens in extra-dimensional models by studying a scalar field in 5-dimensions. In this case the equation of motion for the scalar field is

$$\left(\frac{\partial^2}{\partial t^2} - \nabla_5^2 + m^2\right)\Phi(x, y, z, x_5, t) = 0, \tag{104}$$

where

$$\nabla_5^2 = \frac{\partial^2}{\partial x^2} + \frac{\partial^2}{\partial y^2} + \frac{\partial^2}{\partial z^2} + \frac{\partial^2}{\partial x_5^2} \tag{105}$$

is the 5-dimensional Laplace operator. If the 5-th dimension is circular we can Fourier decompose the field,

$$\Phi(x, y, z, x_5, t) = \sum_n \Phi_n(x, y, z, t)\exp(inx_5/R). \tag{106}$$

The equation of motion therefore becomes,

$$\sum_n \left(\frac{\partial^2}{\partial t^2} - \nabla_4^2 + m^2 + \frac{n^2}{R^2}\right)\Phi_n(x, y, z, t). \tag{107}$$

This gives a Kaluza-Klein (KK) tower of states with mass splitting $\sim 1/R$. There are a number of different models.

Large Extra Dimensions Only gravity propagates in the bulk, *i.e.* in the extra dimensions. We therefore only get Kaluza-Klein excitations of the graviton. In large extra dimensional models the mass splitting between the KK excitations is small and all the gravitons contribute to a given process. Phenomenologically there are deviations from the SM prediction for SM processes.

Small Extra Dimensions Again only gravity propagates in the bulk so there are only KK excitations of the graviton. In this case the mass splitting is large leading to resonant graviton production.

Universal Extra Dimensions Another alternative is to let all the Standard Model fields propagate in the bulk, *Universal Extra Dimensions* (UED). All the particles have Kaluza-Klein excitations. It is possible to have a Kaluza-Klein parity, like R-parity in SUSY. The most studied model has one extra dimension and a similar particle content to SUSY, apart from the spins. There are also some 6-dimensional models.

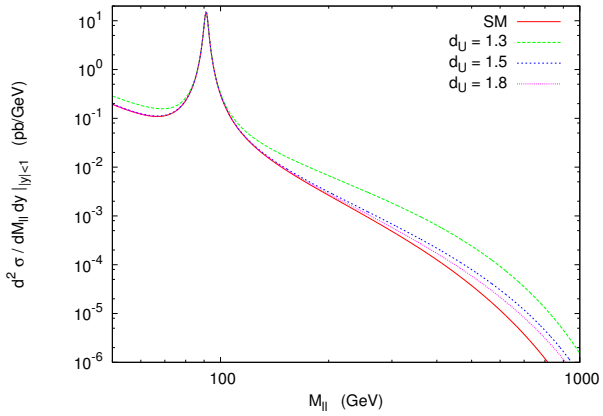

Figure 53: Drell-Yan mass spectrum including unparticle exchange taken from Ref. [24].

9.1.6 Little Higgs Models

In little Higgs models the Higgs fields are Goldstone bosons associated with breaking a global symmetry at a high scale, Λ_S. The Higgs fields acquire a mass and become pseudo-Goldstone bosons via symmetry breaking at the electroweak scale. The Higgs fields remain light as they are protected by the approximate global symmetry. The model has heavy partners for the photon, Z^0, $W^{\pm}$ bosons and the top quark as well as extra Higgs bosons. The non-linear σ-model used for the high energy theory is similar to the low energy effective theory of pions which can be used to describe QCD, or in Technicolor models. This similarity with Technicolor models is one of the reasons for the resurgence of Technicolor models in recent years.

The original Little Higgs models had problems with electroweak constraints. The solution is to introduce a discrete symmetry called T-parity, analogous to R-parity in SUSY models. This solves the problems with the precision electroweak data and provides a possible dark matter candidate. This model has a much large particle content than the original Little Higgs model and is more SUSY-like with a partner for each Standard Model particle.

9.1.7 Unparticles

In these models a new sector at a high energy scale with a non-trivial infrared (IR) fixed point is introduced. This sector interacts with the Standard Model via the exchange of particles with a large mass scale leading to an effective theory

$$\frac{C_U \Lambda_U^{d_{B_Z} - d_U}}{M_U^k} O_{\mathrm{SM}} O_U, \tag{108}$$

where: d_U is the scaling dimension of the unparticle operator O_U; M_U is the mass scale for the exchanged particles; O_{SM} is the Standard Model operator; d_{B_Z} is the dimension of the operator in the high energy theory; k gives the correct overall dimension of the interaction term. This leads to new operators which give deviations from the Standard Model predictions for various observables.

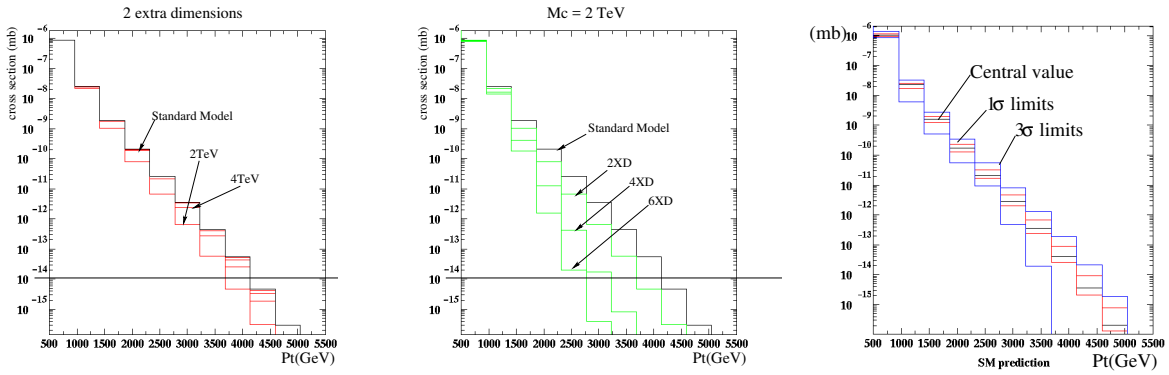

Figure 54: Jet $p_\perp$ spectrum for various numbers of extra dimensions in the ADD model taken from Ref. [25].

9.2 Beyond the Standard Model Signatures

Before we go on and consider the signals of models of new physics in great detail it is worthwhile considering what we expect to see in general. Most models of new physics predict either the existence of more particles than the Standard Model or new operators which give deviations from the Standard Model predictions. The signatures of the model depend on either how these particles are produced and decay or the type of deviations expected. In any study of BSM physics the most important thing is to understand the Standard Model backgrounds. Often the signal is at the tail of some distribution and the limits of our ability to calculate or simulate it.

9.2.1 Deviations from the Standard Model

There can be deviations from what is expected in the Standard Model due to: compositeness; exchanging towers of Kaluza-Klein gravitons in large extra dimension models; unparticle exchange; .... This tends to give changes in the shapes of spectra. Therefore in order to see a difference you need to know the shape of the Standard Model prediction.

Example I: High $p_\perp$ jets One possible signal of compositeness is the production of high $p_\perp$ jets. At one point there was a disagreement between theory and experiment at the Tevatron. However, this was not due to new physics but too little high-x gluon in the PDFs. Now as well as looking in the $p_\perp$ spectra at central rapidities where we expect to see a signal of BSM physics we also look at high rapidity as a disagreement at both central and high rapidities is more likely to be due to the parton distribution functions. An example of the jet $p_\perp$ spectrum at a range of rapidities is shown in Fig. 23.

Example II: Unparticles Many models predict deviations in the Drell-Yan mass spectra, for example in an unparticle model with the exchange of virtual spin-1 unparticles, see Fig. 53. However, we need to be careful as higher order weak corrections which can also change the shape are often neglected.

Background	Expected Events
$Z \to \nu\nu$	130 ± 14
$W \to \tau\nu$	60 ± 7
$W \to \mu\nu$	36 ± 4
$W \to e\nu$	17 ± 2
$Z \to ll$	3 ± 1
QCD	15 ± 10
Non-Collision	4 ± 4
Total Predicted	265 ± 30
Data Observed	263

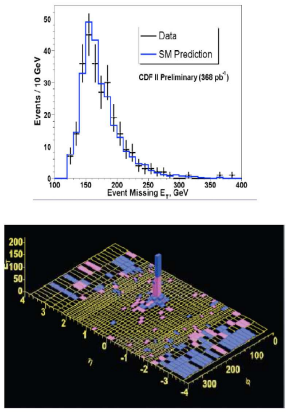

Figure 55: CDF results for monojet production taken from Fermilab wine and cheese seminar by K. Burkett.

Example III: PDF uncertainty or new physics In the ADD model of large extra dimensions there are changes in the shape of the jet $p_\perp$ and dijet mass spectra due to the exchange of KK towers of gravitons and their destructive interference with SM, as shown in Fig. 54.

9.2.2 Monojets

There are a range of models which predict monojet signals with the production of a quark or gluon which is recoiling against either: a stable neutral particle; a tower of KK gravitons in large extra dimension models; unparticles; ....

Example IV: Mono-jets at the $S\bar{p}pS$ In Ref. [26] the UA1 collaboration reported: 5 events with $E_{\perp,\text{miss}} > 40$ GeV and a narrow jet; 2 events with $E_{\perp,\text{miss}} > 40$ GeV and a neutral EM cluster. They could "not find a Standard Model explanation", and compared their findings with a calculation of SUSY pair-production [27]. They deduced a gluino mass larger than around 40 GeV. In Ref. [28], the UA2 collaboration describes similar events, also after 113 nb^{-1}, without indicating any interpretation as strongly as UA1. In Ref. [29] S. Ellis, R. Kleiss, and J. Stirling calculated the backgrounds to that process more carefully, and showed agreement with the Standard Model.

There are many different Standard Model electroweak backgrounds and a careful comparison shows they are currently in agreement with the Standard Model, see Fig. 55.

9.2.3 New Particle Production

In general there are two cases for models in which new particles are produced.

1. The model has only a few new particles, mainly produced as s-channel resonances. Examples include: Z-prime models; little Higgs models; small extra dimension models, ...

2. The model has a large number of new particles. Examples include: SUSY; UED; little Higgs models with T-parity, ...

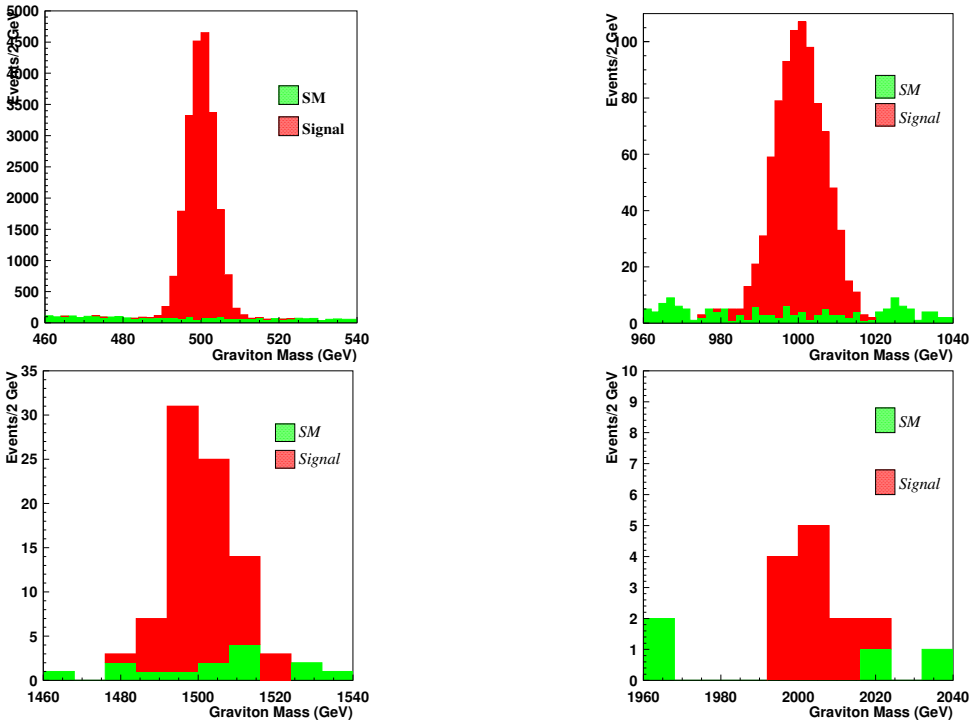

Figure 56: Example of resonant graviton production at the LHC for $\sqrt{s} = 14\,\text{GeV}$ taken from Ref. [30].

In the first type of model the main signal is the production of s-channel resonances while in the second class of models the signals are more varied and complex.

9.2.4 Resonance Production

The easiest and cleanest signal in hadron collisions is the production of an s-channel resonance which decays to e^+e^- or $\mu^+\mu^-$. Resonances in this and other channels are possible in: Little Higgs models; Z' models; UED; Small Extra Dimensions. Backgrounds can be remove using sideband subtraction.

Example V: Resonant Graviton Production The best channel, e^+e^-, gives a reach of order 2 TeV depending on the cross section for the LHC running at $\sqrt{s} = 14\,\text{GeV}$. Other channels $\mu^+\mu^-$, gg, and W^+W^- are possible. If the graviton is light enough the angular distribution of the decay products can be used to measure the spin of the resonance. An example of the dilepton mass spectrum in this model is shown in Fig. 56.

A lot of models predict hadronic resonances. This is much more problematic due to the mass resolution which smears out narrow resonances and the often huge QCD backgrounds. Although background subtraction can be used the ratio of the signal to background is often tiny, for example Fig. 57 shows the measured $Z \to b\bar{b}$ peak at the Tevatron. 57

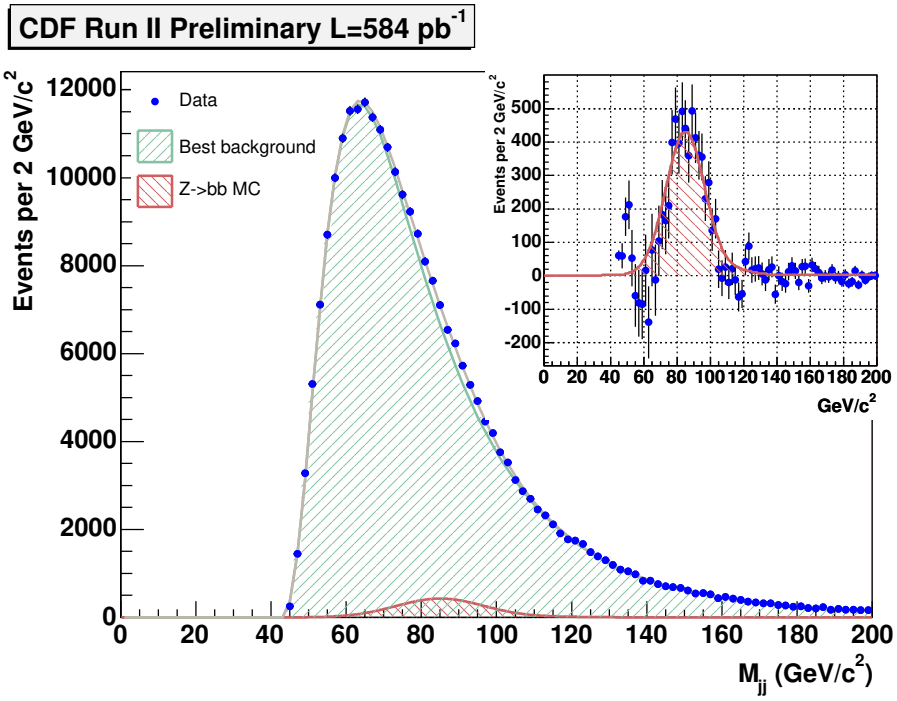

Figure 57: Dijet mass spectrum for bottom quark jets at the Tevatron taken from Ref. [31].

9.2.5 SUSY-like models

Most of the other models are "SUSY"-like, *i.e.* they contain: a partner of some kind for every Standard Model particle; often some additional particles such as extra Higgs bosons; a lightest new particle which is stable and a dark matter candidate.

A lot of new particles should be produced in these models. While some particles may be stable,[8] the the majority of these particles decay to Standard Model particles. Therefore we expect to see: charged leptons; missing transverse energy from stable neutral particles or neutrinos; jets from quarks, perhaps with bottom and charm quarks; tau leptons; Higgs boson production; photons; stable charged particles. It is worth noting that seeing an excess of these does not necessarily tell us which model has been observed.

The archetypal model containing large numbers of new particles which may be accessible at the LHC is SUSY. Other models are UED and the Little Higgs Model with T-parity. However, in practice UED is mainly used as a straw-man model for studies trying to show that a potential excess is SUSY.

Two statements which are commonly made are: the LHC will discover the Higgs boson; the LHC will discover low-energy SUSY if it exists. The first is almost certainly true, however the second is only partially true.

In hadron collisions the strongly interacting particles are dominantly produced. Therefore in SUSY squark and gluino production has the highest cross section, for example via the processes shown in Fig. 58.

[8] *i.e.* the decay length of the particle is such that the majority of the particles escape from the detector before decaying. In practice this happens for lifetimes greater than 10^{-7}s.

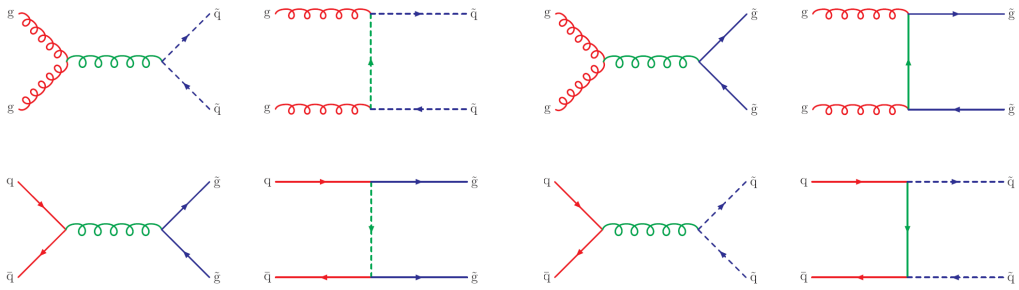

Figure 58: Example SUSY particle production processes.

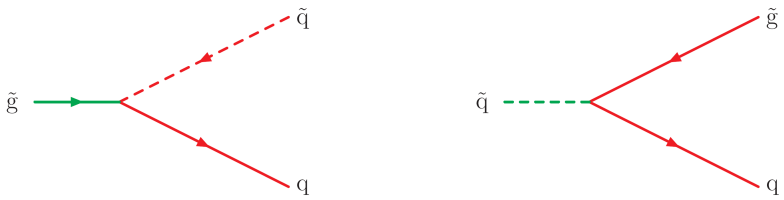

Figure 59: Example strong SUSY particle decays.

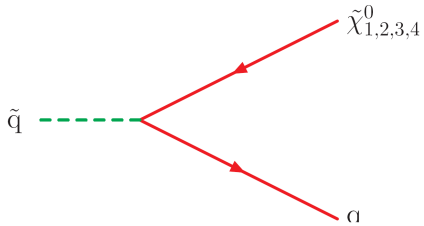

Figure 60: Example weak SUSY particle decays.

These particles then decay in a number of ways. Some of them have strong decays to other strongly interacting SUSY particles, for example via the processes shown in Fig. 59. However the lightest strongly interaction SUSY particle, squark or gluino, can only decay weakly, as shown in Fig. 60. The gluino can only have weak decays with virtual squarks or via loop diagrams. This is the main production mechanism for the weakly interacting SUSY particles.

The decays of the squarks and gluinos will produce lots of quarks and antiquarks. The weakly interacting SUSY particles will then decay giving more quarks and leptons. Eventually the lightest SUSY particle which is stable will be produced. This behaves like a neutrino and gives missing transverse energy. So the signal for SUSY is large numbers of jets and leptons with missing transverse energy. This could however be the signal for many models containing new heavy particles.

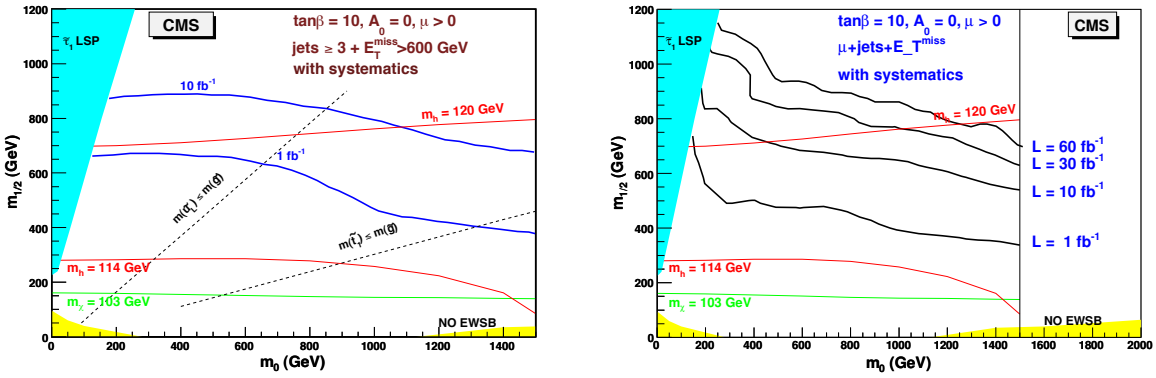

Figure 61: Expected limits in SUSY parameter space for searches using jets and missing transverse energy and jets, leptons and missing transverse energy for the LHC running at $\sqrt{s} = 14\,\text{TeV}$ taken from Ref. [32].

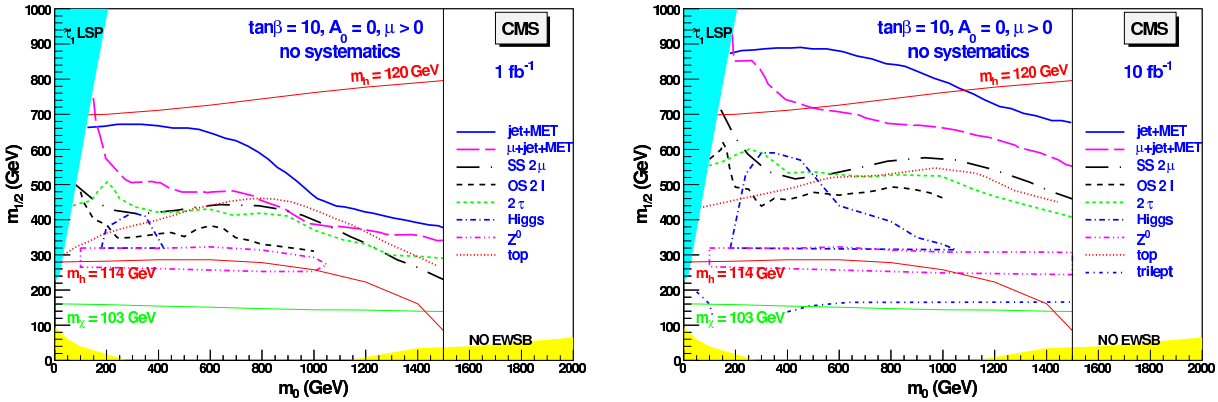

Figure 62: Expected limits in SUSY parameter space for searches using jets, leptons and missing transverse energy for the LHC running at $\sqrt{s} = 14\,\text{TeV}$ taken from Ref. [32].

All SUSY studies fall into two categories: search studies which are designed to show SUSY can be discovered by looking for a inclusive signatures and counting events; measurement studies which are designed to show that some parameters of the model, usually masses, can be measured.

There is a large reach looking for a number of high transverse momentum jets and leptons, and missing transverse energy, see Figs. 61 and 62. It is also possible to have the production of the Z^0 and Higgs bosons and top quarks. In many cases the tau lepton may be produced more often than electrons or muons.

Once we observe a signal of SUSY there are various approaches to determine the properties of the model. The simplest of these is the effective mass

$$M_{\text{eff}} = \sum_{i=1}^{n} p_{\perp i}^{\text{jet}} + \not{E}_T, \tag{109}$$

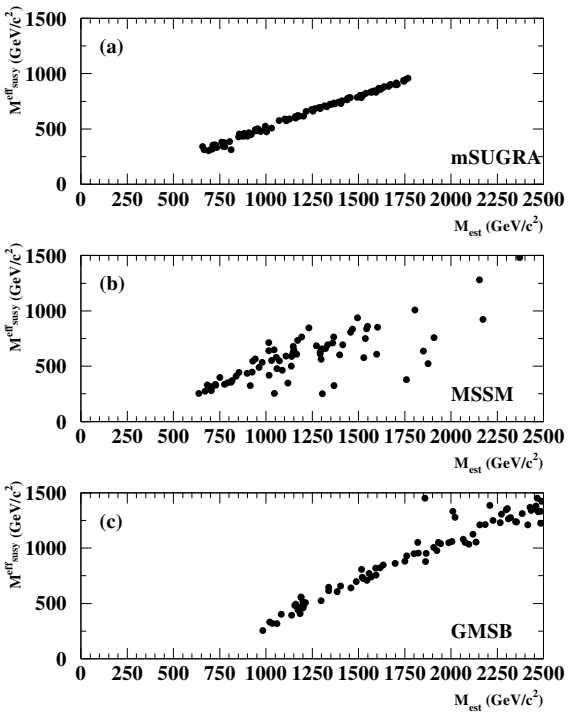

Figure 63: Correlation of the M_{eff} variable with the SUSY mass scale in various SUSY models taken from Ref. [33].

which is strongly correlated with the mass of strongly interacting SUSY particles and can be used to measure the squark/gluino mass to about 15%, see Fig. 63.

The analyzes we have just looked at are those that are used to claim the LHC will discover SUSY but this is not really what they tell us. They don't really discover SUSY. What they see is the production of massive strongly interacting particles, this does not have to be SUSY, it could easily be something else. In order to claim that a signal is SUSY we would need to know more about it. SUSY analyzes tend to proceed by looking for characteristic decay chains and using these to measure the masses of the SUSY particles and determine more properties of the model.

Given most of the searches are essentially counting experiments it is important to understand the Standard Model backgrounds which can be challenging, see Fig. 64.

9.2.6 Model Independent Searches

A popular approach in recent years has been to use experimental data to place constraints on general signatures of new physics parametrised by additional operators suppressed by a scale Λ,

$$\mathcal{L}_{\text{eff}} = \mathcal{L}_{\text{SM}} + \sum_i \frac{1}{\Lambda^{d_i-4}} c_i \mathcal{O}_i. \tag{110}$$

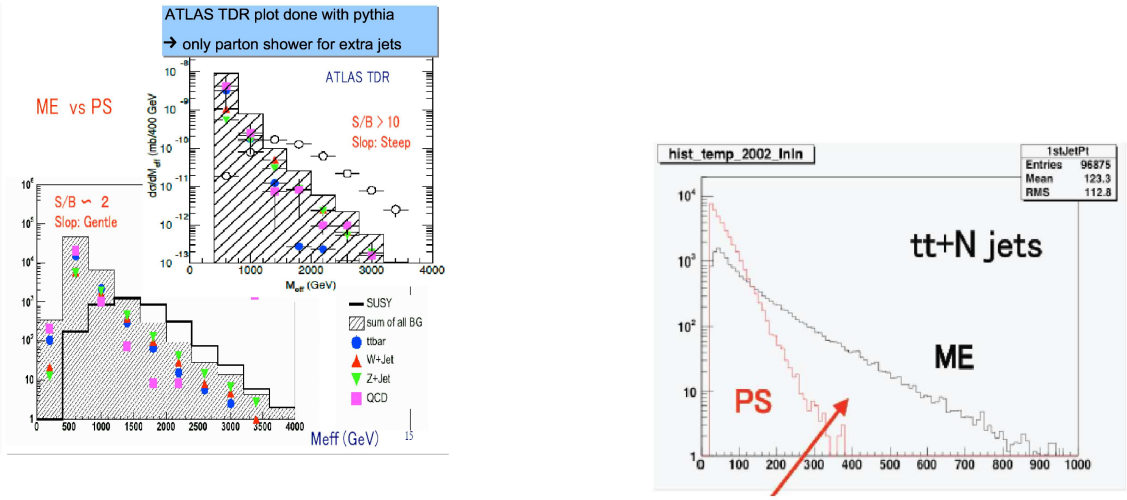

Figure 64: Backgrounds in inclusive SUSY searches.

where $\mathcal{O}_i$ are a set of dimension d_i operators with Wilson coefficients c_i. The Wilson coeffcients $c_i = c_i(\mu_R)$ run as functions of the renormalisation group scale μ_R.

Effective field theories: Even if we restrict ourselves to dimension-6 operators in our expansion the total number of Wilson coefficients is extremely large. Since we are only interested in operators that contribute to on-shell observables we can reduce to a set of independent operators by systematically using the equations of motion for each field and integration-by-parts identities. Nevertheless the number of independent dimension-6 operators for $SU(3) \times SU(2)_L \times U(1)_Y$ with 3 fermion generations is 3045 [34]. Constraining the Wilson coefficients will be a major challenge even with the large amount of new data coming from the LHC. In addition the expansion in the scale Λ must be carefully compared to the energy scales present in the observable. The EFT expansion will only be valid if $\Lambda \gg Q^2$ so that it may not be applicable to events with large transverse energy - which would hope to be of greatest senstivity to new phenomena.

Simplified Models: While not completely model independent, identifying a limited set of additional operators and interactions that can parameterise potential new physics in particular observables is a useful technique. This intermediate point between a complete EFT and a specfic model reduces the number of free parameters to a manageable level and at the same time retaining sensitivity to large classes of theories. Some further details and additional references can be found in [35].

A Kinematics and Cross Sections

A.1 Kinematics

The basic language of all phenomenology is that of relativistic kinematics, in particular four-vectors. In hadron collisions because we do not know what fraction of the beam

momenta is transferred to the partonic system it is preferable to use quantities, such as the transverse momentum, $p_\perp$, with respect to the beam direction which are invariant under longitudinal boosts along the beam direction to describe the kinematics. In addition to the transverse momentum we use the rapidity, y, and massless pseudorapidity, η,

$$y = \frac{1}{2}\ln\frac{E+p_z}{E-p_z} \overset{\text{massless}}{\longrightarrow} \eta = -\ln\tan\frac{\theta}{2}, \tag{111}$$

because rapidity differences are invariant under longitudinal boosts. Particles with small rapidities are produced at an angle close to 90^0 degrees to the beam direction while particles with large positive (negative) rapidities are travelling in the forward (backward) beam direction. The pseudorapidity is more often used experimentally as it is related to the measured scattering angle.

The four-momentum can by written as

$$p^\mu = (E,\, p_x,\, p_y,\, p_z) = (m_\perp \cosh y, p_\perp\cos\phi, p_\perp\sin\phi, m_\perp\sinh y), \tag{112}$$

where $m_\perp^2 = p_\perp^2 + m^2$. The one-particle phase-space element can also be rewritten in terms of y and $p_\perp$ as

$$\frac{\mathrm{d}^4p}{(2\pi)^4}\delta(p^2-m^2)\theta(E) = \frac{\mathrm{d}^3p}{(2\pi)^2 2E} = \frac{\mathrm{d}y\mathrm{d}^2p_\perp}{2(2\pi)^3}. \tag{113}$$

A.2 Cross Sections

The starting point of all collider physics calculations is the calculation of the scattering cross section. The cross section for a $2\to n$ scattering processes, $a+b\to 1...n$, is

$$\mathrm{d}\sigma = \frac{(2\pi)^4}{4\sqrt{(p_a\cdot p_b)^2 - m_a^2m_b^2}}\mathrm{d}\Phi_n(p_a+p_b;p_1\ldots p_n)|\overline{\mathcal{M}}|^2, \tag{114}$$

where $p_{a,b}$ and $p_{i=1,\ldots,n}$ are the momenta of the incoming and outgoing particles, respectively. The matrix element squared $|\overline{\mathcal{M}}|^2$ is summed/averaged over the spins and colours of the outgoing/incoming particles. The n-particle phase-space element is

$$\mathrm{d}\Phi_n(p_a+p_b;p_1\ldots p_n) = \delta^4\left(p_a+p_b-\sum_{i=1}^n p_i\right)\prod_{i=1}^n\frac{\mathrm{d}^3p_i}{(2\pi)^3 2E_i}, \tag{115}$$

where E_i is the energy of the ith particle. It is conventional to define $s=(p_a+p_b)^2$. For massless incoming particles $4\sqrt{(p_a\cdot p_b)^2 - m_a^2m_b^2} = 2s$.

Although modern theoretical calculations involve ever higher multiplicity final states in these lectures we will primarily deal with $2\to 2$ scattering processes in which case

$$\begin{aligned}
\mathrm{d}\Phi_2(p_a+p_b;p_1,p_2) &= \delta^4(p_a+p_b-p_1-p_2)\frac{\mathrm{d}^3p_1}{(2\pi)^3 2E_1}\frac{\mathrm{d}^3p_2}{(2\pi)^3 2E_2}, \\
&= \delta(E_a+E_b-E_1-E_2)\frac{1}{(2\pi)^6 4E_1E_2}|p_1|^2\mathrm{d}|p_1|\mathrm{d}\cos\theta\mathrm{d}\phi, \\
&= \frac{1}{8\pi(2\pi)^4}\frac{|p_1|}{\sqrt{s}}\mathrm{d}\cos\theta,
\end{aligned} \tag{116}$$

where $|p_1|$ is the magnitude of the three-momenta of either of the outgoing particles and θ and ϕ are the polar and azimuthal scattering angles, respectively. The cross section

$$\mathrm{d}\sigma = \frac{1}{16\pi s}\frac{|p_1|}{\sqrt{s}}\mathrm{d}\cos\theta|\overline{\mathcal{M}}|^2. \tag{117}$$

In is conventional to describe the scattering process in terms of the Mandelstam variables

$$s = (p_a + p_b)^2, \qquad t = (p_a - p_1)^2, \qquad u = (p_a - p_2)^2. \tag{118}$$

There are only two independent Mandelstam variables

$$s + t + u = m_1^2 + m_2^2 + m_a^2 + m_b^2 \overset{\text{massless}}{\longrightarrow} 0. \tag{119}$$

In terms of these variables

$$\mathrm{d}\sigma = \frac{1}{16\pi s^2}\mathrm{d}t|\overline{\mathcal{M}}|^2. \tag{120}$$

A.3 Cross Sections in Hadron Collisions

In hadron collisions there is an additional complication as the partons inside the hadrons interact. The hadron–hadron cross section is

$$\mathrm{d}\sigma_{AB} = \sum_{ab}\int_0^1 \mathrm{d}x_1\mathrm{d}x_2 f_{a/A}(x_1,\mu_F^2)f_{b/B}(x_2,\mu_F^2)\hat{\sigma}_{ab}(\hat{s},\mu_F^2,\mu_R^2), \tag{121}$$

where $x_{1,2}$ are momentum fractions of the interacting partons with respect to the incoming hadrons, $\hat{s} = x_1x_2s$, $\hat{\sigma}_{ab}(\hat{s},\mu_F^2,\mu_R^2)$ is the parton-level cross section for the partons a and b to produce the relevant final state, $f_{a/A}(x,\mu_F^2)$ is the parton distribution function (PDF) giving the probability of finding the parton a in the hadron A, and similarly for $f_{b/B}(x,\mu_F^2)$. The factorization and renormalisation scales are μ_F and μ_R, respectively.

In hadron collisions we usually denote the variables for partonic process with $\hat{}$, *e.g.* $\hat{s}$, $\hat{t}$ and $\hat{u}$ for the Mandelstam variables.

A.3.1 Resonance production ($2 \to 1$ processes)

The simplest example of a hadronic cross section is the production of an s-channel resonance, for example the Z^0 or Higgs bosons. We assume that the incoming partons are massless so that the 4-momenta of the incoming partons are:

$$p_{a,b} = x_{1,2}(E,\,0,\,0,\,\pm E), \tag{122}$$

where E is beam energy in the hadron–hadron centre-of-mass system of collider such that $s = 4E^2$. The Breit-Wigner cross section, *e.g.* for Z production, is

$$\hat{\sigma}_{q\bar{q}\to Z^0\to\mu^+\mu^-} = \frac{1}{N_C^2}\frac{12\pi\hat{s}}{M_Z^2}\frac{\Gamma_{q\bar{q}}\Gamma_{\mu^+\mu^-}}{(\hat{s}-M_Z^2)^2 + M_Z^2\Gamma_Z^2}. \tag{123}$$

In the limit that the width is a lot less than the mass

$$\frac{1}{(\hat{s}-M_Z^2)^2 + M_Z^2\Gamma_Z^2} \approx \frac{\pi}{M_Z\Gamma_Z}\delta(\hat{s}-M_Z^2), \tag{124}$$

the *narrow width limit*. In this case the partonic centre-of-mass system is constrained to have $\hat{s} = M_Z^2$. The rapidity $\hat{y}$ of the partonic system and $\hat{s}$ are related to the momentum fractions $x_{1,2}$ by

$$\hat{s} = x_1 x_2, s \qquad \text{and} \qquad \hat{y} = \frac{1}{2}\ln\frac{x_1 + x_2 + x_1 - x_2}{x_1 + x_2 - x_1 + x_2} = \frac{1}{2}\ln\frac{x_1}{x_2}. \tag{125}$$

Inverting these relationships we obtain

$$x_{1,2} = \sqrt{\frac{\hat{s}}{s}}\, e^{\pm\hat{y}} \qquad \text{and} \qquad \hat{y} = \frac{1}{2}\ln\frac{x_1^2 s}{\hat{s}} \leq \ln\frac{2E}{\sqrt{\hat{s}}} = \hat{y}_{\max}. \tag{126}$$

This allows us to change the variables in the integration using

$$s\mathrm{d}x_1\mathrm{d}x_2 = \mathrm{d}\hat{s}\mathrm{d}\hat{y}, \tag{127}$$

giving the differential cross section

$$\frac{\mathrm{d}\sigma_{AB\to Z^0\to\mu^+\mu^-}}{d\hat{y}} = \sum_{a,b=q\bar{q}} x_1 f_{q/A}(x_1,\, \mu_F^2) x_2 f_{\bar{q}/B}(x_2,\, \mu_F^2) \frac{12\pi^2}{N_C^2 M_Z^3} \Gamma_{q\bar{q}} B_{\mu^+\mu^-}. \tag{128}$$

A.3.2 $2 \to 2$ Scattering Processes

For most $2 \to 2$ scattering processes in hadron–hadron collisions it is easier to work in terms of the rapidities y_3, y_4 and transverse momentum, $p_\perp$, of the particles. We introduce average (centre-of-mass) rapidity and rapidity difference,

$$\bar{y} = (y_3 + y_4)/2 \qquad \text{and} \qquad y^* = (y_3 - y_4)/2, \tag{129}$$

which are related to the Bjorken x values by

$$x_{1,2} = \frac{p_\perp}{\sqrt{2}}\left(e^{\pm y_3} + e^{\pm y_4}\right) = \frac{p_\perp}{2\sqrt{s}}\, e^{\pm\bar{y}}\, \cosh y^*. \tag{130}$$

Therefore

$$\hat{s} = M_{12}^2 = 4p_\perp^2 \cosh y^* \qquad \text{and} \qquad \hat{t},\, \hat{u} = -\frac{\hat{s}}{2}\left(1 \mp \tanh y^*\right).$$

The partonic cross section, assuming all the particles are massless, is

$$\begin{aligned} \hat{\sigma}_{ab\to 12} &= \frac{1}{2\hat{s}} \int \frac{\mathrm{d}^3 p_1}{(2\pi)^3 2E_1} \frac{\mathrm{d}^3 p_2}{(2\pi)^3 2E_2} |\overline{\mathcal{M}}_{ab\to 12}|^2 (2\pi)^4 \delta^4(p_a + p_b - p_1 - p_2), \\ &= \frac{1}{2\hat{s}^2} \int \frac{\mathrm{d}^2 p_\perp}{(2\pi)^2} |\overline{\mathcal{M}}_{ab\to 12}|^2 . \end{aligned} \tag{131}$$

Therefore once we include the PDFs, sum over a, b, and integrate over $x_{1,2}$ the hadronic cross section is

$$\sigma_{AB\to 12} = \sum_{ab} \int \frac{\mathrm{d}y_1 \mathrm{d}y_2 \mathrm{d}^2 p_\perp}{16\pi^2 s^2} \frac{f_a(x_1,\, \mu_F) f_b(x_2,\, \mu_F)}{x_1 x_2} |\overline{\mathcal{M}}_{ab\to 12}|^2 ,$$

including the factor $1/(1 + \delta_{12})$ for identical final-state particles.

B Flavour Physics

While most of the interactions in the Standard Model preserve the flavour of quarks and leptons the interaction of fermions with the W boson can change the flavour of the quarks and violate CP-conservation.

In order to understand the interactions of the quarks with the W boson we first need to consider the generation of quark masses in the Standard Model. The masses of the quarks come from the Yukawa interaction with the Higgs field

$$\mathcal{L} = -Y^d_{ij}\overline{Q^I_{Li}}\phi d^I_{Rj} - Y^u_{ij}\overline{Q^I_{Li}}\epsilon\phi^* u^I_{Rj} + \text{h.c.}, \tag{132}$$

where $Y^{u,d}$ are complex 3×3 matrices, ϕ is the Higgs field, i,j are generation indices, Q^i_L are the left-handed quark doublets and, d^I_R and u^I_R are the right down- and up-type quark singlets. When the Higgs field acquires a vacuum expectation value $\langle\phi\rangle = (0, \frac{v}{\sqrt{2}})$ we get the mass terms for the quarks.

The physical states come from diagonalizing $Y^{u,d}$ using 4 unitary 3×3 matrices, $V^{u,d}_{L,R}$

$$M^f_{\text{diag}} = V^f_L Y^f V^{f\dagger}_R \frac{v}{\sqrt{2}}. \tag{133}$$

The interaction of the $W^\pm$ and the quarks is given by

$$\mathcal{L}_W = -\frac{g}{\sqrt{2}}\left[\bar{d}^I_L\gamma^\mu W^-_\mu u^I_L + \bar{u}^I_L\gamma^\mu W^+_\mu d^I_L\right]. \tag{134}$$

The interaction with the mass eigenstates, $f^M_L = V^f_L f^I_L$, is

$$\mathcal{L}_W = -\frac{g}{\sqrt{2}}\left[\bar{d}^M_L\gamma^\mu W^-_\mu V^\dagger_{\text{CKM}} u^M_L + \bar{u}^M_L\gamma^\mu W^+_\mu V_{\text{CKM}} d^M_L\right], \tag{135}$$

where the Cabibbo-Kobayashi-Maskawa (CKM) matrix

$$V_{\text{CKM}} \equiv V^u_L C V^{d\dagger}_L = \begin{pmatrix} V_{ud} & V_{us} & V_{ub} \\ V_{cd} & V_{cs} & V_{cb} \\ V_{td} & V_{ts} & V_{tb} \end{pmatrix}, \tag{136}$$

is a 3×3 unitary matrix.

The CKM matrix can be parameterized in terms of three mixing angles, (θ_{12}, θ_{13}, θ_{23}) and one phase, δ,

$$V_{\text{CKM}} = \begin{pmatrix} c_{12}c_{13} & s_{12}c_{13} & s_{13}e^{-i\delta} \\ -s_{12}c_{23} - c_{12}s_{23}s_{13}e^{i\delta} & c_{12}c_{23} - s_{12}s_{23}s_{13}e^{i\delta} & s_{23}c_{13} \\ s_{12}s_{23} - c_{12}c_{23}s_{13}e^{i\delta} & -c_{12}s_{23} - s_{12}c_{23}s_{13}e^{i\delta} & c_{23}c_{13} \end{pmatrix}, \tag{137}$$

where $s_{ij} = \sin\theta_{ij}$ and $c_{ij} = \cos\theta_{ij}$. As experimentally $s_{13} \ll s_{23} \ll s_{12} \ll 1$ it is convenient to use the Wolfenstein parameterization: $s_{12} = \lambda$; $s_{23} = A\lambda^2$; and $s_{13}e^{i\delta} = A\lambda^3(\rho + i\eta)$.
In which

$$V_{\text{CKM}} = \begin{pmatrix} 1 - \frac{1}{2}\lambda^2 & \lambda & A\lambda^3(\rho - i\eta) \\ -\lambda & 1 - \frac{1}{2}\lambda^2 & A\lambda^2 \\ A\lambda^3(1 - \rho - i\eta) & -A\lambda^2 & 1 \end{pmatrix} + \mathcal{O}(\lambda^4). \tag{138}$$

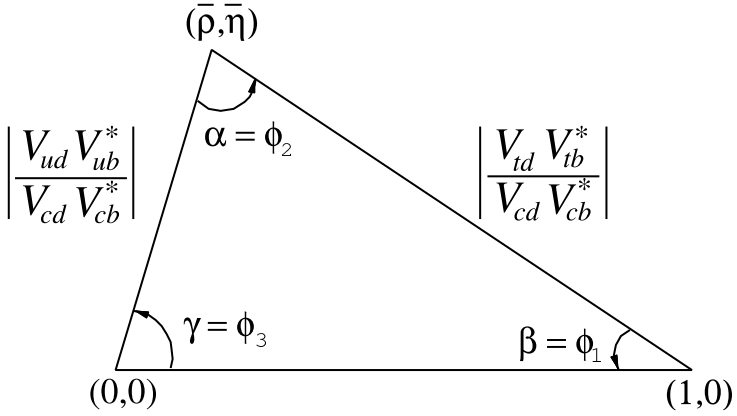

Figure 65: Unitary triangle.

If we assume that the neutrinos are massless there is no mixing for leptons. We now know that the neutrinos have small masses so there is mixing in the lepton sector. The analogy of the CKM matrix is the Maki-Nakagawa-Sakata (MNS) matrix $U_{\rm MNS}$.

A number of unitarity triangles can be constructed using the properties of the CKM matrix. The most useful one is

$$V_{ud}V_{ub}^* + V_{cd}V_{cb}^* + V_{td}V_{tb}^* = 0, \tag{139}$$

which can be represented as a triangle as shown in Fig. 65. The area of all the unitary triangles is $\frac{1}{2}J$, where J is the Jarlskog invariant, a convention-independent measure of CP-violation,

$$J = \mathrm{Im}\{V_{ud}V_{cs}V_{us}^*V_{cd}^*\}. \tag{140}$$

There are a large number of measurements which constrain the parameters in the unitarity triangle. They all measure different combinations of the parameters and over-constrain the location of the vertex of the unitarity triangle.

The magnitudes of the CKM elements control the lengths of the sides:

1. $|V_{ud}|$ is accurately measured in nuclear beta decay;

2. $|V_{cd}|$ can be measured using either semi-leptonic charm meson decays or using neutrino DIS cross sections;

3. $|V_{ub}|$ is measured using inclusive and exclusive semi-leptonic B meson decays to light mesons $B \to X_u\ell\bar{\nu}$ or $B \to \pi\ell\bar{\nu}$;

4. $|V_{cb}|$ is measured using inclusive and exclusive semi-leptonic B meson decays to charm mesons $B \to X_C\ell\bar{\nu}$ or $B \to D\ell\bar{\nu}$.

The CKM matrix elements which give the length of the remaining side can only be measured in loop-mediated processes. The most important of these, FCNCs, have already been discussed in the context of BSM physics in Section 9.1.4. These also gives rise to $B - \bar{B}$ mixing and oscillations, via the Feynman diagrams shown in Fig. 66.

Figure 66: Feynman diagrams giving $B^0 - \bar{B}^0$ and $B_s^0 - \bar{B}_s^0$ oscillations.

The oscillation probability is

$$P_{\text{oscillation}} = \frac{e^{-\Gamma t}}{2}\left[\cosh\left(\frac{\Delta\Gamma t}{2}\right) + \cos\left(\Delta m t\right)\right], \tag{141}$$

where Γ is the average width of the mesons, $\Delta\Gamma$ is the width difference between the mesons and Δm is the mass difference of the mesons. For both B_d and B_s mesons the Δm term dominates. From the box diagram

$$\Delta m_q = -\frac{G_F^2 m_W^2 \eta_B m_{B_q} B_{B_q} f_{B_q}^2}{6\pi^2} S_0\left(\frac{m_t^2}{m_W^2}\right)(V_{tq}^* V_{tb})^2. \tag{142}$$

The decay constant f_{B_q} can be measured from leptonic decays $B_q \to \ell^+\nu_\ell$ but B_{B_q} comes from lattice QCD results. The QCD correction $\eta_B \sim \mathcal{O}(1)$.

The B-factories have studied $B^0 - \bar{B}^0$ mixing in great detail giving

$$\Delta m_d = 0.507 \pm 0.005\text{ps}^{-1}. \tag{143}$$

It is important to measure both $B_d - \bar{B}_d$ and $B_s - \bar{B}_s$ mixing as some hadronic uncertainties cancel in the ratio. The rate is $\propto |V_{ts}V_{tb}^*|^2$ due to the GIM mechanism. However, the high oscillation frequency makes $B_s - \bar{B}_s$ mixing tricky to observe. The Tevatron observation relied on tagging the flavour of the B meson at production by observing an associated kaon from the fragmentation. The final result is

$$\begin{aligned} \Delta m_s &= 17.77 && \pm 0.10(\text{stat}) && \pm 0.07(\text{sys}), \\ |V_{td}||V_{ts}| &= 0.2060 && \pm 0.0007(\text{exp}) && \pm 0.008(\text{theo}). \end{aligned} \tag{144}$$

The only source of CP-violation in the Standard Model is the complex phase in the CKM matrix. In order to see any effect we need at least two diagrams for the process with different CP-phases. There are three possibilities: CP-violation in the decay (*direct*); CP-violating in the mixing (*indirect*); CP-violation in the interference between decay and mixing. Example amplitudes are shown in Fig. 67.

The simplest type of CP-violation is direct CP-violation. This is the only possible type of CP-violation for charged mesons and is usually observed by measuring an asymmetry

$$A_{f^\pm} \equiv \frac{\Gamma(M^- \to f^-) - \Gamma(M^+ \to f^+)}{\Gamma(M^- \to f^-) + \Gamma(M^+ \to f^+)} \overset{\text{CP conserved}}{\longrightarrow} 0. \tag{145}$$

If CP-symmetry holds, then $|K_L\rangle = \frac{1}{\sqrt{2}}(|K^0\rangle + |\bar{K}^0\rangle)$ would be a CP-eigenstate with $|K_L\rangle = |\bar{K}_L\rangle$. If we take $|M\rangle = |K_L\rangle$ and $|f\rangle = |\pi^- e^+ \nu_e\rangle$ the corresponding CP-asymmetry is $A_{\text{CP}} = (0.327 \pm 0.012)\%$, which means that K_L is not a CP-eigenstate

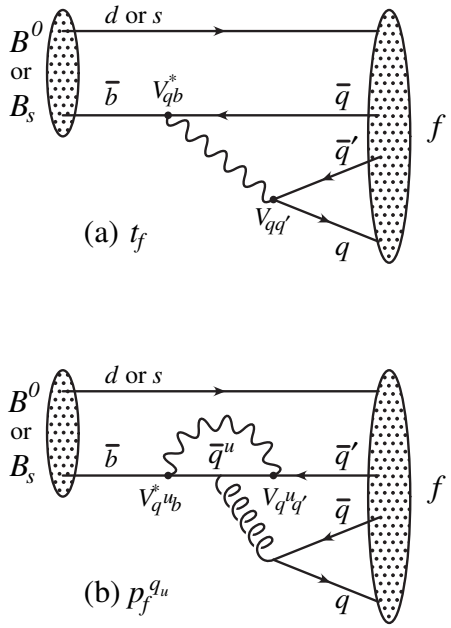

Figure 67: Examples of tree and penguin mediated processes, taken from Ref. [8].

and there is CP-violation. There are many possible modes which measure different cominations of the angles in the unitarity triangle. The observed flavour and CP-violation is consistent with the Standard Model, i.e. the description by the CKM matrix, see Fig. 68.

There is one final area of flavour physics which is important. The matter in the universe consists of particles and not antiparticles. There are three Sakharov conditions required for this to happen:

1. baryon number violation;
2. C-symmetry and CP-symmetry violation;
3. interactions out of thermal equilibrium.

There are non-perturbative effects in the SM which violate baryon number. However, the amount of CP-violation in the quark sector is not enough to give the observed matter-antimatter asymmetry, there might be more in the lepton sector, otherwise we need a new physics source of CP-violation.

C Color algebra

The color factors C_F and C_A correspond to the factors one gets for emitting a gluon off a quark or gluon line respectively.

The color factor for the splitting of a gluon into a quark-antiquark pair is given by T_R.

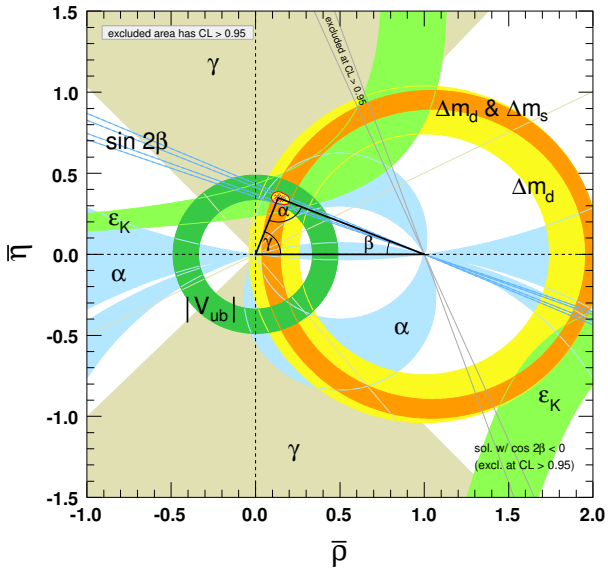

Figure 68: Experimental measurement of the unitarity triangle taken from Ref. [8].

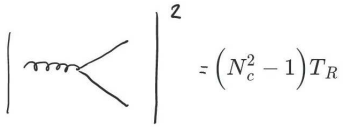

One can compute color factors using a set of pictorial rules (see [36] for more details.) All these rules follow from the properties of the SU(3) color group.

$$T^a_{ij} T^a_{jk} = \frac{1}{2}\left(\delta_{il}\delta_{jk} - \frac{1}{N_c}\delta_{ij}\delta_{kl}\right)$$

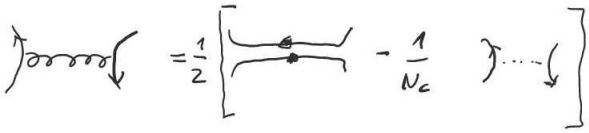

The three-gluon vertex can be rewritten as:

$$if^{abc} = 2\left(\mathrm{Tr}\left[T^a T^b T^c\right] - \mathrm{Tr}\left[T^a T^c T^b\right]\right)$$

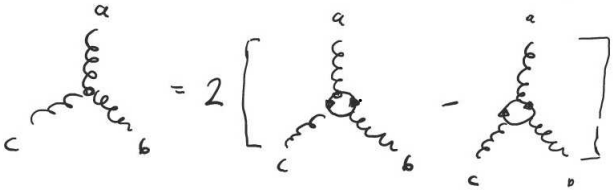

Here is an example of a calculation of a color factor with the pictorial method.

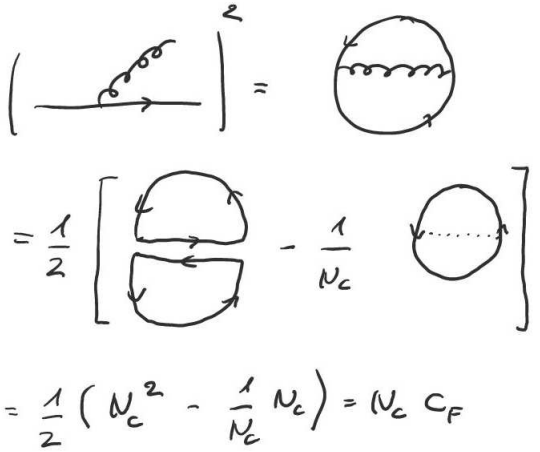

We have used the fact that a closed fermion loop with no gluon attachments amounts to a factor of N_c, while a closed gluon loop would give a factor of $N_c^2 - 1$.

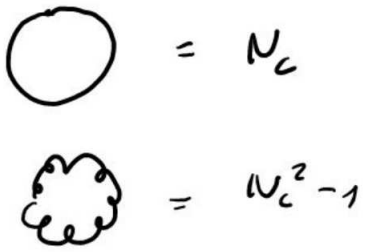

A gluon loop on a gluon line can be written as the same line without the loop but with a factor of N_c.

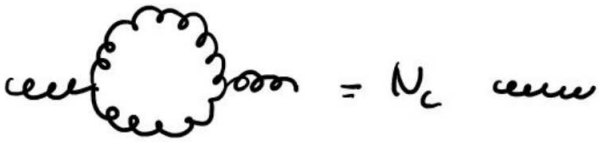

References

[1] F. Halzen and A. D. Martin, *Quarks and Leptons: An Introductory Course in Modern Particle Physics*, . ISBN-9780471887416.

[2] V. D. Barger and R. J. N. Phillips, *Collider Physics*, . Redwood City, USA: Addison-Wesley (1987) 592 P. (Frontiers in Physics, 71).

[3] R. K. Ellis, W. J. Stirling, and B. R. Webber, *QCD and Collider Physics*, *Camb. Monogr. Part. Phys. Nucl. Phys. Cosmol.* **8** (1996) 1–435.

[4] G. Dissertori, I. G. Knowles, and M. Schmelling, *Quantum Chromodynamics: High energy experiments and theory*, . Oxford, UK: Clarendon (2003) 538 p.

[5] J. F. Gunion, H. E. Haber, G. L. Kane, and S. Dawson, *The Higgs Hunter's Guide*, *Front. Phys.* **80** (2000) 1–448.

[6] G. P. Salam, *Towards Jetography*, *Eur. Phys. J.* **C67** (2010) 637–686, [arXiv:0906.1833].

[7] A. Buckley *et. al.*, *General-purpose event generators for LHC physics*, arXiv:1101.2599.

[8] **Particle Data Group** Collaboration, K. Nakamura *et. al.*, *Review of particle physics*, *J. Phys.* **G37** (2010) 075021.

[9] **OPAL** Collaboration, G. Abbiendi *et. al.*, *Measurement of event shape distributions and moments in e^+e^- →hadrons at 91-209 GeV and a determination of α_S*, *Eur. Phys. J.* **C40** (2005) 287–316, [hep-ex/0503051].

[10] **H1 and ZEUS** Collaboration, F. D. Aaron *et. al.*, *Combined Measurement and QCD Analysis of the Inclusive ep Scattering Cross Sections at HERA*, *JHEP* **01** (2010) 109, [arXiv:0911.0884].

[11] J. M. Campbell, J. W. Huston, and W. J. Stirling, *Hard Interactions of Quarks and Gluons: A Primer for LHC Physics*, *Rept. Prog. Phys.* **70** (2007) 89, [hep-ph/0611148].

[12] **CDF** Collaboration, T. A. Aaltonen *et. al.*, *Measurement of $d\sigma/dy$ of Drell-Yan e^+e^- pairs in the Z Mass Region from $p\bar{p}$ Collisions at $\sqrt{s} = 1.96$ TeV*, *Phys. Lett.* **B692** (2010) 232–239, [arXiv:0908.3914].

[13] **D0** Collaboration, V. M. Abazov *et. al.*, *Measurement of the shape of the boson transverse momentum distribution in $p\bar{p} \to Z/\gamma^* \to e^+e^- + X$ events produced at $\sqrt{s} = 1.96$-TeV*, *Phys. Rev. Lett.* **100** (2008) 102002, [arXiv:0712.0803].

[14] C. Anastasiou, L. J. Dixon, K. Melnikov, and F. Petriello, *High precision QCD at hadron colliders: Electroweak gauge boson rapidity distributions at NNLO*, *Phys. Rev.* **D69** (2004) 094008, [hep-ph/0312266].

[15] J. R. Ellis, M. K. Gaillard, and G. G. Ross, *Search for Gluons in e+ e- Annihilation*, *Nucl. Phys.* **B111** (1976) 253.

[16] R. K. Ellis, D. A. Ross, and A. E. Terrano, *The Perturbative Calculation of Jet Structure in e^+e^- Annihilation*, *Nucl. Phys.* **B178** (1981) 421.

[17] A. Gehrmann-De Ridder, T. Gehrmann, E. W. N. Glover, and G. Heinrich, *Second-order QCD corrections to the thrust distribution*, *Phys. Rev. Lett.* **99** (2007) 132002, [arXiv:0707.1285].

[18] **CDF** Collaboration, T. Aaltonen *et. al.*, *Measurement of the Inclusive Jet Cross Section at the Fermilab Tevatron p-pbar Collider Using a Cone-Based Jet Algorithm*, *Phys. Rev.* **D78** (2008) 052006, [arXiv:0807.2204].

[19] **CDF** Collaboration, T. Aaltonen *et. al.*, *First Run II Measurement of the W Boson Mass*, *Phys. Rev.* **D77** (2008) 112001, [arXiv:0708.3642].

[20] V. Buescher and K. Jakobs, *Higgs boson searches at hadron colliders*, *Int. J. Mod. Phys.* **A20** (2005) 2523–2602, [hep-ph/0504099].

[21] C. Anastasiou, C. Duhr, F. Dulat, F. Herzog, and B. Mistlberger, *Higgs Boson Gluon-Fusion Production in QCD at Three Loops*, *Phys. Rev. Lett.* **114** (2015) 212001, [arXiv:1503.0605].

[22] C. Anastasiou, C. Duhr, F. Dulat, E. Furlan, T. Gehrmann, F. Herzog, A. Lazopoulos, and B. Mistlberger, *High precision determination of the gluon fusion Higgs boson cross-section at the LHC*, *JHEP* **05** (2016) 058, [arXiv:1602.0069].

[23] S. Dawson, *Introduction to the physics of Higgs bosons*, in *Theoretical Advanced Study Institute in Elementary Particle Physics (TASI 94): CP Violation and the limits of the Standard Model Boulder, Colorado, May 29-June 24, 1994*, pp. 0445–506, 1994. hep-ph/9411325.

[24] K. Cheung, W.-Y. Keung, and T.-C. Yuan, *Collider Phenomenology of Unparticle Physics*, *Phys. Rev.* **D76** (2007) 055003, [arXiv:0706.3155].

[25] **ATLAS** Collaboration, S. Ferrag, *Proton structure impact on sensitivity to extra-dimensions at LHC*, hep-ph/0407303.

[26] **UA1** Collaboration, G. Arnison *et. al.*, *Experimental Observation of Events with Large Missing Transverse Energy Accompanied by a Jet Or a Photon(s) in $p\bar{p}$ Collisions at $\sqrt{s} = 540$-GeV*, *Phys. Lett.* **B139** (1984) 115.

[27] J. R. Ellis and H. Kowalski, *Supersymmetric Particles at the CERN $p\bar{p}$ Collider*, *Nucl. Phys.* **B246** (1984) 189.

[28] **Bern-CERN-Copenhagen-Orsay-Pavia-Saclay** Collaboration, P. Bagnaia *et. al.*, *Observation of Electrons Produced in Association with Hard Jets and Large Missing Transverse Momentum in $p\bar{p}$ Collisions at $\sqrt{s} = 540$ GeV*, *Phys. Lett.* **B139** (1984) 105.

[29] S. D. Ellis, R. Kleiss, and W. J. Stirling, *Missing Transverse Energy Events and the Standard Model*, *Phys. Lett.* **B158** (1985) 341.

[30] B. C. Allanach, K. Odagiri, M. A. Parker, and B. R. Webber, *Searching for narrow graviton resonances with the ATLAS detector at the Large Hadron Collider*, *JHEP* **09** (2000) 019, [hep-ph/0006114].

[31] J. Donini *et. al.*, *Energy Calibration of b-Quark Jets with $Z \to b\bar{b}$ Decays at the Tevatron Collider*, *Nucl. Instrum. Meth.* **A596** (2008) 354–367, [arXiv:0801.3906].

[32] **CMS** Collaboration, G. L. Bayatian *et. al.*, *CMS technical design report, volume II: Physics performance*, *J. Phys.* **G34** (2007) 995–1579.

[33] D. R. Tovey, *Measuring the SUSY mass scale at the LHC*, *Phys. Lett.* **B498** (2001) 1–10, [hep-ph/0006276].

[34] B. Henning, X. Lu, T. Melia, and H. Murayama, *2, 84, 30, 993, 560, 15456, 11962, 261485, ...: Higher dimension operators in the SM EFT*, arXiv:1512.0343.

[35] **LHC New Physics Working Group** Collaboration, D. Alves, *Simplified Models for LHC New Physics Searches*, *J. Phys.* **G39** (2012) 105005, [arXiv:1105.2838].

[36] L. J. Dixon, *Calculating scattering amplitudes efficiently*, hep-ph/9601359.